A Study of An Electrodeless Low Pressure Argon Plasma as A New Ion Laser Source

by

Peiyuan Zhu

October 1990

A thesis submitted for the degree of

Doctor of Philosophy

of the Australian National University

This thesis is entirely my own work,

except where explicitly indicated.

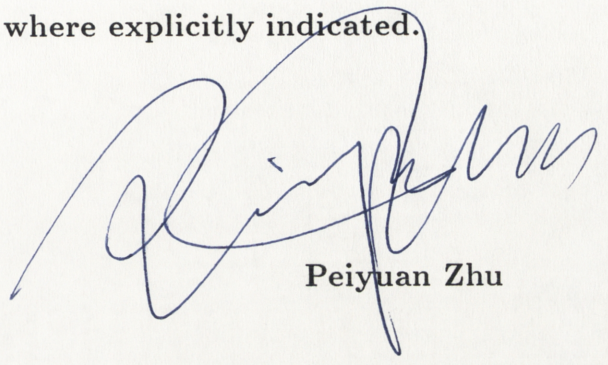

Peiyuan Zhu

Plasma Research Laboratory

Research School of Physical Sciences

The Australian National University

Canberra, A.C.T., Australia

Acknowledgements

It is my pleasure to thank my acadamic supervisors, Dr. Rod Boswell and Professor Sydney Hamberger. Their encouragement has made this study possible. I have gained much from their valuable ideas, suggestions and comments on this thesis.

Special thanks go to Dr. Robert Porteous and particularly Arnstein Prytz, not only for their excellent work in building the Basil-II apparatus, but also for their involvement in this study, through discussions and suggestions. I have learnt a lot from Arnstein Prytz's experience in tuning and running Basil-II plasma. I also wish to thank Dr. Andrew Perry, Dr. Boyd Blackwell and Dr. John Howard. I have benefited enormously from discussions with them.

Thanks also go to the technical staff of PRL for the help they offered me during my experimental work. I thank especially Alen Campbell, Peter Lloyd, Eddie Wedhorn, Steve Hyde, and John Wach.

Many people have helped me to overcome my language difficulties, among them I particularly wish to thank Irene Wyld, Helen Smith, and Helen Hawes.

My wife Hongzheng Chen deserves the most special thanks of all. Without her support, this thesis could never be finished. I also thank her for typesetting the thesis.

I acknowledge the financial support of a PhD scholarship from the Australian National University.

This thesis is dedicated to my motherland,
my parents, and my wife Hongzheng Chen

Abstract

This thesis presents the investigation of an electrodeless argon magnetoplasma discharge (Basil-II) as a new ion laser source. The plasma is generated by an m=1 helicon wave, which is excited by a double loop rf antenna.

The optical properties of the discharge have been measured to pursue the possibility of making a new ion laser based on the discharge. Both the spontaneous emission and the optical gain of the Ar^+ 488nm transition are systematically measured as functions of longitudinal magnetic field (0.05-0.15T), argon filling pressure (0.3-1.5Pa), rf power (1-5kW), radio frequency (7-14MHz) and tube diameter (30-65mm). The plasma parameters are studied to aid in the understanding of the discharge behaviour. A central electron density $\sim 10^{20}m^{-3}$ is found to be typical of this discharge, with a bulk electron temperature in the range of 3 - 5eV.

The main results of this study have led to the invention of a new Ar^+ laser, based on this discharge, which has a measured output power of 0.5W at the 488nm transition with an efficiency of 10^{-4}. The mechanism for population inversion is studied, and the Landau damping of an m=1 helicon wave is found to be responsible. During this study a beam-like electron distribution tail is observed for the first time in a laboratory plasma without electron beam injection.

Contents

Chapter 1

Introduction

This thesis presents an experimental investigation of an electrodeless argon discharge operating as a new ion laser source. Some theoretical efforts are also made to explain the population inversion mechanism of this discharge.

The initial purpose of this study is to pursue the possibility of applying a very efficient discharge, which is generated by an m=1 helicon wave excited by an external double-loop rf antenna, to the ion laser field. Once this was successfully accomplished, attention was turned to the population inversion mechanism.

The plasma under this study is operated in a very reproducible repetitive pulse mode to satisfy the requirements of the rf power supply, which can provide up to 5kW rf power in the frequency range 3-18MHz in pulsed operation mode. The pulse duration is chosen to be a few milliseconds which is much longer than the characteristic time needed to establish the plasma parameters so that the plasma reaches a quasistationary state and the results can be meaningful for dc discharges[1]. Although the transient nature of the discharge has been studied to some degree, the physics of the transient nature of this discharge is far from

clear at this stage. The main attention of this study is paid to the discharge behaviour when a quasistationary state is reached, since by then there is enough optical gain for laser action. This investigation has not only led to an invention of a new form of argon ion laser, but also explains, to some extent, the physics of this discharge.

This chapter will briefly review the background of the subject. The experimental apparatus and the plasma diagnostics relevant to this thesis will be described in Chapter 2 and Chapter 3 respectively. Then follow the main parts of this thesis, Chapters 4, 5, and 6 which present the experimental results. Chapter 4 investigates the optical properties of the plasma and Chapter 5 describes the phenomena of the new Basil laser. In Chapter 6, some plasma parameters are studied. It is found that the electron distribution can not be simply described by a Maxwellian, hence effort has been made to investigate the tail of the electron energy distribution. A theoretical discussion is made for a possible explanation of the population inversion mechanism, which will be discussed in Chapter 7. The last chapter gives the conclusions.

Section 1 of this chapter gives a short review of the Ar^+ ion laser while Section 2 describes briefly the basic characteristics of the discharge generated by an m=1 helicon wave.

1.1 Review of cw Ar^+ laser

The active medium used in a conventional Ar^+ laser is the positive column of a high current density (>100A/cm^2), small tube diameter (1-16mm) dc- excited argon discharge. The first cw Ar^+ laser was developed by Bridges[3] early in

1964, and since then the Ar^+ laser has been an active topic due to its use in research into holography, nonlinear optics, light scattering, communication, and various other scientific research fields. There are many publications on this topic: an early review paper in 1969[4] included 185 references. Although a few good review papers are available[4]-[6], the physics of the Ar^+ laser is still not fully understood and it is still attracting much attention[7]-[9].

In this section only some general features of the Ar^+ laser, which are relevant to this study will be outlined. For more details of the dc-excited Ar^+ laser, a recent publication can be referred[7].

1.1.1 Population inversion mechanism

Fig 1.1 shows part of the level scheme of Ar^+ and indicates the 10 principal Ar^+ laser transitions which are between levels of the 4s and 4p configurations. Although the formation of population inversion is still not fully understood[7], it has been commonly accepted that the much quicker decay of the lower levels (of the 4s configuration) than that of the upper levels plays an important role.

For the excitation of the 4p levels, four possible processes were proposed[4]-[6]:

1. Direct excitation by electron impact from the ground state of the argon atom.

2. Two-step excitation by electron impact via the Ar^+ ground state.

3. Multi-step excitation by electron impact via certain configuration states of either the neutral atom or the ion.

4. Radiative cascade transitions to 4p-configuration levels from higher states excited by electron impact either in one step or multi-step from the ion ground

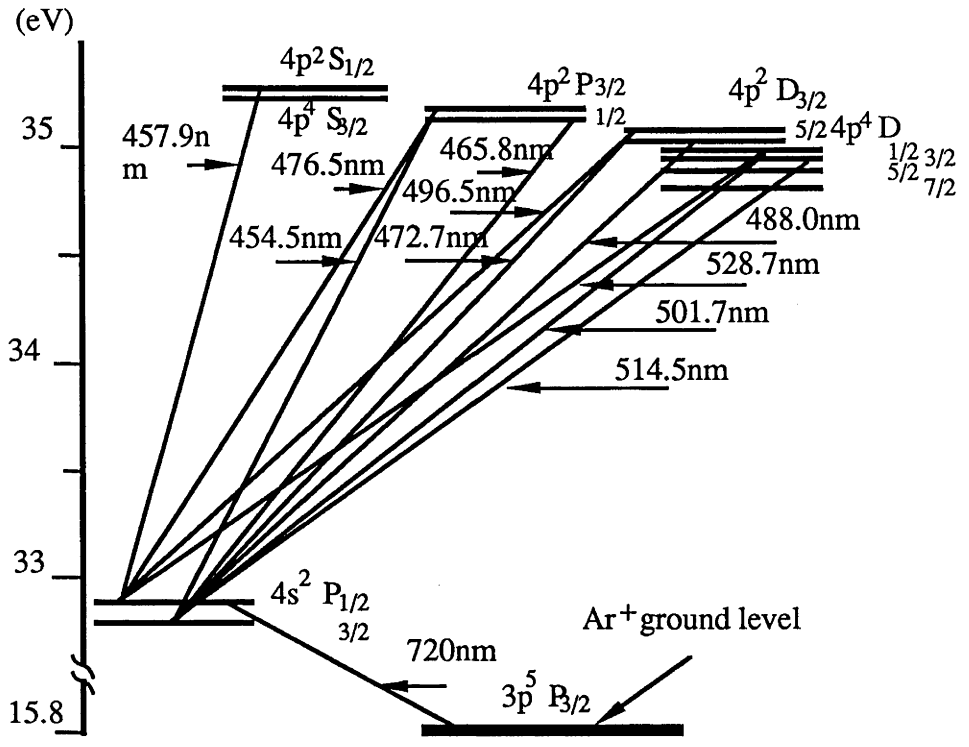

Figure 1.1: Level scheme of the 4p and 4s ion configurations. The lasing transitions between the two configurations are indicated.

state.

Fig 1.2 shows the four possible channels for the excitation of the 4p configuration levels. High electron energy is essential for all these four channels, which is the main reason why a high current density discharge is required.

1.1.2 Plasma parameters and electrical characteristics

Table 1-1. lists some electric characteristics (data from reference[10]) for Ar^+ laser discharge under conditions close to optimal for total laser output power.

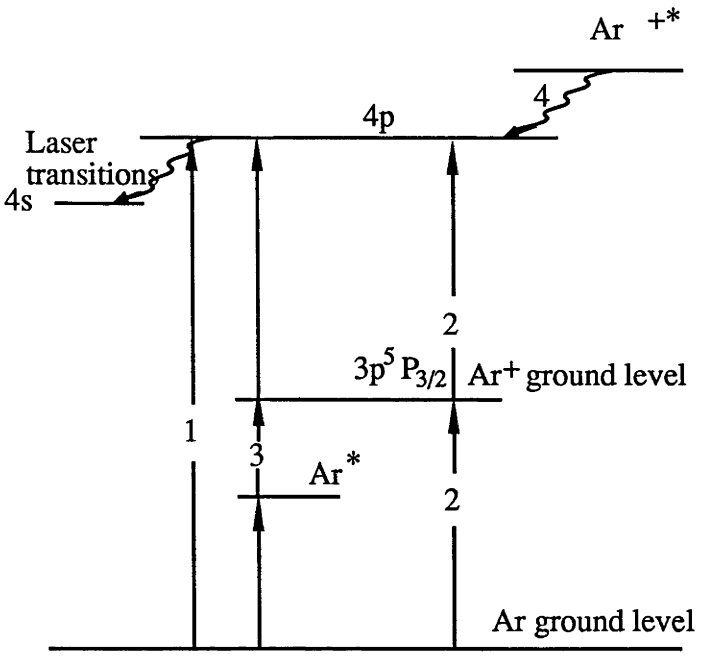

Figure 1.2: Possible channels for the excitation of the 4p-configuration levels

The table reflects, to some degree, the basic features of the dc-excited Ar^+ laser. Column 1 of the table gives the tube diameter and columns 2 and 3 list the operating current and current density respectively. The electric power per unit length of the discharge column W_{in}/l is listed in Column 4 and the laser output efficiency is listed in the last column.

ϕ (mm)	i(A)	j(A/cm^2)	W_{in}/l(kW/cm)	Efficiency
1.25	40	3500	0.84	10^{-4}
2.7	90	1600	0.7	—
11.0	330	340	0.76	1.03×10^{-3}
16.0	420	230	0.8	1.56×10^{-3}

Table 1-1. Electric characteristics and laser output of Ar^+ laser discharge in tubes of varying diameters

It can be seen from Table 1-1, although the electron current and current density vary for different tube diameters, the electric power per unit discharge column is nearly a constant of 0.8kW/cm for obtaining maximum laser output and the laser output efficiency is proportional to the tube diameter. Increasing the discharge tube size then seems a logical approach to obtain higher efficiency. However, no success has been achieved so far in making a dc-excited Ar^+ laser discharge with a tube diameter larger than 16mm.

The electron distribution of a cw Ar^+ laser has been found to be a Maxwellian and the electron temperature T_e and the electron density n_e of an Ar^+ laser are as follows[7]:

$$T_e \sim \text{2-9eV};$$

$$n_e \sim (\text{1-8})\times 10^{19}\text{m}^{-3},$$

which are similar to that of a large tube diameter (45mm) discharge generated by a helicon wave [11]. Hence it is worthwhile to study the possibility of using a large (30-65mm) tube diameter discharge generated by helicon waves to make an Ar^+ laser.

1.2 Brief description of the discharge generated by a m=1 helicon wave

Helicon waves are bounded whistler waves in the frequency range well below the electron gyrofrequency but well above the ion gyrofrequency ($\omega_{ic} \ll \omega \ll \omega_{ec}$).

It was found in 1970 that, by employing a double loop rf antenna, one could excite an m=1 helicon standing wave, which in turn coupled the rf energy into the discharge[12] to produce a dense plasma. This provides a very efficient means of making an electrodeless discharge with a highly ionized ($\sim$ 100%) core on the axis[13]. The discharge generated by this method has been used as the plasma source for wave studies[14],[15], for plasma etching of silicon[16],[17], and has some other potential applications[18],[19].

Fig1.3 shows a simplified diagram of the wave field of the m=1 helicon standing wave[12]. The standing wave is formed by two helicon waves propagating in opposite axial (z) directions. These two waves can either both be excited by the external rf field at the same time, since the field does not have a preferred direction, or be formed as a result of the wave reflection from the end. The field of a non-damped helicon wave in a cylindrical symetric system can be written in the form

$$B_s = B_{0s} e^{-i(\omega t \pm kz + m\theta)},$$

where $s = r, \theta, z$. Hence the wave components of an m=1 standing helicon wave have the form $B_{m=1} \propto \sin(kz) \exp -(i\omega t + \theta)$, where k is the helicon wave number. Notice that the wave amplitude will change its sign on the wave node and this means there will be a sudden 180° degree phase change. The feature of this sudden phase change can be used to experimentally determine the helicon wave number k [12], hence the wave phase velocity $v_{ph} = \frac{\omega}{k}$.

It has been reported[11] that a high density, high ionized plasma in a 1.6m long, 50mm diameter discharge tube with reasonable uniformity along the axial direction can be generated by the m=1 helicon wave. With an rf input power of $\sim$1 kW, one obtains a highly axially peaked plasma with a central density of

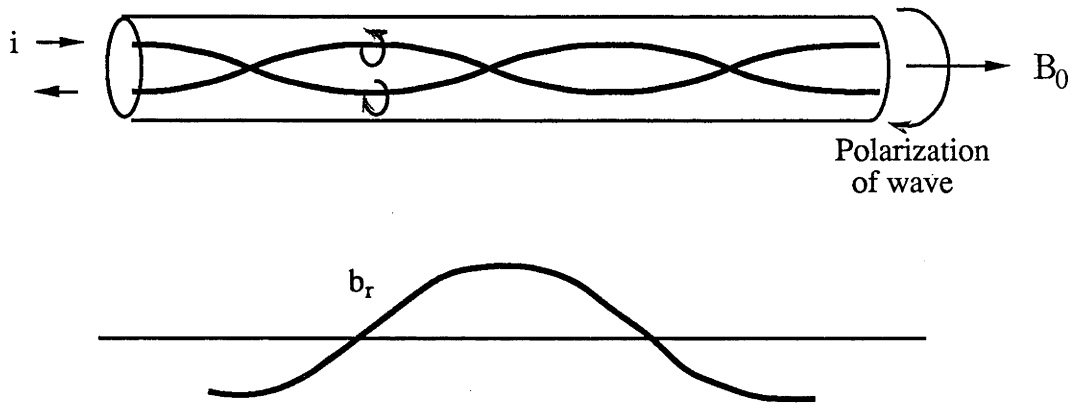

Figure 1.3: Wave field of the m=1 helicon standing wave. (From Boswell[10])

10^{18}-$10^{19}$$m^{-3}$, electron temperature of 3eV and ion temperature of 1eV. This kind of discharge has plasma parameters similar to that of an Ar^+ laser discharge, and has the proper geometry for developing a laser. Hence there are sufficient reasons for an investigation of this discharge as a new ion laser source, which is just the purpose of this thesis.

Table.1-2 lists some typical ranges of the parameters of the discharges generated by the m=1 helicon wave. For more details of the features of this discharge, see reference[12].

Antenna length (m)	0.05–0.5
Plasma length (m)	0.30–1.6
Tube diameter (mm)	30–300
Input power(kW)	0.1–5
Pressure (Pa)	0.1–1.5
RF frequency	$\omega_{ic} \ll \omega_{rf} \ll \omega_{ec}$
B_0 (T)	$<2f_{rf} \times 10^{-2}$ (f_{rf} in MHz)
T_e (eV)	3-5
n_e ($10^{19}\mathrm{m}^{-3}$)	0.01–10

Table 1-2. Typical ranges of the parameters

Chapter 2

Experimental apparatus

This chapter describes the discharge apparatus Basil-II (section 1), in which a low pressure argon discharge is created. The rf supply, the rf antenna (section 2) and the data collection system (section 3) will also be described in this chapter.

2.1 Basil-II

Basil-II is a radio frequency excitation discharge apparatus in which a highly ionized discharge with central density $\sim 10^{20}$ m^{-3} can be produced. Fig 1.1 shows a sketch of the apparatus.

Briefly, the apparatus consists of a cylindrical glass vacuum vessel inside 14 magnetic field coils arranged to produce an uniform longitudinal magnetic field. The vacuum vessel is coaxial with the coils. An external double-loop rf antenna, which serves to couple the rf power to the discharge, is located at the middle of

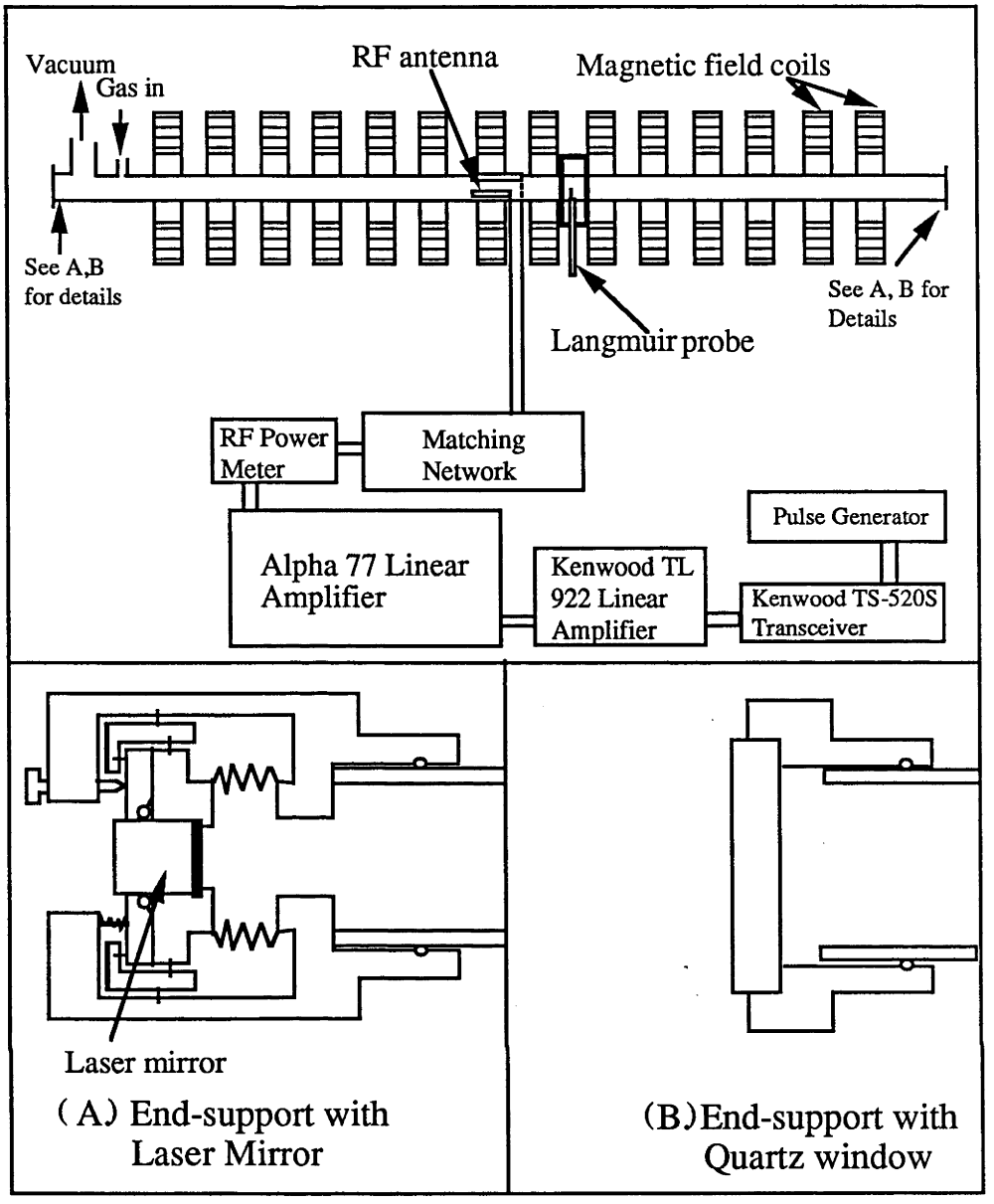

Figure 2.1: Basil-II apparatus

the vacuum vessel and attached to the outside of the plasma tube. Up to 5 kW

rf power (at 3 to 14 MHz frequency) can be fed to the antenna via a capacitive network.

2.1.1 Vacuum system

The vacuum chamber of Basil-II is a pyrex glass tube 1.7m long terminated by two stainless steel end-supports attached to the main support frame. A probe box, which will be described in detail in the next chapter, is mounted on the tube at a position 16 cm away from the middle. There is a square hole of $1cm^2$ in the glass tube at this position so the radial probe can be inserted without causing too much change in the boundary conditions.

One of the end-supports is connected to both the vacuum system and the working-gas feed. Both end-supports have a set of adapter pieces which enables us to choose the tube outer diameters among the sizes 4, 5, 7 and 10 cm. Either a quartz window or an adjustable laser mirror support can be mounted on the end-support, so as to allow both end-on spectroscopic study and laser output. Fig 2.1(a) shows a section view of the laser mirror mount on the end-support, while Fig 2.1(b) shows a section view of the quartz window on the end-support.

The pumping system consists of a 300l/s Edwards diffusion pump backed by an Edwards E2M5 rotary pump. The whole system can maintain the vacuum vessel at a background pressure $\sim 10^{-4}$ Pa. The base pressure of the vacuum vessel is measured with a penning gauge, while the gas filling pressure is monitored by either penning or pirani gauges, depending on the pressure range. These gauges are calibrated against an MKS baratron capacitance manometer every six months. The calibration curves for both gauges are shown in Fig 2.2. The argon gas is continuously passed through the system via a gas feed system during the experiments to minimize gas trapping. The gas feed system consists of a compressed gas cylinder with gas pressure controllers and an MKS mass flow

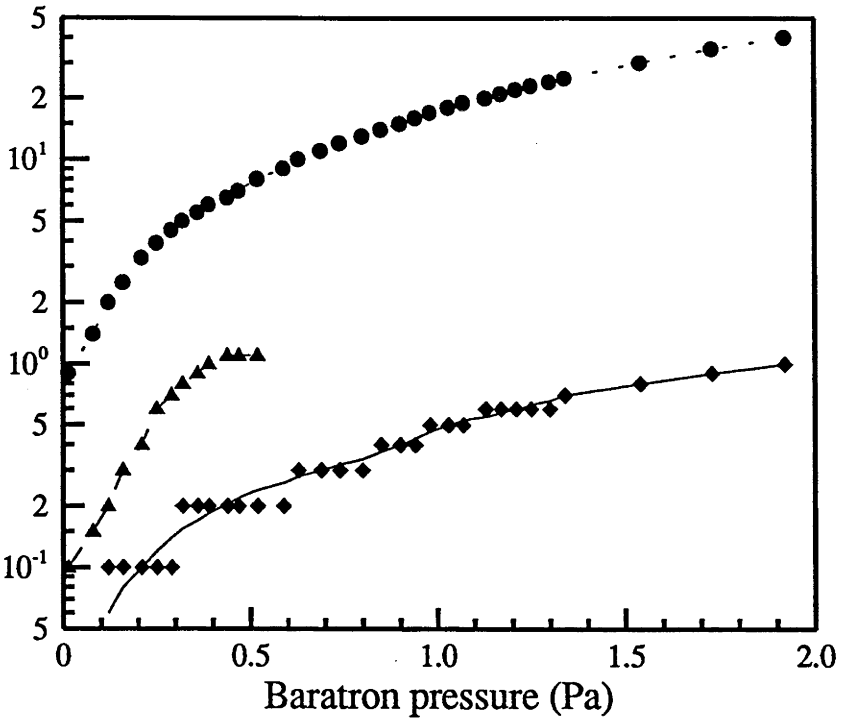

Figure 2.2: The calibration of Penning gauge (△, unit of Pa), pirani gauge (♦, unit of Pa), and the mass flow rate (•, unit of SCCM) against baratron pressure.

controller. The relation between the mass flow rate and the gas pressure is also calibrated annually against an MKS Baratron capacitance manometer. Provided that any change of the pumping speed can be neglected between the two calibrations, the reading of the mass flow meter can be converted into the gas pressure. It turns out that as a way to measure the gas pressure, the reading of the mass flow meter is more reliable than that of the penning gauge, owing to pollution of its cathode. This is a slow but uncertain increasing function of discharge running time, and affects the gauge reading to a certain degree. Hence the reading of the mass flow meter is used as both a double check of the gas pressure and a sign of the condition of the penning gauge. The relation between the mass flow and the Baratron pressure is also shown in Fig 2.2.

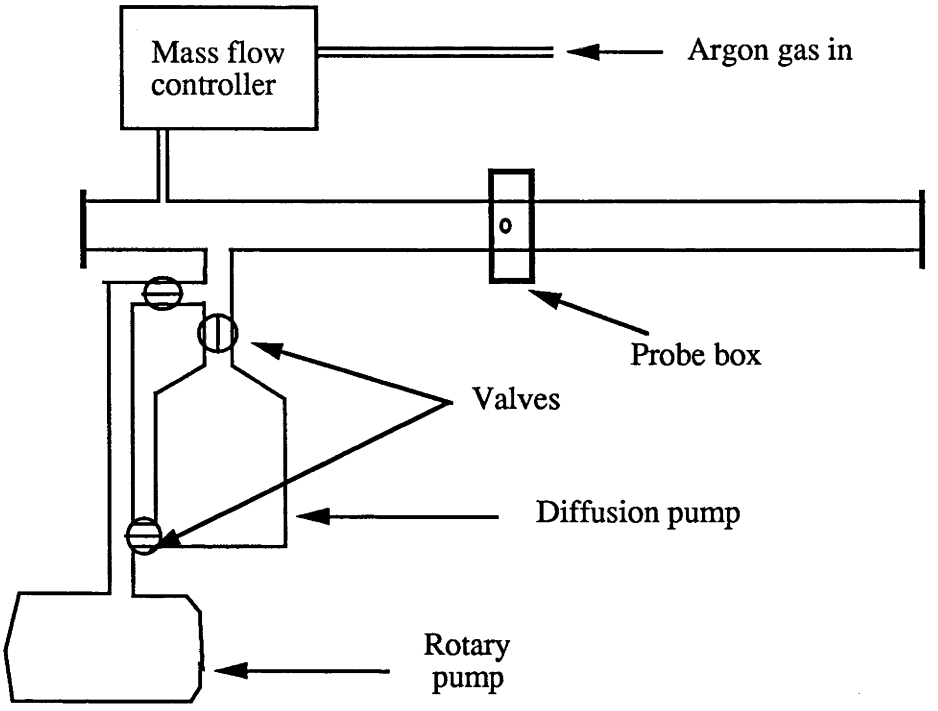

Figure 2.3: Vacuum system

Fig 2.3 shows the vacuum system together with gas feeding system. All the experiments are carried out using high-purity-grade argon with a minimum purity of 99.99%.

2.1.2 Magnetic field coils

To obtain a steady uniform longitudinal magnetic field in a length of about 1.2m, fourteen magnetic field coils are used. The coils are coaxially mounted with 11 cm separation between each (see Fig 2.1) and sit on a table supported by the main frame. These fourteen magnetic field coils can produce a longitudinal magnetic field up to 0.2T with a uniformity $\sim$ 3% inside the 1.2m long region of the coils.

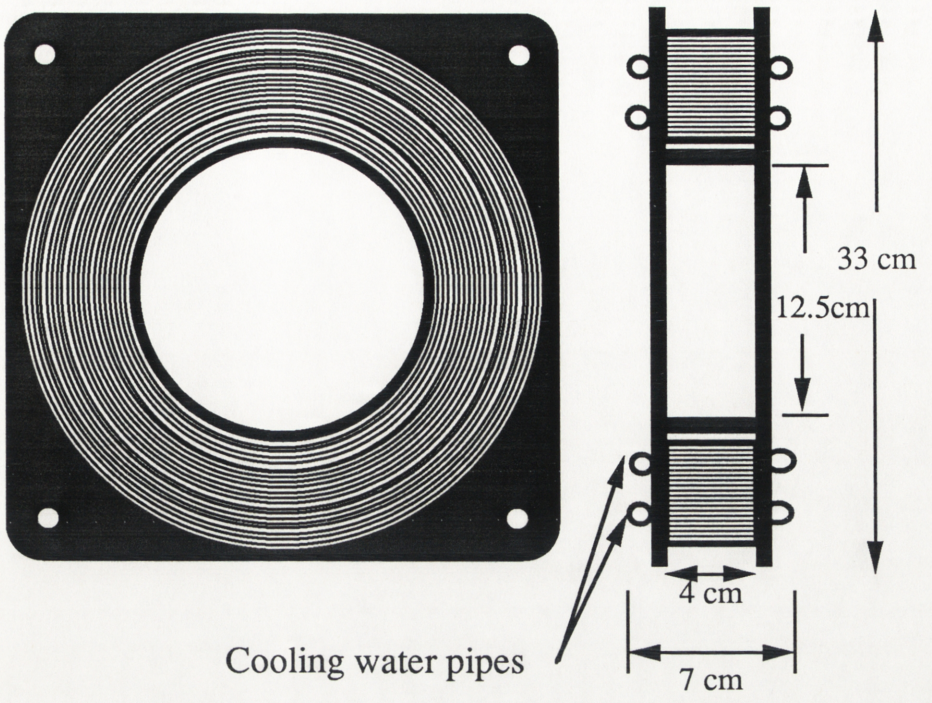

Figure 2.4: Magnetic field coil

Fig 2.4 shows a sketch of a single coil and Fig 2.5 shows an example of the magnetic field on the axis of the system produced by the coils for a current of 25A.

2.2 RF antenna and rf power supply

A double-loop antenna is used to generate an oscillating magnetic field perpendicular to the axis inside the discharge tube, which in turn excites helicon waves in the discharge. This kind of antenna (shown in Fig 2.6) is known to efficiently produce a highly ionized plasma [13]. RF power is fed to the antenna via a capacitive matching network (also shown in Fig 2.6). A Kenwood TS-520S transceiver is used to drive two rf linear amplifiers in series (Kenwood TL 922 and Alpha

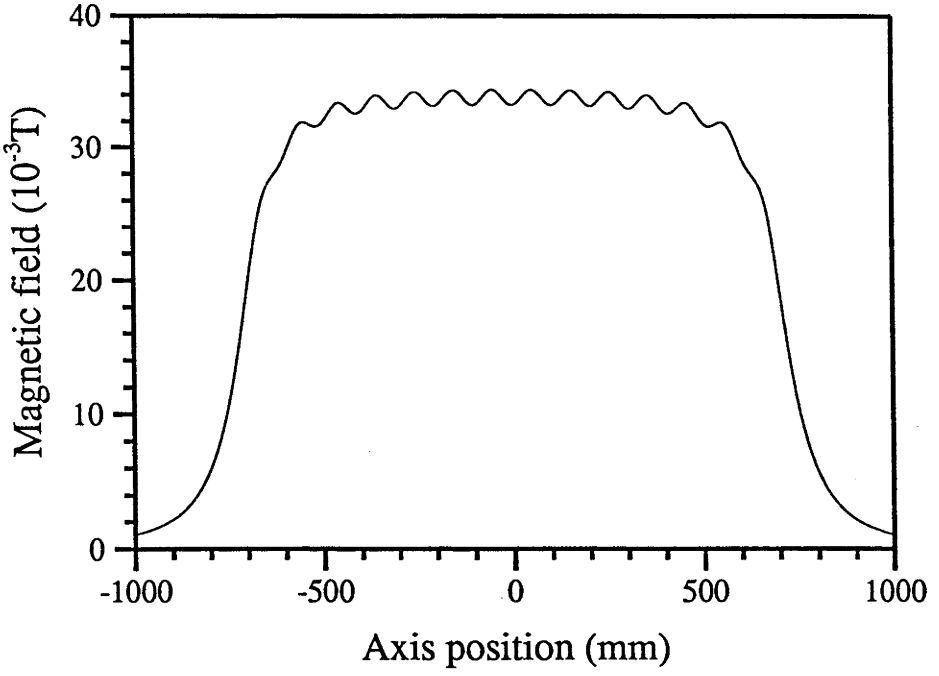

Figure 2.5: Longitudinal magnetic field produced by 14 coils for electrical current of 25A

DX77) to obtain rf power outputs up to 5 kW at 7–14 MHz. A pulse generator is used to pulse the rf transceiver and trigger the data collection system. Most of the experiments have been carried out at 7 MHz with pulses of 5–10ms duration and 10–20% duty cycle with rise time of $\sim 10^{-5}$sec.

2.3 Data collection system

The data collection system used in this study was designed and developed by a former PhD student, Arnstein Prytz. The system is based on an Apple II microcomputer and has the functions of controlling data collection, data storage and some simple data processing such as curve smoothing or scale changing. The highest data collection rate of this system is 70000 samples per second, and the resolution of the system is 8 bits. The system also has the ability of transferring

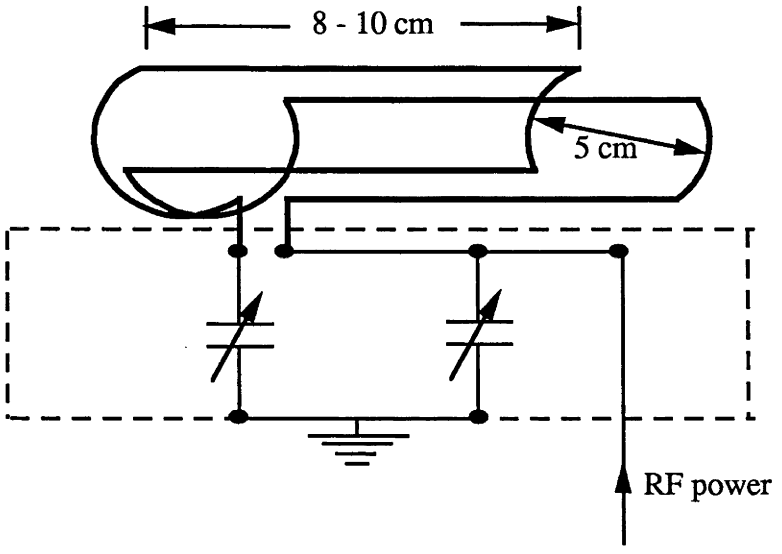

Figure 2.6: RF antenna

data files to a Vax11/785 computer on which more complicated data treatment can be carried out.

The signal required by the data collection system is a peak-peak voltage within the range of ± 5V. Any experimentally measured signal must first be changed into a voltage signal within the required range and then be fed into the data collection system.

Chapter 3

Diagnostics

This chapter describes the diagnostics involved in this study together with the theory associated with each measurement.

Sections 1 of this chapter describes the methods for investigating the optical properties of the discharge, especially the spontaneous and stimulated emission of the 488 nm argon ion line. In order to obtain reliable results, two independent methods are applied to determine the electron density. One is the Langmuir probe method (section 2) and the other is the microwave interferometer method (section 3) . The electron energy distribution is investigated also by means of a Langmuir probe while a magnetic probe (section 4) is used to measure the helicon wavelength in the discharge.

3.1 Optical diagnostics

In order to study the potential application of a discharge in the laser field, the knowledge of the spontaneous and the stimulated emission of the laser operation

lines is essential. Standard spectroscopic methods are applied to investigate the relative intensities of the spontaneous emission for several argon ion lines under different experimental conditions. A beam from an Ar^+ laser operated at the 488 nm line is used as an optical probe to measure the optical gain, which is the balance of the stimulated emission over absorption, of the 488 nm Ar^+ line radiation from the discharge.

3.1.1 Spontaneous emission measurement

The equipment required for a relative analysis of atomic or ionic spontaneous emission is one of the least complicated. It requires a monochromator to disperse the optical emission and a set of optics to image light from the discharge onto a photodetector. In this study, an optical fibre with a 0.8mm wide, 1cm long end is mounted on a mechanically scanning system to allow the side-on scanning of spontaneous emission from the middle of the discharge column. The system is located at the image surface of the optical system and the scanning resolution is about 2mm. A sketch of the whole arrangement used in this study for the relative analysis of the spontaneous discharge emissions is shown in Fig 3.1. Since the emissions to be studied in this case consist of the visible or UV lines of the argon ion and only their relative intensities are required, a 1m monochromator (McPherson Model 2051), which has a maximum spectral resolution of 0.01nm, can easily satisfy the requirement. An EMI 9816QKAM photomultiplier tube

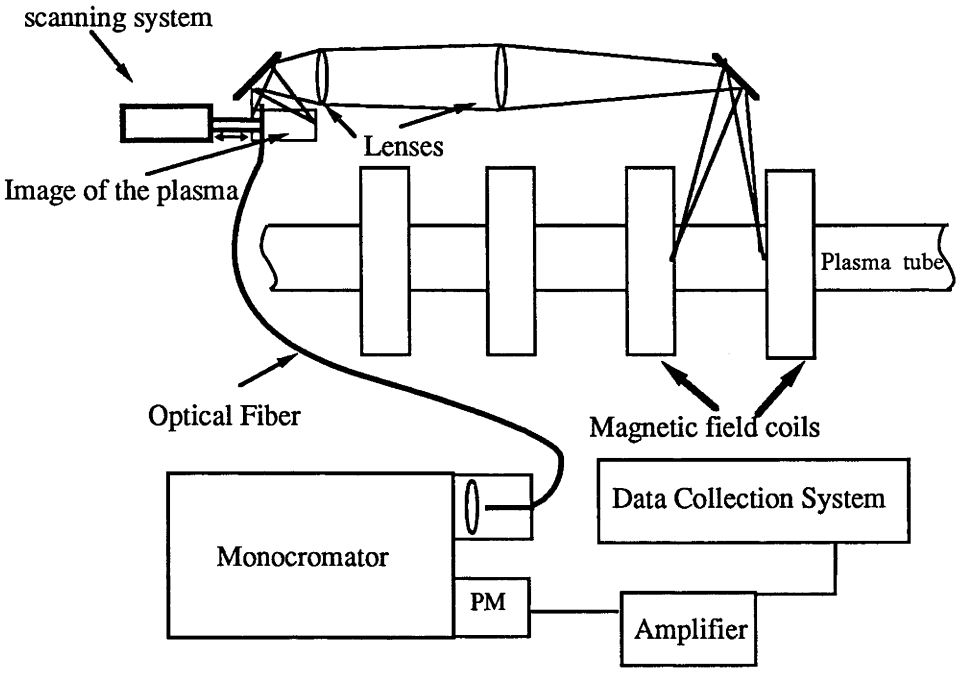

Figure 3.1: Experimental arrangement for spontaneous emission measurement

Wavelength (nm)	Relative Responsivity	Wavelength (nm)	Relative Responsivity
300	0.01	460	0.92
330	0.110	480	0.856
350	0.524	500	0.757
370	0.771	550	0.540
400	0.965	600	0.341
420	1.000	650	0.199
440	0.974		

Table 3-1. Spectral response of the monochromator-pm system

mounted at the exit slit of the monochromator is used as the detector. The relative spectral response of the whole system (Table 3-1) is calibrated against a quartz-window, tungsten-ribbon standard lamp.

The relative intensities of the spontaneous emissions of a plasma can directly provide information about electron temperature, relevant excitation state densities and electron density if the plasma under study is either in local thermodynamic equilibrium(LTE) or coronal equilibrium. The coronal domain is roughly bounded by the condition [20]

$$n_e < 2 \times 10^{-1}(z+1)^{-1}T^4\mathrm{m}^{-3} \tag{3.1}$$

whereas the LTE is reached at densities approximately [20]

$$n_e > 1.5 \times 10^{21}(z+1)^6T^{1/2}\mathrm{m}^{-3} \tag{3.2}$$

where T is the electron temperature in K and z is the effective charge and for single ionization system z=1. The electron temperature of the Basil-II discharge is about 3×10^4 to 6×10^4K. Neglecting any double ionization in Basil-II discharge, one can rewrite the conditions as

$$n_e < 10^{18}\mathrm{m}^{-3} \tag{3.3}$$

for coronal domain and

$$n_e > 1.6 \times 10^{25}\mathrm{m}^{-3} \tag{3.4}$$

for LTE.

The electron density of the plasma in this study lies in the range $10^{19}\mathrm{m}^{-3}$ to $10^{20}\mathrm{m}^{-3}$. This is far from that required by LTE and also exceeds the condition for a coronal equilibrium. Thus neither the LTE model nor the coronal model can be applied.

Although neither LTE nor coronal conditions are valid in this study, the time-resolved spontaneous emissions from different excitation states and ionization states can give directly useful information about the relevant states, especially the variation with time of their relative populations without involving any complicated theories.

3.1.2 Optical gain measurement

The optical gain of the laser operation line is the most important property of a discharge for laser applications. If the optical gain of a line in the system is positive, and exceeds the total loss of the system, the radiation of this line in the optical cavity is amplified by stimulated emission, resulting in laser action.

Since the net intensity enhancement of a line is proportional to the total intensity of the emission, it is possible to use a beam of laser light of the same wavelength to probe the gain. If the intensity of the laser light is much higher than the spontaneous emission of the same wavelength from the discharge, but is weak enough to avoid nonlinear effects, the enhancement of the light intensity is approximately proportional to the intensity of the laser light.

The experimental arrangement shown in Fig 3.2 is used in this study to measure the single pass longitudinal optical gain. The 488 nm probing laser beam has a divergence of 0.6×10^{-3}rad and the size of the beam is limited by a 1mm diameter aperture before it enters the discharge. Thus the optical probe can measure the optical gain in a narrow volume with a diameter of $\sim$ 1 mm throughout the discharge. By moving the probing beam one can investigate the radial variation

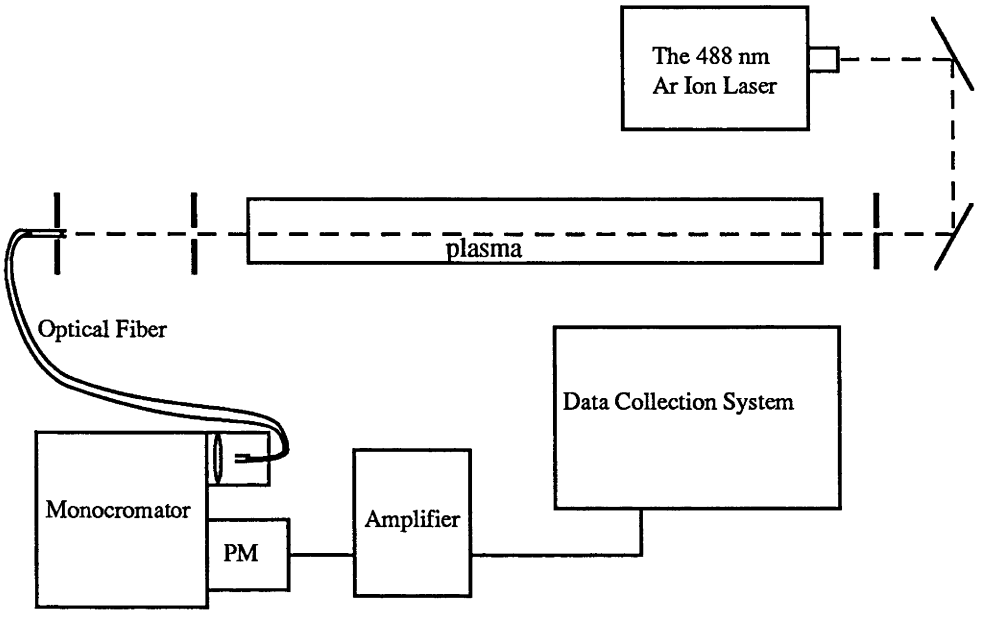

Figure 3.2: Experimental arrangement for gain measurement

of the optical gain with a resolution ~1mm. The monochromator here serves as a selective filter so that only the 488 nm line can reach the collection system. The probing laser is operated at TEM_{00} single mode and the line width(on the order of 10^{-5}nm) of the laser beam is much narrower than that of the emission from the discharge (on the order of 0.01nm) and it is totally overlapped by the emission. The detected gain structure in this case is mainly determined by the laser mode structure. Hence the detected gain can be taken as a very good estimate of the gain for the centre frequency of the line ($G(\lambda_0)$. Using the system shown in Fig 3.2, three signals (I_1, I_2, and I_3) can be recorded when the experiments are carried out under the following conditions:

I_1: laser on, discharge off;

I_2: both laser and discharge on;

I_3: laser off, discharge on.

Here I_2 is the sum of the intensities of the laser light and the stimulated and spontaneous emission from the discharge, with the concept of negative stimulated emission for absorption, and I_1, I_3 represent the laser intensity level and the spontaneous emission intensity respectively.

From the definition of the gain per pass, it is easy to write:

$$G = ln\frac{I}{I_0} = ln\frac{I_2}{I_1 + I_3}.$$

If $G \ll 1$, the above can be simplified as

$$G = \frac{I_2 - I_1 - I_3}{I_1 + I_3} \tag{3.5}$$

If the intensity of the laser light is much higher than that of the spontaneous emission from the discharge, ie. $I_1 \gg I_3$, one has:

$$G \simeq \frac{I_2 - I_1}{I_1}. \tag{3.6}$$

In the experiments, the laser intensity is so chosen that it is strong enough to use Eq.3.6, and weak enough to avoid nonlinear effects ensuring that the gain measured is the small signal gain.

3.2 Langmuir probe

For the propose of discussion, a Maxwellian distribution for bulk electrons is assumed, although(see later)there is a clear indication of a nonthermal electron distribution in this discharge. The effect of the magnetic field and rf oscillating fields on the probe characteristic must be taken into account to get reliable results. The rf field in the plasma will cause an oscillation in probe potential with respect

to the plasma. For a plasma with standing helicon waves, as in our case, this effect can be minimized by carefully choosing the diagnostic position to be at a wave node, where the rf field in the plasma minimum. The magnetic field will cause a reduced current to the probe if the gyroradius of the charged particles is much smaller than the probe dimension. In this study, it is assumed that the effect of the magnetic field on the probe measurement can be neglected if the ratio of gyroradius to probe radius ≥ 1.

Although modern probe theories have covered a great variety of plasma states [21], there is no universal formula to interpret the experimentally measured V-I characteristic of a Langmuir probe immersed in a plasma. Probe theory can derive a probe characteristic only when the form of the electron distribution in the plasma is known, and in most non-maxwellian distribution cases the characteristic can be obtained only through a process of numerical integration. That means for plasmas with a non-maxwellian electron distribution, the interpretation of the Langmuir probe characteristic has to be treated case by case. A detailed discussion of complete Langmuir probe theory is out of the scope of this study, and only the treatment of this particular plasma case will be discussed in this section.

The remainder of this section describes the Langmuir probe system, the probe characteristics measured in Basil-II, and their interpretation.

3.2.1 Langmuir probe system

A vacuum-tight probe box is used to mount a radially movable single Langmuir probe. The probe box can be fitted in the gap between two magnetic field coils, so that the longitudinal distance between the middle of the antenna and the probe can be (16+11n)cm (n = 0, 1, ... 4). In most of the experiments carried out in this study, the probe box is located in the gap adjacent to the one which hosts the antenna, where a minimum rf level is measured by a magnetic probe, so the distance from the middle of the antenna to the probe is 16 cm. A 0.3mm diameter tungsten wire is used to form a single cylindrical Langmuir probe. The construction of the probe and a sectional view of the probe mount are shown in Fig 3.3.

In a plasma with a magnetic field, the probe characteristic could be effected if the gyroradius of the charged particles ($\rho_{e,i}$) is much smaller than the radius of the probe(r_p). Table 3-2 shows $\rho_{e,i}/r_p$ as function of the charge carrier energy for B_0 = 0.08T, r_p = 0.15mm. From Table 3-2, one can see that the probe characteristic will not be strongly affected by the magnetic field when the probe potential is more negative than -20V. However, for a less negative probe, the effect of the magnetic field can cause serious experimental error. Thus this probe is not very good for studying low energy electrons but is suitable for studying both ions and high energy electrons.

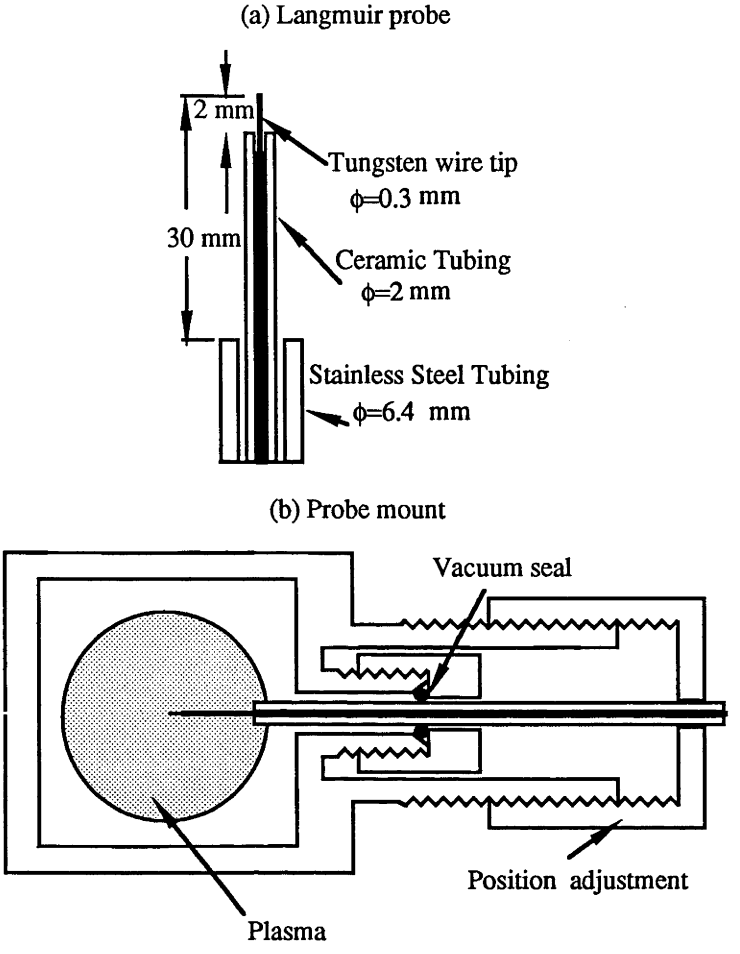

Figure 3.3: Construction of radially adjustable langmuir probe

Type of Charge Carrier	Energy Range (eV)	$\rho_{e,i}/r_p$
Electron	0 - 10	0 - 0.63
	10 - 20	0.63 - 0.88
	20 - 40	0.88 - 1.25
	40 - 100	1.25 - 2
Ar^+ Ion	0.5 - 1	38 - 53.75

Table 3-2. $\rho_{e,i}/r_p$ for $B_0 = 0.08$T and $r_p = 0.15$mm

3.2.2 Probe characteristic

In this subsection, the details of the Langmuir probe characteristic measured in Basil-II will be discussed. A typical probe characteristic obtained from Basil-II plasma (Fig 3.4) can be divided into four regions:

A. Positive ion collection region

In this region, the probe is so strongly negatively biased that few electrons can penetrate the probe sheath. The characteristic is mainly determined by positive ion current and is nearly independent of the form of the electron distribution provided the distribution is not too far from Maxwellian. Since the heavy ions are hardly magnetized in this case, the magnetic field has little effect on the characteristic. The ion current detected is proportional to the electron density if only singly ionized ions are collected and the ion temperature is much less than the electron temperature [22]:

$$I_+ \simeq 0.6 n_e e (\frac{kT_e}{m_i})^{1/2} A_s \tag{3.7}$$

where A_s is the area of the sheath surface which does not differ from the area of the probe for the normal case, although there is some slow increase in A_s as the probe is made more negative. This means I_+ is only very weakly dependent on the probe potential so the effect of the rf field inside the plasma on the characteristic is negligible. The characteristic in this region can then be used to estimate the electron density [22]:

$$n_e \simeq \frac{I_+}{0.6 e A_s} (\frac{m_i}{kT_e})^{1/2}. \tag{3.8}$$

B. Nonthermal fast electron collection region

In this region, the probe potential with respect to the plasma is still sufficiently

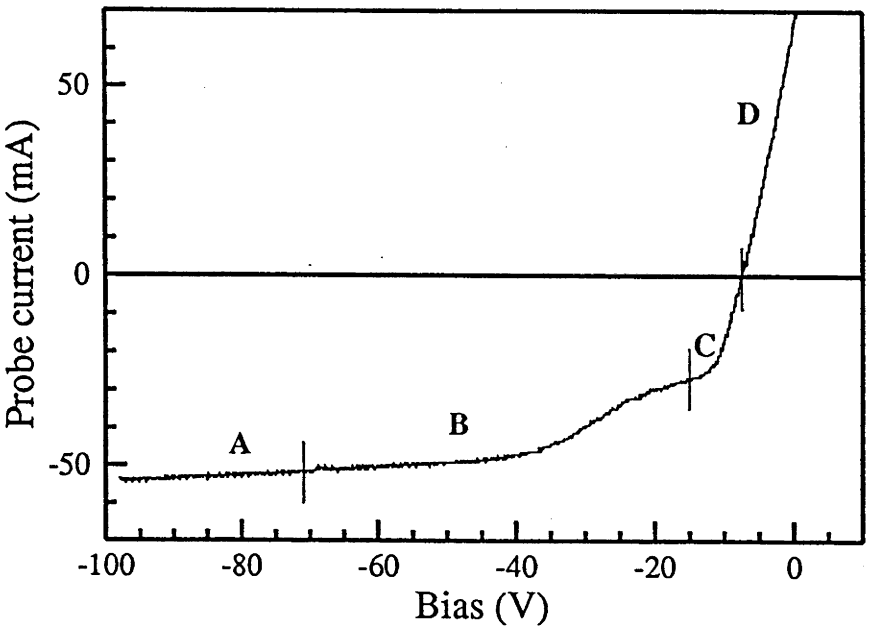

Figure 3.4: Typical probe V-I characteristic of Basil-II plasma for B_0=0.08T, P=0.9Pa, P_{rf} =3.5kW and rf=7MHz.

negative so that only very fast electrons can reach the surface of the probe. It is this part that provides information on the nonthermal electron tail since the number of thermal electrons in this energy range is negligible. It has been found that a calculated characteristic for a plasma which includes an electron beam can fit some of the measured characteristics quite well. The probe electron current for an electron beam can be written as [21]:

$$I_e = en_b\sqrt{\frac{T_b}{2\pi m_e}}exp(-x_m^2) + \frac{en_b v_b}{2}[1 + erf(x_m], \tag{3.9}$$

where

$$erf(x_m) \equiv 2\sqrt{\pi}\int_0^{x_m} exp(-x^2)dx, \tag{3.10}$$

and

$$x_m = \sqrt{\frac{E_b - eV_{probe}}{kT_e}}, \tag{3.11}$$

with E_b, the beam energy; v_{probe}, the probe potential with respect to the plasma and v_b the beam velocity. Note that T_b, the beam temperature, is a measure of the beam thermal spread and can be written as:

$$T_b \simeq \Delta E_b \frac{\Delta E_b}{4E_b} \tag{3.12}$$

where ΔE_b is the spread in the beam energy which corresponds to the half width of the beam distribution at the e^{-1} point.

The effect of the magnetic field on this part of the probe characteristic is not strong since the gyroradius of these fast electrons is about twice the probe radius. The derivative of probe current with respect to the probe potential is relatively small so rf fields do not play a major role, since the uncertainty of the probe current due to the rf is proportional to the derivative of the current:

$$\Delta I \simeq \frac{dI}{dV} \Delta V,$$

where ΔV is the rf level. In this region, an uncertainty of only $\sim$ 2eV in the determination of the electron energy could be involved due to the effect of the rf, which will cause a plasma potential variation $\sim$3-5V. Fig 3.5 shows a comparison of the theoretical characteristics both with and without the rf field.

C. Thermal electron collection region

The probe potential with respect to the plasma is still negative but some thermal electrons with high energy can reach the surface of the probe. Since these thermal tail electrons dominate the probe current in the characteristic, one can expect to get some information about the bulk electron temperature from this part.

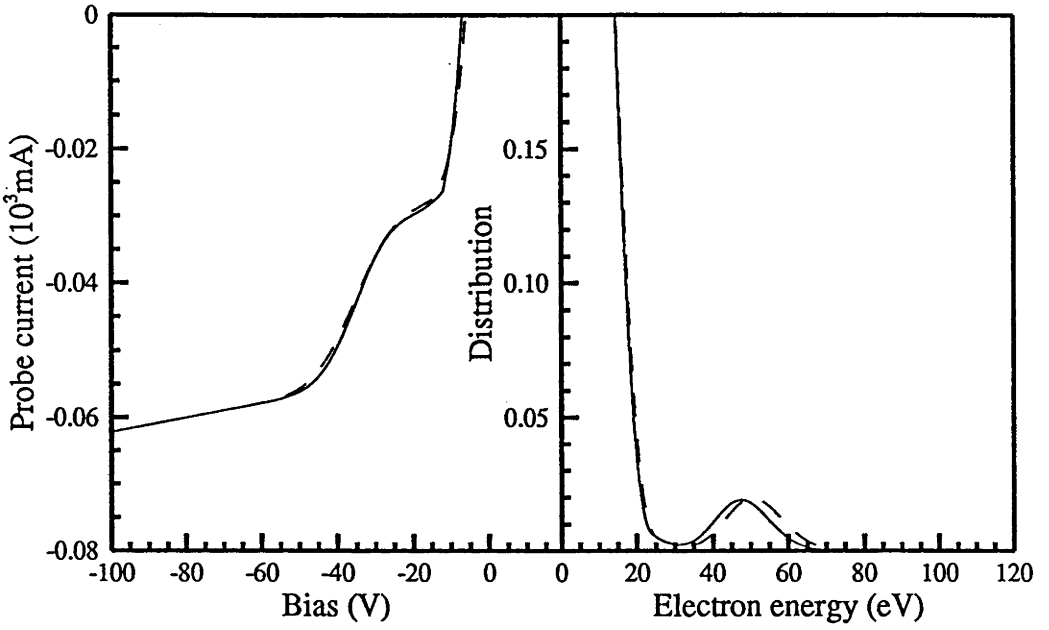

Figure 3.5: (a) Comparison of the theoretical characteristics both with (dashed line) and without (solid line) the rf field and (b) their corresponding distributions

However, there are several factors which may cause considerable errors in determining the bulk electron temperature. Firstly, those thermal electrons which can be collected are only a small fraction of the bulk electrons, and the distribution in this region is very likely to be distorted in some way. Secondly, as the gyroradii of the electrons in this energy range are of the same order as the probe radius, the magnetic field will have some effect on the probe characteristic. The effect of the rf field is also larger than in regions A and B since the derivative of the current with respect to probe potential is no longer negligible. Hence only a rough estimate of the bulk electron temperature can be expected.

D. The bulk electron region

When the probe potential with respect to the plasma is made less negative,

bulk electrons with low energy can be collected by the Langmuir probe. However the probe characteristic is strongly affected by the magnetic field since the gyroradii of these slow electrons is much smaller than the probe radius. The characteristic can be used to determine the bulk electron temperature only in those cases where such a weak magnetic field is applied that their gyroradii are similar to the probe radius. In Basil-II, this requires a magnetic field below 0.06T.

3.2.3 Interpretation of the probe characteristic

From the above discussion, it is clear that although the theory of the probe characteristic for the Basil-II plasma is quite complicated, the saturated ion current can still be easily identified. The extraction of the ion current from the characteristic is not difficult in practice, hence particular attention need only be paid to the electron current. In a magnetized plasma, since a Langmuir probe will collect those electrons which are travelling along the magnetic field [23], one can consider a one-dimensional case for simplicity. Although Langmuir probe theory normally becomes very complicated when a non-Maxwellian electron distribution is concerned, the original equation for the current density to the probe is still valid:

$$I = eA_{probe} \int_{v_{min}}^{\infty} f(v) v dv \tag{3.13}$$

where A_{probe} is the effective surface area of the probe. As mentioned before, there is no universal theory to derive the electron distribution from a probe characteristic unless the form of the distribution is known. Fortunately, from the measured probe characteristic, one can normally have a quite good guess of the form of the distribution, which in turn can be put into Eq. 3.13 to derive a correspond-

ing characteristic. By comparing the measured characteristic with the calculated one, another closer guess can then always be made. By iteration, the assumed distribution can be made so close to the real one that the calculated curve can reasonably fit the measured data. In practice, this method needs the knowledge of the plasma potential which is not easy to measure experimentally in this case, since applying a zero bias would result in such a large electron current being collected as to destroy the probe tip. An assumed figure within the range of 11-16V for the plasma potential is thus used in the interpretation of the measured characteristic. The uncertainty of the plasma potential will only cause a few eV shift in the tail of the electron distribution but can cause significant error in determining the bulk electron temperature, which, as has been shown above, can not in any case be measured accurately for other reasons. Hence, from this simple Langmuir probe measurement, only a rough estimate of the bulk electron temperature can be expected.

The iterative tracing method is used in this study to obtain the electron distribution from the measured Langmuir probe data. A typical sample of the fitting of a theoretical characteristic to a measured one is shown in Fig 3.6 together with the corresponding distribution function.

The actual distribution functions can be highly non-Maxwellian, which we chosen to mode with sum of three simple functions to obtain a good fit:

$$F = \sqrt{eV} \times (f_1 + f_2 + f_3) \tag{3.14}$$

where

$$f_1 = n_e \sqrt{\frac{m_e}{\pi T_e}} e^{-\frac{eV}{kT_e}}, \tag{3.15}$$

$$f_2 = S_1 \times f_1 \times e^{-S_2 \times \frac{e(V_r - V)}{kT_e}}, \tag{3.16}$$

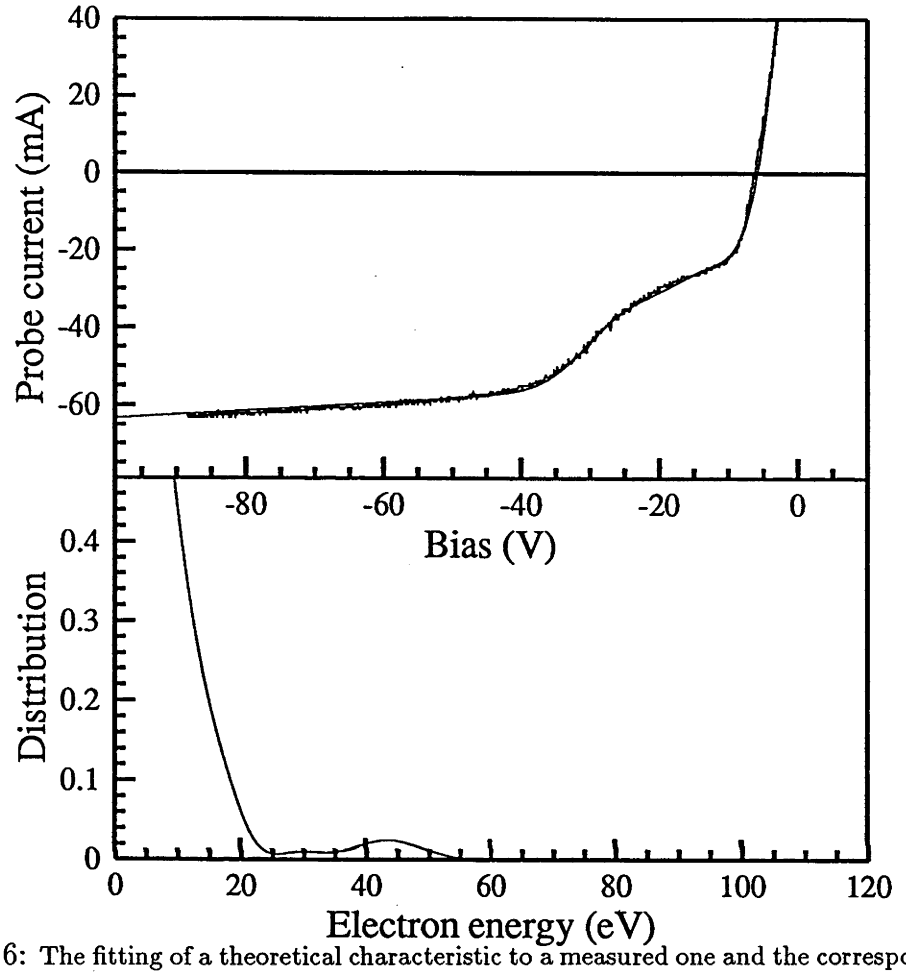

Figure 3.6: The fitting of a theoretical characteristic to a measured one and the corresponding distribution tail

here $0 \geq S_1 \geq -1$, and $S_2 \sim 10$ are adjustable parameters; and

$$f_3 = n_b \sqrt{\frac{m_e}{\pi T_b}} e^{-\frac{e|V_b - V|}{kT_b}}, \tag{3.17}$$

with $T_b \simeq \frac{\Delta E_b}{4E_b} \Delta E_b$ and ΔE_b is the beam e^{-1} spread half-width in eV. The error due to an uncertainty of 5V in the plasma potential for T_e is about 30%, for V_b about 5-10% and for relative beam density n_b/n_e about 20%. Hence the distribution can be represented by a few parameters, such as bulk electron temperature

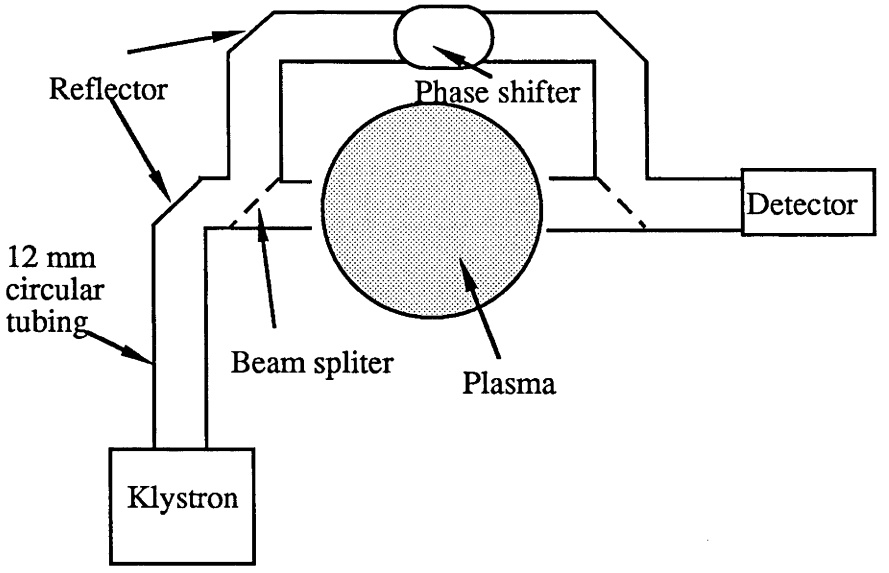

Figure 3.7: Experimental arrangement of microwave interferometer measurement

T_e, beam energy E_b, beam energy spread width ΔE_b, and the normalized beam density n_b/n_e.

3.3 Microwave interferometer

As an independent means of density measurement, a microwave interferometer (λ=3mm) is used to check the absolute density measured by the Langmuir probe. Fig 3.7 shows a schematic diagram of the microwave interferometer used in this study.

3.3.1 The principle of the method

The principle of the 3mm wavelength microwave interferometer used is that of the Michelson interferometer. The microwave power from a klystron is split into two beams. The two beams are combined again after traversing two different paths, i.e. a reference path and the main path through the plasma tube. The reference path is adjusted so that the output for the detector is zero in the absence of a plasma. The phase change due to the change of the microwave refractive index in the plasma can then be determined from the phase shift due to the two-beam interference [24]:

$$\theta = \frac{4\pi}{\lambda}\int_0^R \Delta N_r dl = \frac{4\pi}{\lambda}\int_0^R [1-(1-\frac{n}{n_c})^{1/2}]dl. \tag{3.18}$$

where ΔN_r is the change of the refractive index of the wave in the plasma and n_c is the cut-off density defined as:

$$n_c = \frac{m_e\omega^2}{4\pi e^2}, \tag{3.19}$$

where ω is the frequency of the microwave. If the plasma has a cylindrically symmetrical radial variation in electron density:

$$n = n_{e0}f(r)$$

where n_{e0} is the value of the central density and $f(r)$ is the radial density distribution function with $f(0) = 1$. Eq. 3.18 becomes:

$$\theta = \frac{4\pi}{\lambda}\int_0^R [1-(1-\frac{n_{e0}f(r)}{n_c})^{1/2}]dr. \tag{3.20}$$

Eq. 3.20 can be simplified when the condition $n_{e0}f(r)/n_c \ll 1$ is satisfied:

$$n_{e0} = \frac{\theta\lambda n_c}{2\pi\int_0^R n(r)dr}. \tag{3.21}$$

For a cylindrically symmetrical plasma, the volume mean electron density can be defined as:

$$\bar{n}_v = \frac{2n_{e0}\int_0^R r f(r)dr}{R^2}, \tag{3.22}$$

where R is the plasma radius.

3.3.2 Experimental considerations

The simple theory reviewed above is based on the assumptions of geometrical optics, perfect antennas, and negligible effect of the refraction due to the density variation. These assumptions should be checked from the experimental point of view.

The first assumption, geometrical optics, is valid when the plasma size D is at least three to five times the microwave length, eg. D$>$ 3 $\sim$ $5\lambda_0$ [25], [24]. In the Basil-II plasma, although the plasma tube diameter is 50mm, the radial distribution of the electrons is sharply peaked with a full width half maximum (FWHM) $\sim$ 14 mm. For a rough estimation, the FWHM of the profile can be treated as the effective plasma size, which is $\sim$4.7 times the wavelength in this case. This means the geometrical optics approximations can be used only if a rough estimation of the density is sufficient.

In Basil-II, the radial distribution of the electron density will cause considerable refraction of the beam direction. The refraction angle can be estimated by the equation [26]:

$$\phi(b) = sin^{-1}\frac{V_0[(\frac{b}{a})^2 - (\frac{b}{a})^4]^{1/2}}{[V_0(\frac{b}{a})^2 + (\frac{1-V_0}{2})^2]^{1/2}} \tag{3.23}$$

where b is the impact parameter and a is the tube diameter (Fig 3.8). Notice

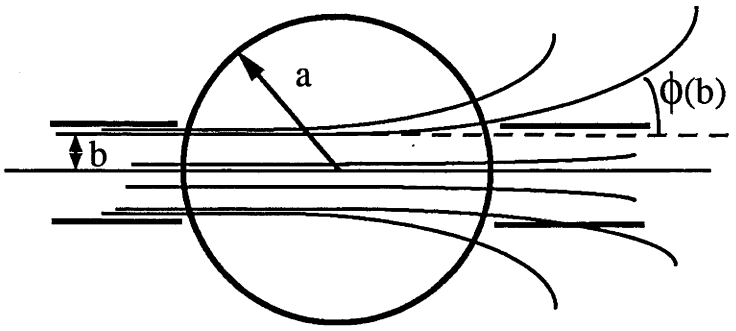

Figure 3.8: Refraction of the microwave

that $\phi(b) \rightarrow 0$ at the axis, hence for a single channel located at the axis with small collection angle, as is the case, the actual effect of the refraction is not really serious. Since the effect of the refraction will cause a somewhat lower cut-off density [25], it can also be checked from the earlier cut-off, if any, in the measured data. In this study, a peak density $\sim 0.7 n_c$ is estimated from the measured phase shift without observing any cut-off, confirming that the effect of refraction is negligible.

From the measured data, a value of $n_{e0} \sim 7 \times 10^{19} \mathrm{m}^{-3}$ for n_{e0} is estimated. Taking into account that in this case $n_c \simeq 1.24 \times 10^{20} \mathrm{m}^{-3}$, the condition $\frac{n_{e0} n(r)}{n_c} \ll 1$ does not always hold. Thus, to estimate the electron density from the measured phase change, Eq. 3.20 has to be used instead of Eq. 3.21. A program has been developed to solve Eq. 3.20 numerically for various phase changes and different FWHM (full-width half-maximum) of the Gaussian distribution profile, which is not far from the profile measured by Langmuir probe. The results are shown in Fig 3.9.

Since this simple interferometer can only provide information on the magni-

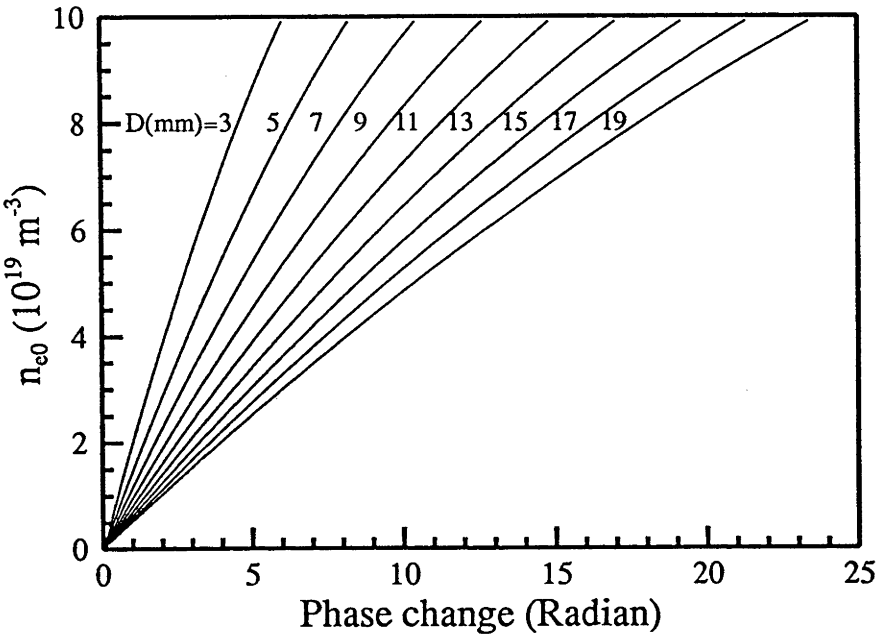

Figure 3.9: Central electron density as function of measured microwave phase change for various Gaussian profile width

tude of the phase change without its sign, it is necessary to identify the direction of the change during a pulse. This is simply done by comparison with the Langmuir probe data.

Although a detailed treatment based on wave optics could in principle be used to get more reliable results, the interpretation of the measured data is carried out using Eq.(3.20) for simplicity. Nevertheless, the result from this simple treatment agrees quite well with the result from the Langmuir probe measurement. The accuracy of the measurement can thus be estimated to be within a factor of 2.

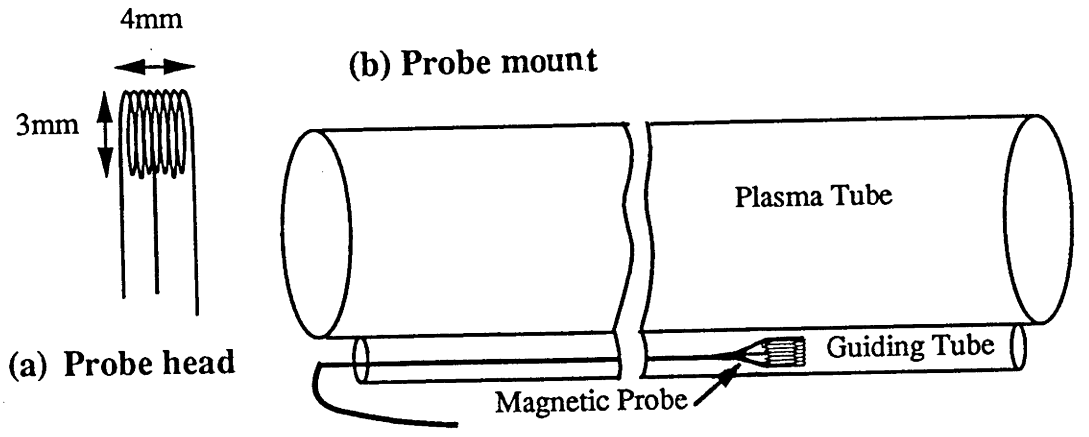

Figure 3.10: The construction of the magnetic probe and its mount

3.4 Magnetic probe

A magnetic probe is used to measure the helicon wavelength in the Basil-II plasma. The pick-up coil has a centre tap which is earthed to minimize electrostatic pickup. The construction of the probe is shown in Fig 3.10(a).

The probe is located inside a 7mm diameter glass tube, mounted parallel to the outer surface of the plasma tube (Fig 3.10(b)). The probe can be moved along the glass tube so that the external field of the helicon wave can be measured as a function of the longitudinal position. From the separation of the zero-field points or, as mentioned in Chapter 1 of this thesis, of the 180° phase-shift points, one can derive the wave number of the helicon wave. The fact that a clear 180° phase change is observed even when the probe is located outside the discharge tube suggests the helicon wave vector is not a strong function of the radial position. The measurement of the wave magnitude as a function of position, even a relative measurement, is not reliable since there are electrostatic pickup and other sources

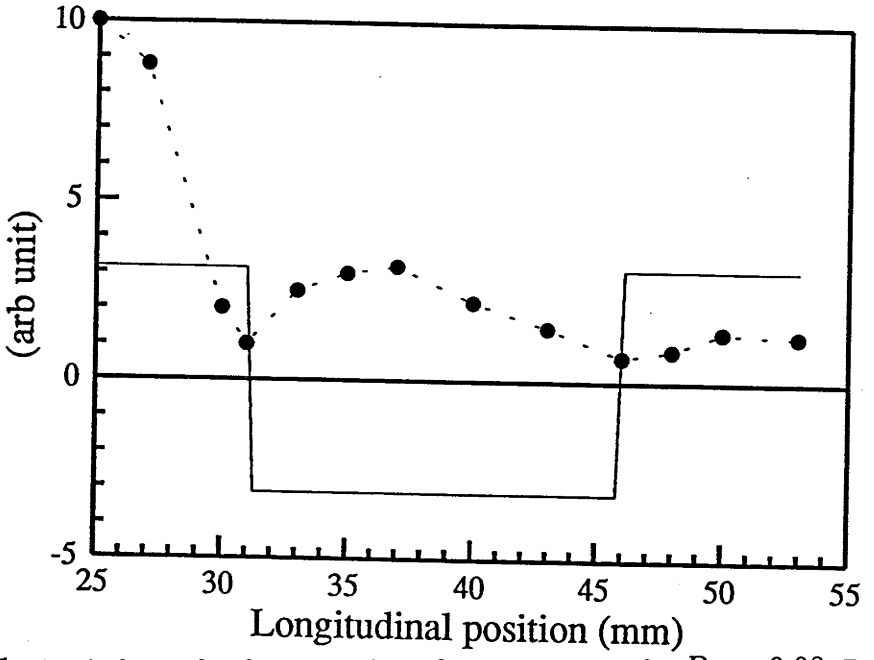

Figure 3.11: Typical sample of a magnetic probe measurement for $B_0 = 0.08$, P=0.9Pa, P_{rf} =4kW and measured at t=2ms

of interference even though a centre-tapped probe is used. Fortunately, the phase shift measurement is quite reliable, since a sudden 180° change in phase on the wave node is very easy to be experimentally identified.

Although an internal probe should be used to investigate the wave inside the plasma, there is evidence [27] that the measurements made outside the plasma column do correspond to the wave number inside the plasma. Fig 3.11 shows a typical sample of the results from the magnetic probe measurement.

Chapter 4

Optical properties of the plasma

To explore the possibility of using Basil-II as a laser, the knowledge of the optical properties of the plasma is essential. This chapter presents an investigation of the optical properties, especially those of the 488 nm laser operation line. The result of the investigation has not only positively confirmed that there is the possibility but also successfully led to a new argon ion laser whose special characteristics will be described in the next chapter.

The main part of this chapter describes the study of the spontaneous and the optical gain of the 488 nm Ar^+ line. The spontaneous emissions of some other Ar^+ lines are measured in order to get a rough picture of the spectrum under certain experimental conditions. Ar^{++} 350 nm emission is also measured for several conditions. Section 1 of this chapter will be devoted to the spontaneous and the optical gain of the 488 nm line for various experimental conditions, and the spontaneous emissions of some other Ar^+ and Ar^{++} lines will be presented in section 2. The results and several conclusions will be discussed in section 3 of this chapter.

4.1 The 488 nm line

This section will present the experimental results of the spontaneous emission and the optical gain of the 488 nm line. There are three good reasons to pay particular attention, as a starting point, to this line. First of all, the Ar^+ transition of 488 nm ($4p^2D_{\frac{5}{2}} - 4s^2P_{\frac{3}{2}}$) is the one of the strongest Ar^+ laser transitions. Secondly, a small Ar^+ laser operating at this line is available and can easily be used for probing the single pass gain. Thirdly, the 488 nm transition has the lowest current threshold for laser operation [28], so it is more likely to find gain in this line within the Basil-II plasma operation range.

The optical gain of a laser line is not a constant since the population of the laser transition upper level will be depleted by the stimulated emission. The single pass gain will then be reduced following the intensity of the transition[29]:

$$G = G_0 \frac{1}{1 + I/I_{sat}}, \tag{4.1}$$

where G_0 is the single-pass small-signal gain and $I_{sat} = \frac{h\omega}{\sigma\tau_{eff}}$ is the the intensity level at which the gain will be reduced to half of its original value G_0, where σ, and τ_{eff} are the laser transition cross section and the effective recovery time respectively. However, if the intensity of the emission is weak enough that $I/I_{sat} \ll 1$, then the gain is not sensitive to the emission intensity and is very close to G_0 which is a reflection of the population inversion of the unperturbed plasma. The small signal gain is of particular interest in this study since the maximum possible laser output intensity is proportional to it[29]:

$$I_{max} = G_0 I_{sat}. \tag{4.2}$$

Later on, for convenience, G_0 will be used for the gain unless otherwise stated.

4.1.1 Radial profile

The radial profile of the spontaneous emission and that of the optical gain have been investigated within the following experimental ranges:

B_0 : 0.050 - 0.140T for spontaneous emission;

B_0 : 0.065 - 0.100T for optical gain;

filling argon pressure : 0.4 - 1.5Pa;

input rf (7 -14 MHz) power : 3.5kW;

tube diameter : 30 - 56mm.

The reason for the smaller B_0 range for the gain is that only in this range can the profile be measured with reasonable accuracy. All the profiles are measured at a time of 2 ms after the plasma is turned on, when the plasma reaches a relatively steady state.

The spontaneous emission is scanned side-on across the tube to get a profile while the radial profile of the single-pass gain is scanned end-on. It is found that both profiles of spontaneous emission and optical gain have quite narrow FWHM no larger than 1.2 cm for most of the experimental conditions. Fig 4.1 shows a typical example of the measured profiles of both the spontaneous emission and the optical gain. Both profiles are measured under the same experimental condition of $B_0 = 0.075$T, rf 7MHz, and tube diameter 45mm. The side-on scanned profile is not the true emission radial profile and an Abel inversion should be carried out[30]. However, if the measured profile is a Gaussian distribution, this treatment is not necessary since the Abel inversion of a Gaussian distribution is also a Gaussian. This can easily be verified. From the Abel law, one has[31]:

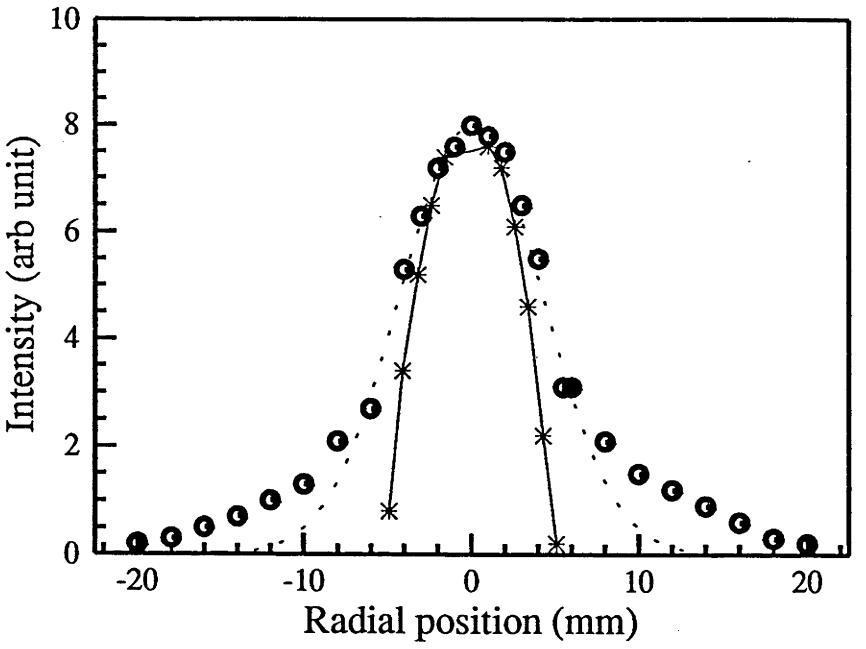

Figure 4.1: Radial profiles of spontaneous emission (o) and optical gain (*) of the 488nm transition for B_0=0.08T, P_{rf}=3.5kW, P=0.9Pa.

$$I(y) = \int_{|y|}^{R} \frac{r\epsilon(r)}{(y^2 - r^2)^{1/2}} dr; \tag{4.3}$$

$$\epsilon(r) = -\frac{1}{\pi} \int_{r}^{R} \frac{dI(y)}{dy} \frac{dy}{(r^2 - y^2)^{1/2}}, \tag{4.4}$$

where $I(y)$ and $\epsilon(r)$ are the measured profile across the tube and the radial profile respectively. Put $I(y) = Ae^{-\alpha y^2}$ into Eq.(4.4):

$$\epsilon(r) = -\frac{1}{\pi} \int_{r}^{R} \frac{dI(y)}{dy} \frac{dy}{(r^2 - y^2)^{1/2}} = \frac{2\alpha}{\pi} \int_{r}^{R} \frac{yI(y)}{(r^2 - y^2)^{1/2}} dy. \tag{4.5}$$

Notice that Eq.(4.5) has the same form as Eq.(4.3), applying Abel's law again one obtains:

$$I(y) = -\frac{1}{2\alpha} \int_{|y|}^{R} \frac{d\epsilon(r)}{dr} \frac{dr}{(y^2 - r^2)^{1/2}} \tag{4.6}$$

Comparing Eq. (4.3) with Eq. (4.6), one can find

$$\frac{d\epsilon(r)}{dr} = -2\alpha\epsilon(r). \tag{4.7}$$

The solution of the Eq.(4.7) is simply a Gaussian distribution with same FWHM:

$$\epsilon(r) = A^* e^{-\alpha r^2},$$

where A^* is a constant. Since in our plasma, the measured profile across the tube is a reasonab fit to a Gaussian distribution, it is treated as the radial profile without processing via an Abel inversion. A trial calculation of the radial profile suggests the FWHM of the measured profile can be taken as that of the emission profile without introducing much error (Fig.4.1b).

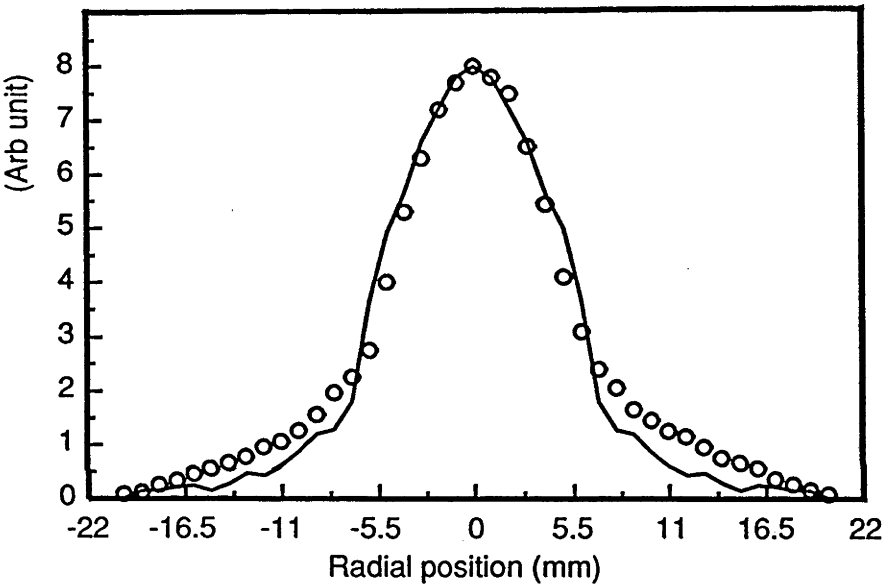

Fig.4.1b Measured profile (o) and its Abel inversion (solid line)

The FWHM of the profile as a function of rf and argon filling pressure are shown in Figs 4.2 and 4.3 respectively. The results are obtained from B_0 = 0.075T for both figures and P=0.5Pa for Fig 4.2, 7MHz rf for Fig 4.3. The FWHM as a function of the magnetic field is shown in Fig 4.4 with 7MHz rf, tube diameter of 45mm and filling pressure of 0.9Pa. From Figs 4.2 to 4.4, it is clear that the FWHM is a constant ~8mm for all the experimental conditions but the profile of the spontaneous emission is sensitive to the magnetic field in

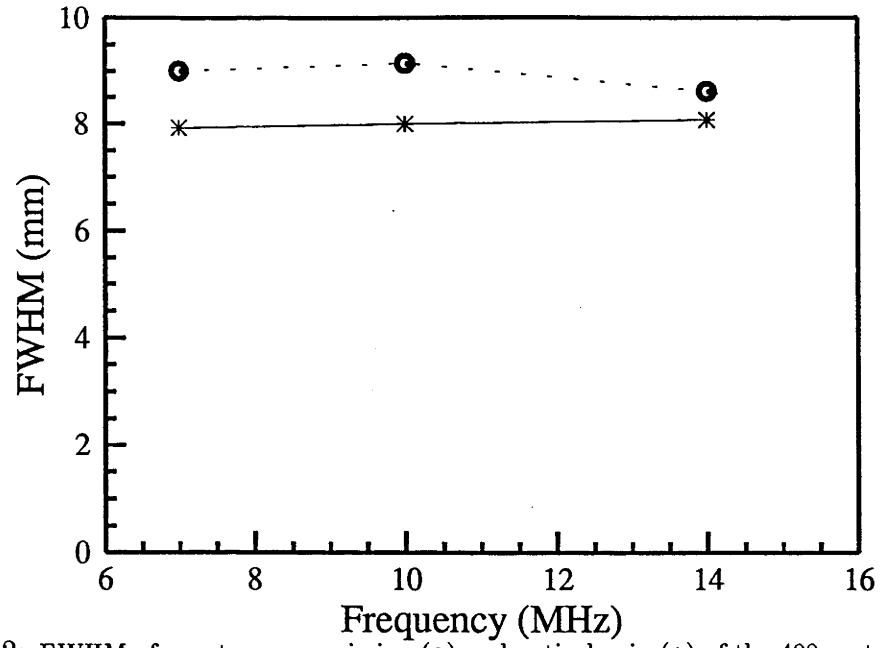

Figure 4.2: FWHM of spontaneous emission (o) and optical gain (*) of the 488nm transition as a function of radio frequency.

some ranges. Fig 4.5 shows that the FWHM of the profile for the spontaneous emission and the optical gain do not depend greatly on the plasma tube diameter. This suggests that the interaction between the tube wall and the plasma is not very strong and the plasma is confined in some way which is nearly independent of the tube wall over the range studied. The increase in width of the spontaneous emission profile follows the magnetic field (Fig 4.4) when B_0 >0.09T suggests some other confinement mechanism rather than magnetic field confinement. The sudden drop in FWHM in Fig 4.4 for the spontaneous emission at the magnetic field ~0.06T suggests a threshold B_0 field for a certain mode.

The spontaneous emission of a transition (E_{sp}) is proportional to the density of its upper excited state while the optical gain (G_0) is proportional to both upper state density and degree of population inversion

$$E_{sp} \propto n^*_{up};$$

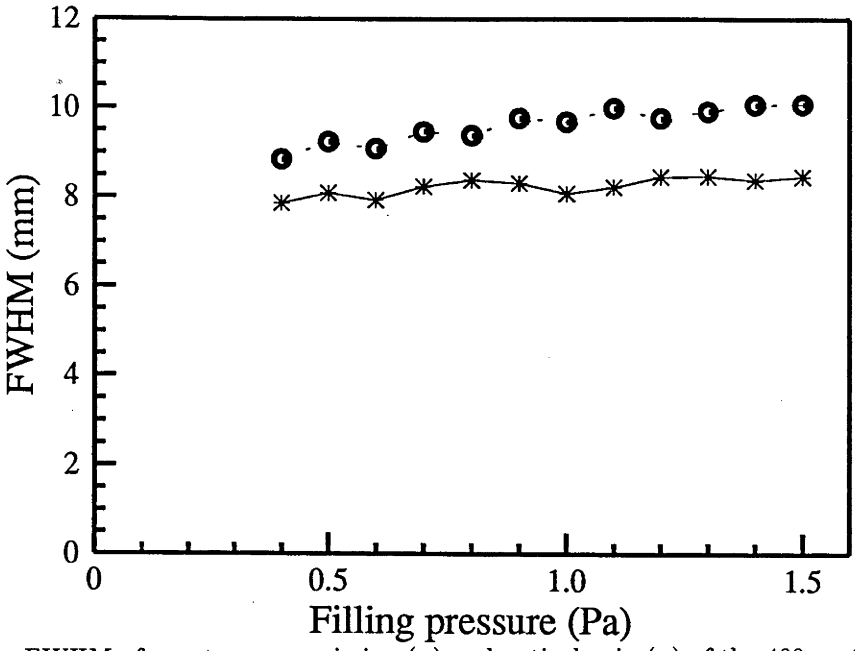

Figure 4.3: FWHM of spontaneous emission (o) and optical gain (*) of the 488nm transition as a function of argon filling pressure.

$$G_0 \propto n^*_{up} \frac{n^*_{up} - n^*_{lo}}{n^*_{up}},$$

where n^*_{up} and n^*_{lo} are the populations of the upper and lower states of the transition. The fact that the profile of the optical gain is always narrower than that of the spontaneous emission suggests a somewhat higher degree of population inversion in the centre of the plasma. This is not a surprising result since the plasma is generated by the m=1 helicon wave excited by the rf field of the double antenna, and the wave field has its maximum on the axis[12], resulting in a stronger excitation there.

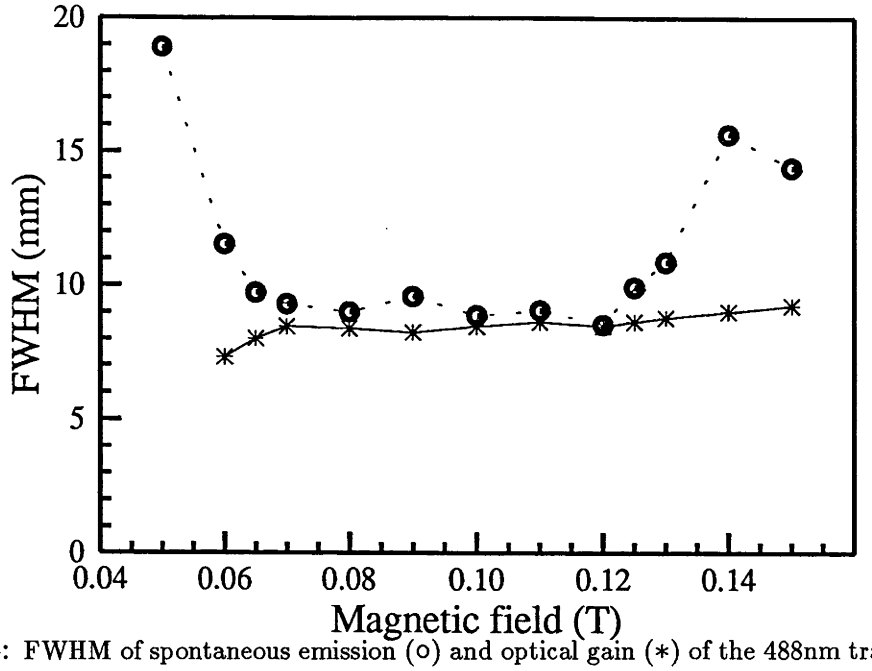

Figure 4.4: FWHM of spontaneous emission (o) and optical gain (*) of the 488nm transition as a function of magnetic field.

4.1.2 Time evolution

The Basil-II plasma is excited with pulse of 5-10ms duration. It is find that the discharge is not sensitive to changes in the pulse duty cycle over quite a large range from 2% to 50%; however, lower duty cycles means that it takes a longer time to collect the data, while too high a duty cycle will risk overheating the RF power source. Hence an intermediate value of 10% - 20% is used. During this 5-10ms, the plasma varies and the time evolution of the various emissions will be discussed in this subsection. Fig 4.6 shows a typical example of the spontaneous emission and the gain time evolution of the gain. This is measured along the axis of the plasma with B_0=0.075T, P=0.9Pa, rf power of 3.5kW at 7MHz. The whole evolution can be roughly described in terms of three characteristic times, t_1, t_2, and t_3. Here t_1 is the first 0.2~1.5ms, when the emission increases to ~0.6 of its peak value. During the rise time t_1, the excitation of the 488nm transition,

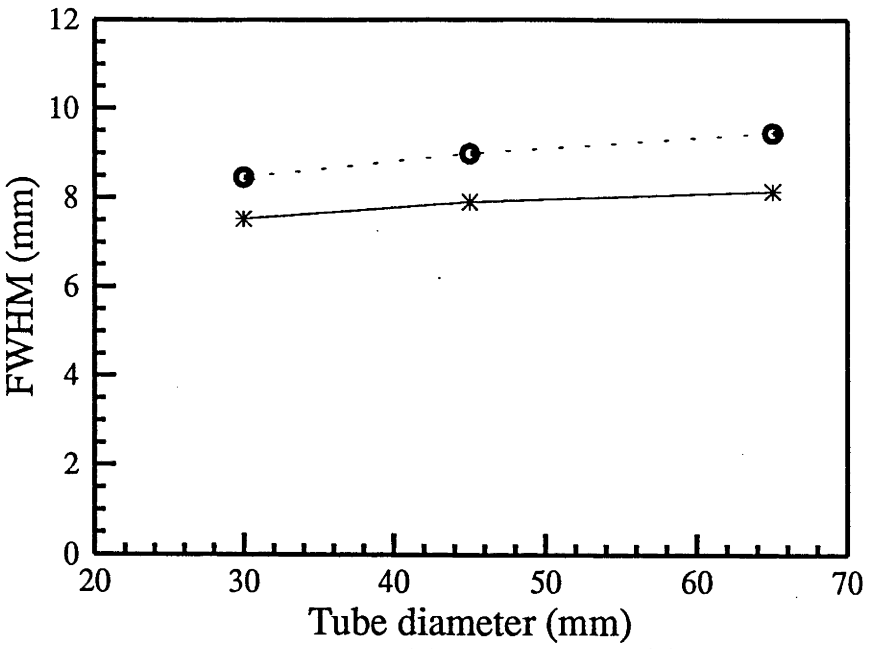

Figure 4.5: FWHM of spontaneous emission (o) and optical gain (*) of the 488nm transition as a function of tube diameter.

which depends on both electron density and the electron energy distribution, is increasing. In the next 2~5ms(t_2), the emission reaches its peak value and remains relatively steady. It is during this time t_2 that the maximum excitation of the upper state of the 488nm transition is reached and considerable optical gain is observed. After t_2, both the spontaneous emission and the gain drop to a much lower level, and the plasma finally reaches a steady state which can last for a long time t_3 (until the input power is switched off). The sudden change in the emission suggests a major change in rf-plasma coupling due to the change of plasma impedance. This is supported by the fact that the FWHM also widens at the same time (Fig 4.7). The whole time evolution can thus be divided in to a 'head' and a steady 'tail'. The former can roughly be represented by $t_1 + t_2$. It is found that in a repeated pulse mode, if the interval between consecutive pulses is not long enough, t_1 will depend somewhat on the pulse separation time and the shorter the separation, the shorter the t_1. This can be explained by a higher level

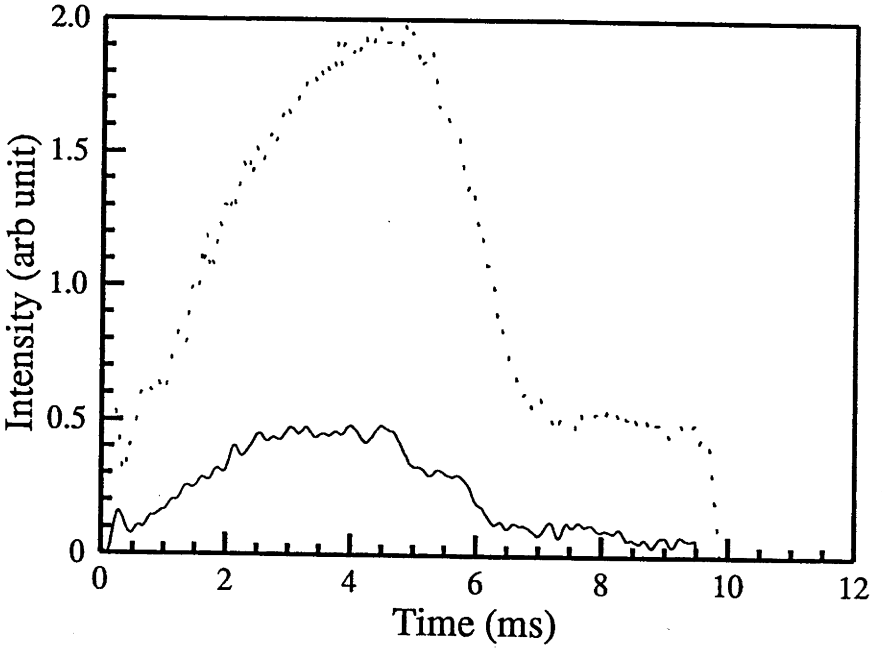

Figure 4.6: Evolution of spontaneous emission (dotted line) and optical gain (solid line) of the 488nm transition.

of preionization for the case of shorter pulse separation, so that the initial process will take less time. A low duty cycle of 10-20% ensures that the separation is long enough that the earlier pulsed plasma does not have much effect on the later one. The time evolution is then mainly dependent on the filling pressure and input power. Fig 4.8 shows t_1 and t_2 as a function of filling argon pressure, and Fig 4.9 shows the effect of varying the input rf power. It seems that the higher the pressure, the longer are t_1 and t_2, and the higher the input power, the shorter they are.These two characteristic times are not very sensitive to the magnetic field in the range of 0.06-0.11T, and then t_2 decreases following the increase of the B_0 field (Fig 4.10). Below 0.06T, the wave form does not have a'head', so that t_2 is zero. Notice that this sudden change of the evolution shape occurs at the same B_0 where a sudden change in the profile is observed (Fig 4.4). This also supports the suggestion of a mode change at B_0 ~0.06T. For the proposed application, the plasma should be operated with a pulse width equal to the sum

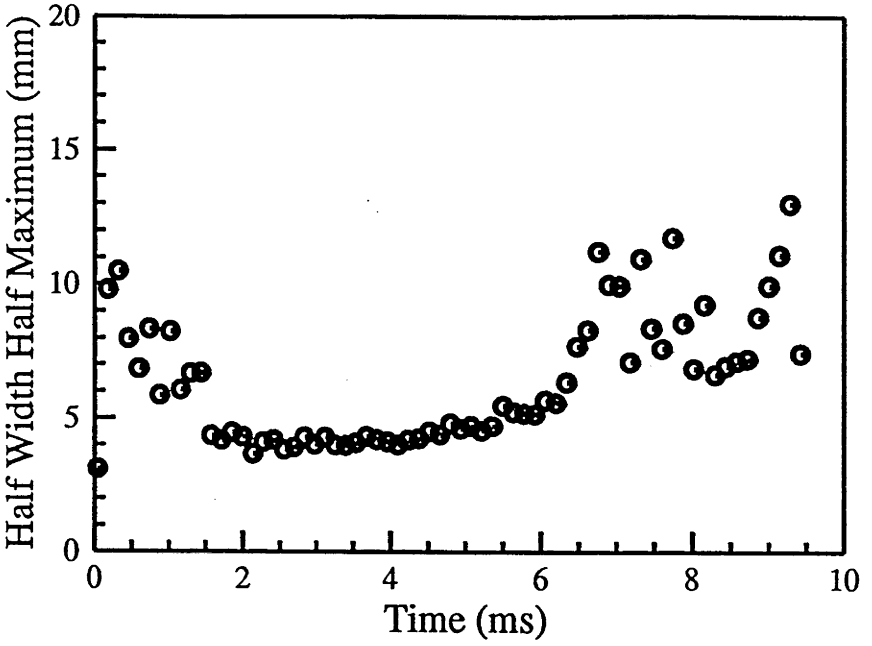

Figure 4.7: Evolution of the half-width half-maximum spontaneous emission profile.

of t_1 and t_2, and a high t_2/t_1 ratio is desirable.

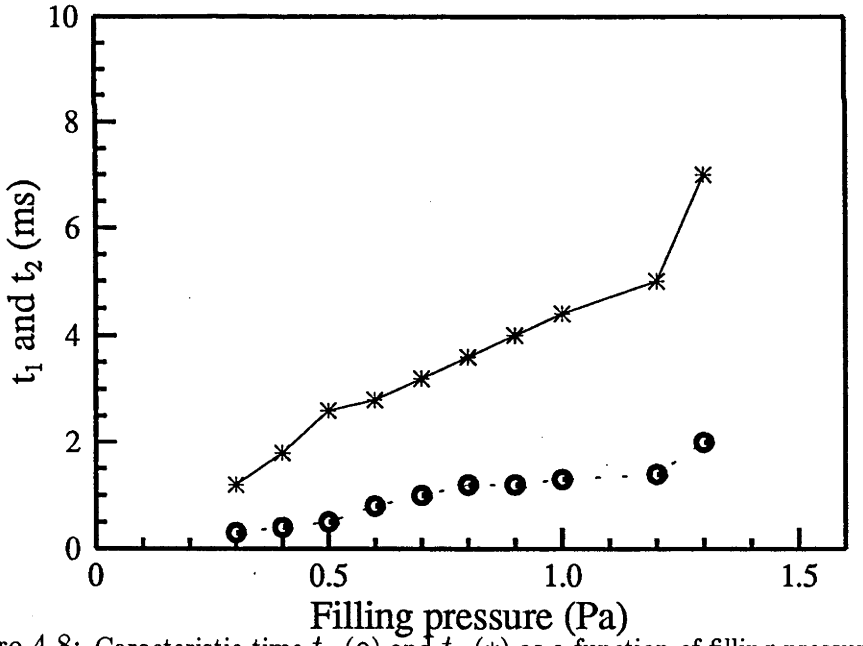

Figure 4.8: Caracteristic time t_1 (o) and t_2 (*) as a function of filling pressure.

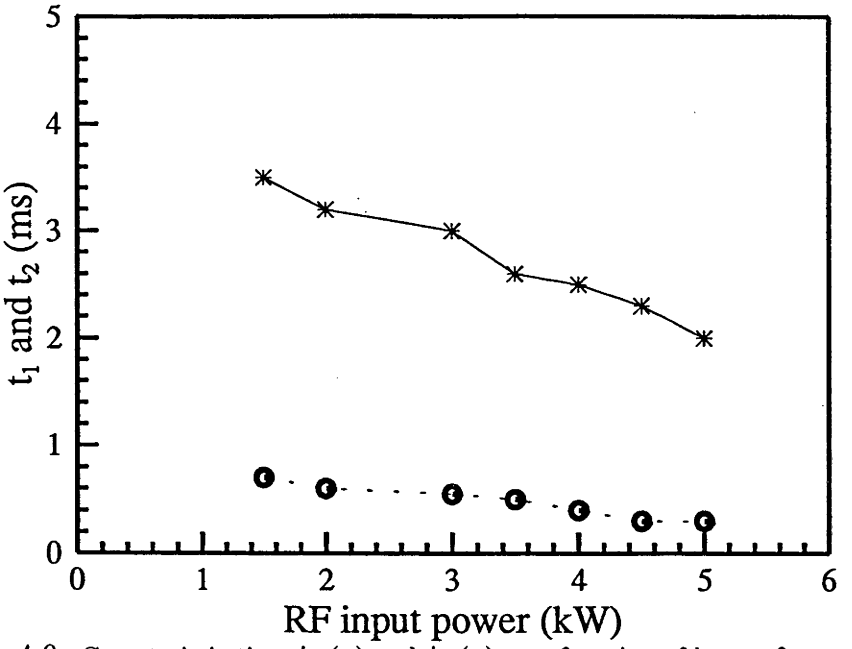

Figure 4.9: Caracteristic time t_1 (o) and t_2 (*) as a function of input rf power.

4.1.3 Emission and gain peaks

The peaks of the spontaneous emission and the gain during a pulse are of particularly interest, especially the latter, for exploring the optimal plasma operation

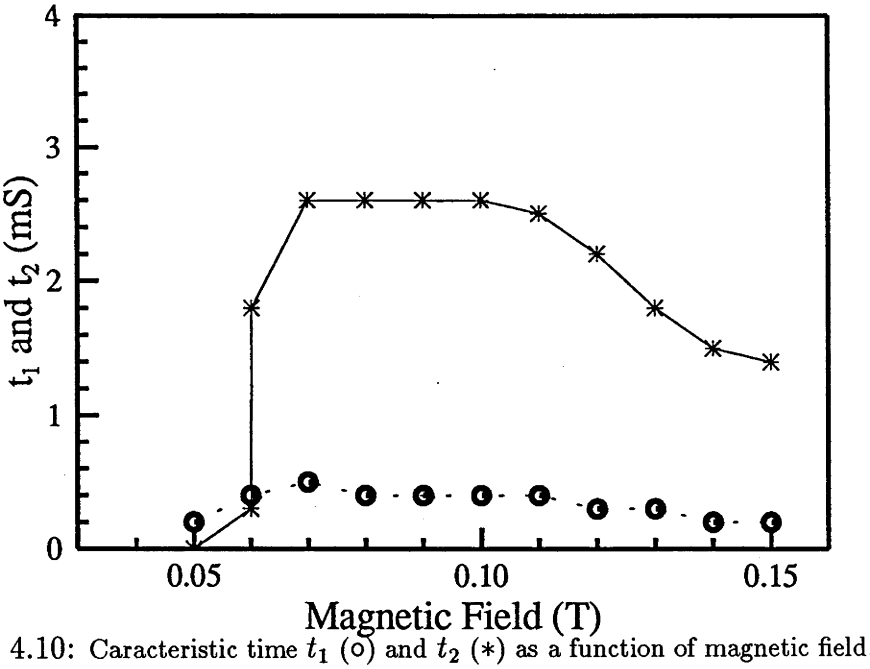

Figure 4.10: Caracteristic time t_1 (o) and t_2 (*) as a function of magnetic field.

condition for laser application, since the plasma has its best performance for lasing at these times. All the data are measured on the axis of the plasma and at a time when the gain or the emission reach their peaks. The following operation conditions: B_0=0.075T

P=0.9Pa

rf power of 3.5kW at 7MHz

tube diameter=45mm

will be regarded as standard and only one of the parameters will be varied to see its effect, unless otherwise stated. The peaks of the spontaneous emission and the optical gain as a function of magnetic field for excitation frequencies of 7, 10 and 14 MHz are plotted in Fig 4.11 and Fig 4.12 respectively. There is clearly a resonant range of B_0, for each excitation frequency where both the spontaneous emission and the optical gain of the 488nm line have their maximum. The optimal value of B_0 for maximum gain is close to that required by the condition $f_{rf} = f_{LH}$ (Fig 4.13) in the rf 7-14MHz range, where f_{rf} is the excitation frequency and f_{LH} is the lower hybrid frequency. This seems unlikely to be just a coincidence, although there is no convincing theory to explain this observation. The peak gain is not very sensitive to the excitation frequency (Fig 4.14), filling pressure (Fig 4.15), nor even the tube diameter (Fig 4.16), in the ranges of rf$\sim$7-14MHz, P$\sim$ 0.4-1.4Pa, and tube diameter of 30-65mm when optimal B_0 is used. When the rf power is increased from 1.5kW (the threshold for gain) to 3kW, the gain increases considerably at first, but afterwards it shows signs of saturating(Fig 4.17). The spontaneous emission of the line shows a similar variation but with a less well defined saturation. The largest peak gain achieved in the system is $\sim$7% when 5kW rf power is fed in.

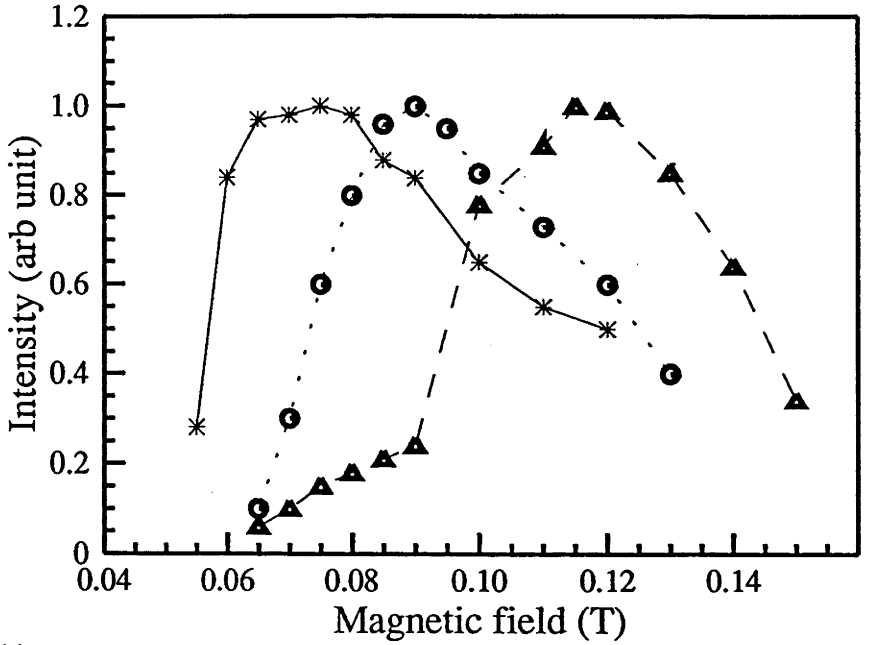

Figure 4.11: The 488nm spontaneous emission as a function of magnetic field for rf=7MHz (∗), rf=10MHz (o), and rf=14MHz (△).

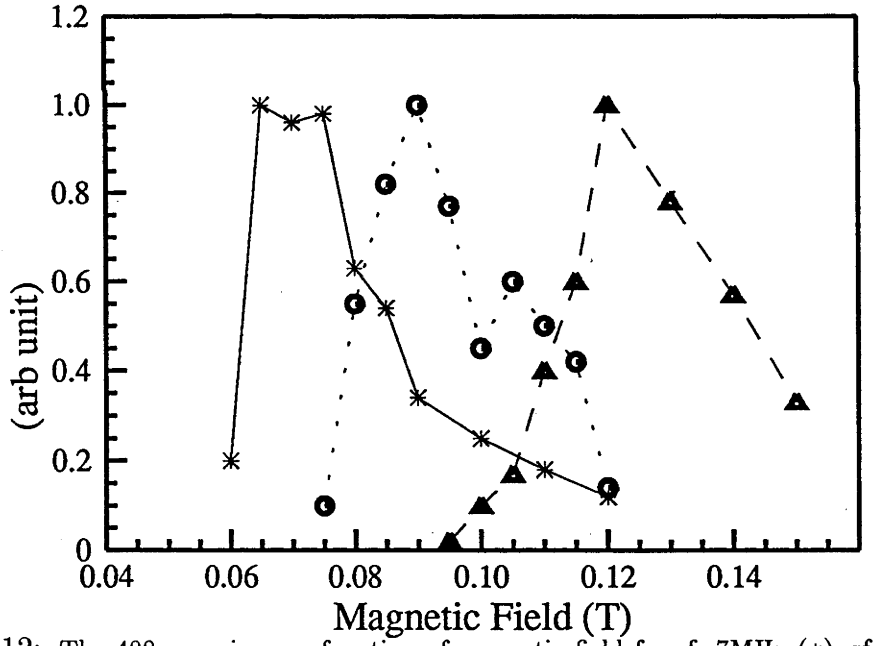

Figure 4.12: The 488nm gain as a function of magnetic field for rf=7MHz (∗), rf=10MHz (o), and rf=14MHz (△).

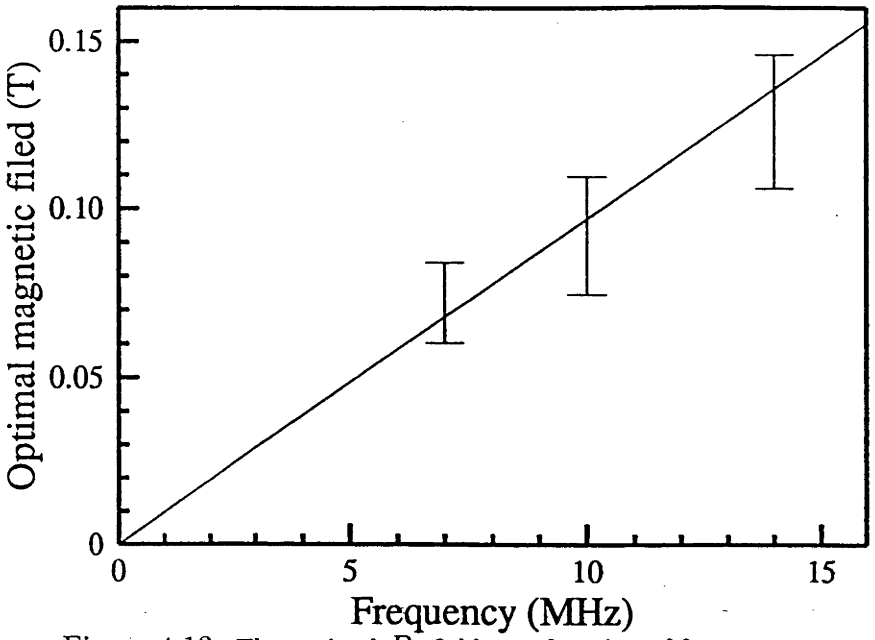

Figure 4.13: The optimal B_0 field as a function of frequency.

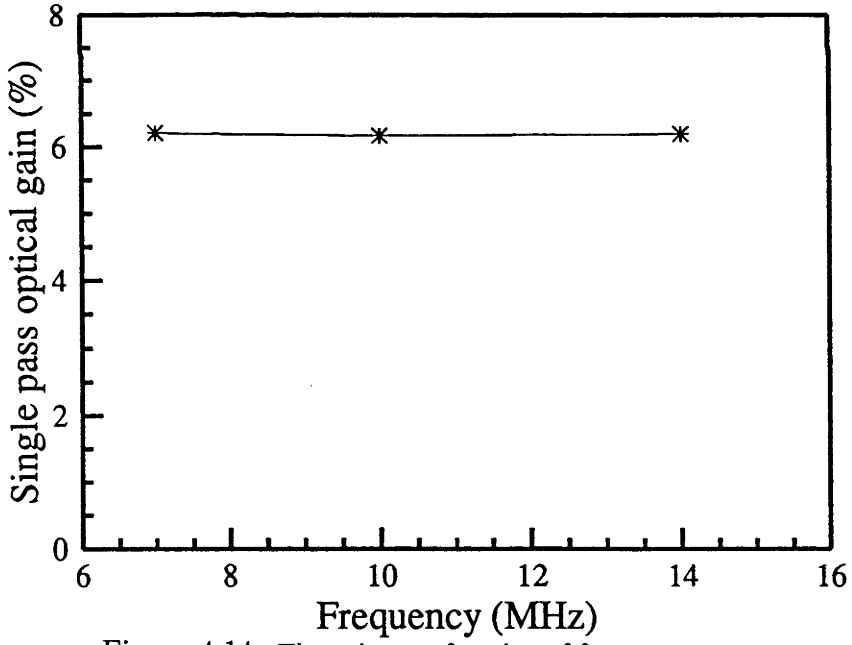

Figure 4.14: The gain as a function of frequency.

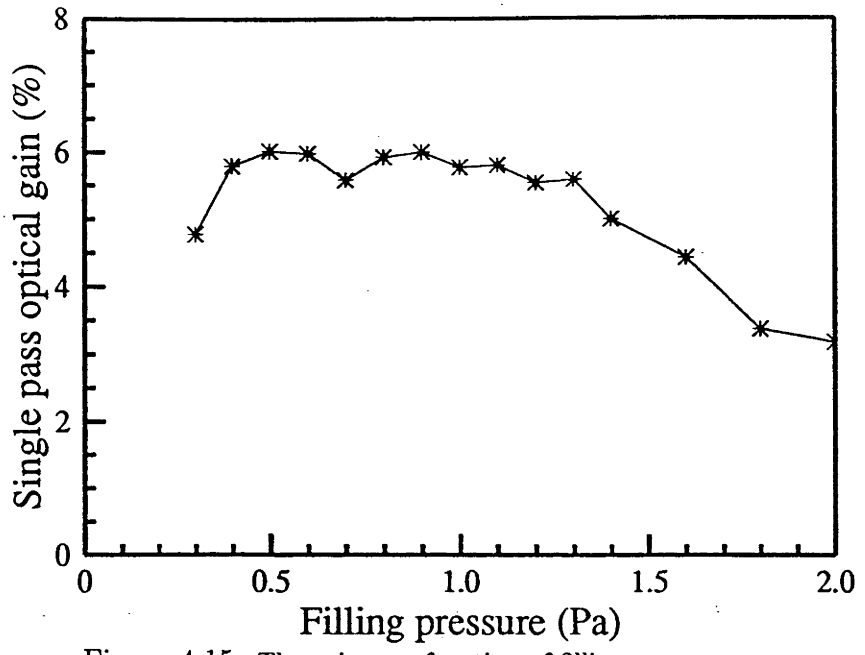

Figure 4.15: The gain as a function of filling pressure.

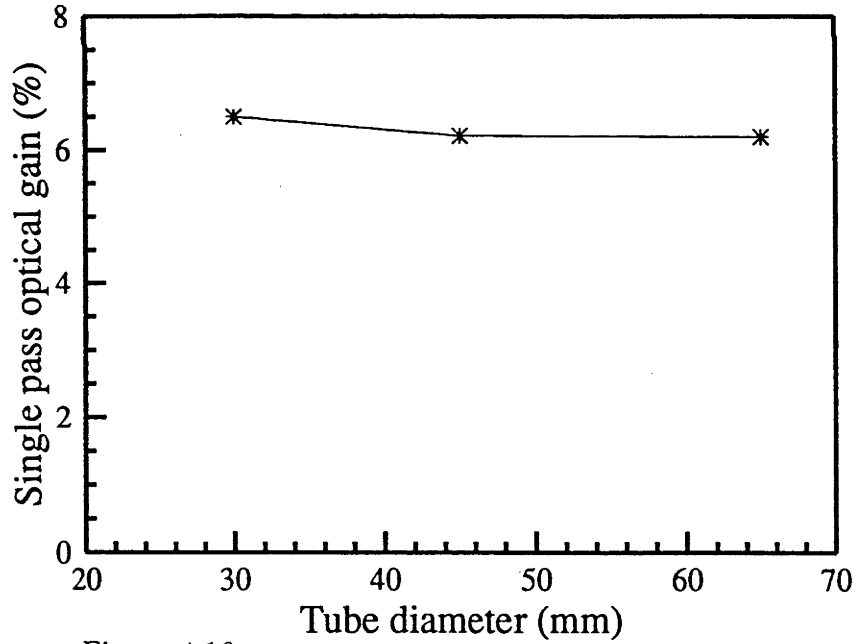

Figure 4.16: The gain as a function of tube diameter.

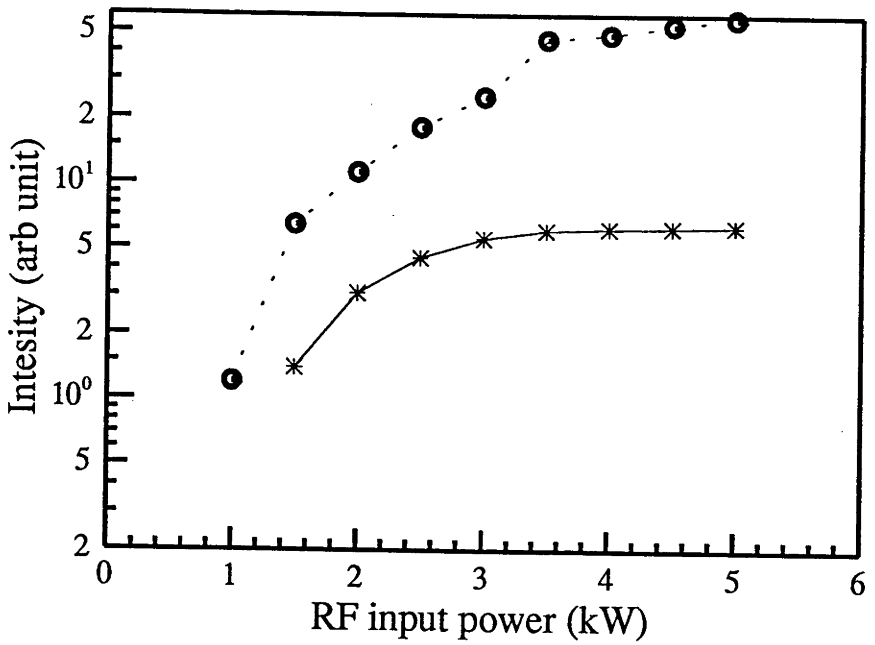

Figure 4.17: The spontaneous emission (o) and optical gain (*) as functions of rf input power.

4.2 Other lines

The peaks in the spontaneous emission of some other Ar^+ lines during a pulse have been measured to get a rough picture of the emission spectrum. The Ar^{++} 351nm emission under some operation conditions will be compared to the Ar^+ 488nm emission in this section,

The relative intensities of some Ar^+ transitions under the standard operation condition are listed in Table 4-1 together with their upper and lower states, excitation energies for these states, and their transition probabilities (A_{ki}).

The spectrum is shown in Fig 4.18. Fig 4.19 shows the Ar^{++} 351nm emission as a function of the rf input power. The 488nm emission is also plotted in Fig 4.19 for comparison. The results show the Ar^{++} emission increases quickly for rf

Wavelength (nm)	Upper state (k)	Lower state (i)	E_i (eV)	E_k (eV)	A_{ki} ($10^8 s^{-1}$)	Intensity (arb unit)
347.675	$(3P)4d^4D_{5/2}$	$(3P)4p^4P_{5/2}$	19.22	22.79	1.34	0.191
350.978	$(3P)4d^4D_{2/1}$	$(3P)4p^4P_{2/1}$	19.30	22.84	2.5	0.016
351.439	$(3P)4d^4D_{5/2}$	$(3P)4p^4P_{3/2}$	19.26	22.79	1.23	0.164
352.000	$(3P)4d^4F_{5/2}$	$(3P)4p^4D_{5/2}$	19.55	23.07	0.80	0.033
353.532	$(3P)4d^4D_{3/2}$	$(3P)4p^4P_{1/2}$	19.30	22.81	0.82	0.038
354.852	$(3P)4d^4F_{3/2}$	$(3P)4p^4D_{3/2}$	19.61	23.10	1.1	0.038
355.951	$(3P)4d^2F_{7/2}$	$(3P)4p^2D_{5/2}$	19.68	23.16	3.9	0.246
356.103	$(1D)4d'^2G_{9/2}$	$(1D)4p'^2F_{7/2}$	21.14	24.75	4.0	0.148
358.236	$(3P)4d^4F_{5/2}$	$(3P)4p^4D_{3/2}$	19.61	23.07	3.72	0.150
358.845	$(3P)4d^4F_{9/2}$	$(3P)4p^4D_{7/2}$	19.49	22.95	3.39	0.141
405.292	$(1S)4p''^2P_{3/2}$	$(1S)4s''^2S_{1/2}$	20.74	23.80	1.5	0.006
407.201	$(1D)4p'^2D_{5/2}$	$(1D)4s'^2D_{5/2}$	18.45	21.50	0.57	0.149
413.173	$(1D)4d'^2P_{1/2}$	$(1D)4s'^2D_{3/2}$	18.43	21.43	1.4	0.043
422.816	$(3P)4p^2D_{5/2}$	$(3P)4s^4P_{3/2}$	16.75	19.68	0.13	0.142
426.653	$(3P)4p^4D_{5/2}$	$(3P)4s^4P_{5/2}$	16.64	19.55	0.156	0.214
427.752	$(1D)4p'^2P_{3/2}$	$(1D)4s'^2D_{5/2}$	18.45	21.35	1.0	0.076
428.290	$(3P)4p^4D_{1/2}$	$(3P)4s^4P_{3/2}$	16.75	19.64	0.120	0.073
433.120	$(3P)4p^4D_{3/2}$	$(3P)4s^4P_{3/2}$	16.75	19.61	0.56	0.437
433.203	$(3P)4p^4P_{1/2}$	$(3P)3d^4D_{3/2}$	16.44	19.30	0.20	0.146
434.806	$(3P)4p^4D_{7/2}$	$(3P)4s^4P_{5/2}$	16.64	19.49	1.24	2.620
435.220	$(3P)4p^4P_{1/2}$	$(3P)3d^4D_{1/2}$	16.46	19.30	0.228	0.105
437.133	$(3P)4p^4P_{3/2}$	$(3P)3d^4D_{5/2}$	16.42	19.26	0.233	0.366
437.595	$(3P)4p^2S_{1/2}$	$(3P)4s^2P_{3/2}$	17.14	19.97	0.200	0.047
437.967	$(3P)4p^4D_{1/2}$	$(3P)4s^4P_{1/2}$	16.81	19.64	1.04	0.410
440.010	$(3P)4p^4P_{3/2}$	$(3P)3d^4D_{3/2}$	16.44	19.26	0.164	0.258
440.099	$(3P)4p^4P_{5/2}$	$(3P)3d^4D_{7/2}$	16.41	19.22	0.322	0.474
442.091	$(3P)4p^4P_{3/2}$	$(3P)3d^4D_{1/2}$	16.56	19.26	0.033	0.050

Table.4-1 Spontaneous emission of Ar^+ lines.

Wavelength (nm)	Upper state (k)	Lower state (i)	E_i (eV)	E_k (eV)	A_{ki} ($10^8 s^{-1}$)	Intensity (arb unit)
442.601	$(3P)4p^4D_{5/2}$	$(3P)4s^4P_{3/2}$	16.77	19.55	0.83	1.171
443.019	$(3P)4p^4D_{3/2}$	$(3P)4s^4P_{1/2}$	16.81	19.61	0.53	0.527
448.181	$(1D)4p'^2D_{5/2}$	$(3P)3d^2D_{5/2}$	18.73	21.50	0.494	0.114
454.505	$(3P)4p^2P_{3/2}$	$(3P)4s^2P_{3/2}$	17.14	19.87	0.413	0.184
457.935	$(3P)4p^2S_{1/2}$	$(3P)4s^2P_{1/2}$	17.27	19.97	0.82	0.186
458.990	$(1D)4p'^2F_{5/2}$	$(1D)4s'^2D_{3/2}$	18.43	21.13	0.82	0.264
460.956	$(1D)4p'^2F_{7/2}$	$(1D)4s'^2D_{5/2}$	18.45	21.14	0.91	0.528
465.789	$(3P)4p^2P_{1/2}$	$(3P)4s^2P_{3/2}$	17.14	19.80	0.81	0.222
472.686	$(3P)4p^2D_{3/2}$	$(3P)4s^2P_{3/2}$	17.14	19.76	0.50	0.227
473.591	$(3P)4p^4P_{3/2}$	$(3P)4s^4P_{5/2}$	16.64	19.26	0.58	0.811
476.486	$(3P)4p^2P_{3/2}$	$(3P)4s^2P_{1/2}$	17.26	19.87	0.575	0.227
480.602	$(3P)4p^4P_{5/2}$	$(3P)4s^2P_{3/2}$	16.64	19.22	0.79	1.752
484.782	$(3P)4p^4P_{1/2}$	$(3P)4s^4P_{3/2}$	16.75	19.30	0.85	0.467
486.592	$(3P)5s^4P_{5/2}$	$(3P)4p^4S_{3/2}$	19.97	22.51	0.15	0.017
487.986	$(3P)4p^2D_{5/2}$	$(3P)4s^2P_{3/2}$	17.14	19.68	0.78	1.000
488.903	$(3P)4p^2P_{1/2}$	$(3P)4s^2P_{1/2}$	17.27	19.68	0.159	0.044
493.321	$(3P)4p^4P_{3/2}$	$(3P)4s^4P_{3/2}$	16.75	19.26	0.143	0.205
496.507	$(3P)4p^2D_{3/2}$	$(3P)4s^2P_{1/2}$	17.27	19.76	0.347	0.120
497.216	$(3P)4p^4P_{1/2}$	$(3P)4s^4P_{1/2}$	16.81	19.30	0.096	0.045
500.933	$(3P)4p^4P_{5/2}$	$(3P)4s^4P_{3/2}$	16.75	19,22	0.147	0.433
506.204	$(3P)4p^4P_{3/2}$	$(3P)4s^4P_{1/2}$	16.81	19.26	0.221	0.339
514.179	$(3P)4p'^2F_{7/2}$	$(3P)3d^2D_{5/2}$	18.73	21.14	0.095	0.096
514.532	$(3P)4p^4D_{5/2}$	$(3P)4s^2P_{3/2}$	17.14	19.54	0.097	0.221
624.313	$(3P)4p^2D_{5/2}$	$(3P)3d^4F_{7/2}$	17.69	19.68	0.029	0.032
648.308	$(3P)4p^2S_{1/2}$	$(3P)3d^2P_{3/2}$	18.06	19.97	0.101	0.014

Table.4-1 Spontaneous emission of Ar^+ lines(continued)

powers above 3.5kW suggesting a significant increase in double ionization above 3.5kW. This could be an explanation of the saturation of both the spontaneous emission and the optical gain of the Ar^+ 488nm line. The Ar^{++} 351nm emission

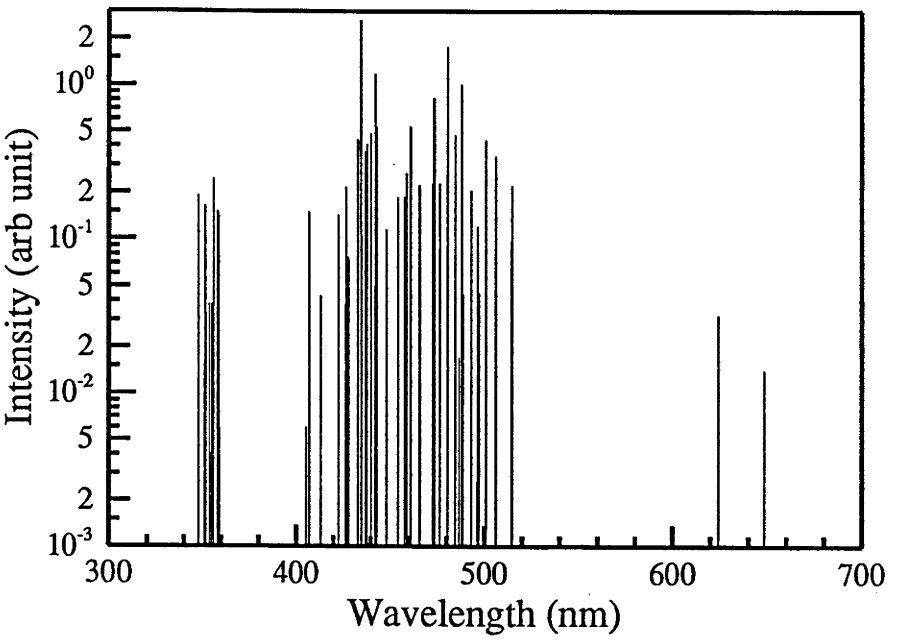

Figure 4.18: Ar^+ spectrum in Basil-II.

as function of the magnetic field is shown in Fig 4.20, with the resonant B_0 range centred around 0.095T instead of 0.075T for the Ar^+ 488nm emission. A possible explanation of this result will be discussed in chapter 7.

4.3 Discussion and some conclusions

Since the experimental results show that a gain of ~7% can be obtained, it can be concluded that this plasma can surely be used in a new type of argon ion laser. In this section the results will be discussed to predict the optimal operating conditions for obtaining the best performance of a laser based on this plasma.

From the experimental results, it is clear that the optical behaviour of the

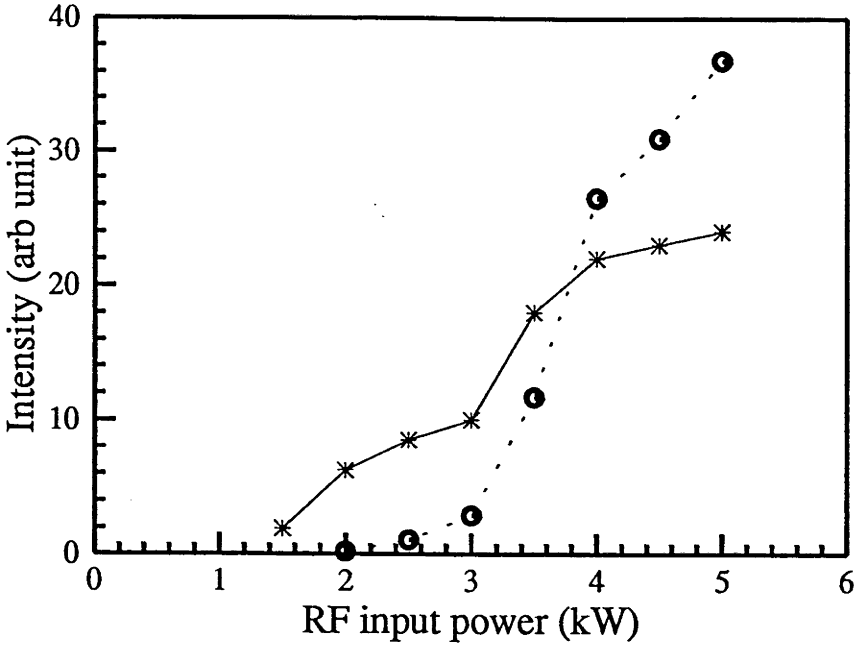

Figure 4.19: The Ar^{++} 351nm emission (o) and the Ar^{+} 488nm emission (*) as a function of rf input power.

plasma is sensitive to the longitudinal magnetic field and that there is a resonant magnetic field range. This B_0 range is nearly independent of the tube diameter, the argon filling pressure, and the rf input power, but is approximately propor-

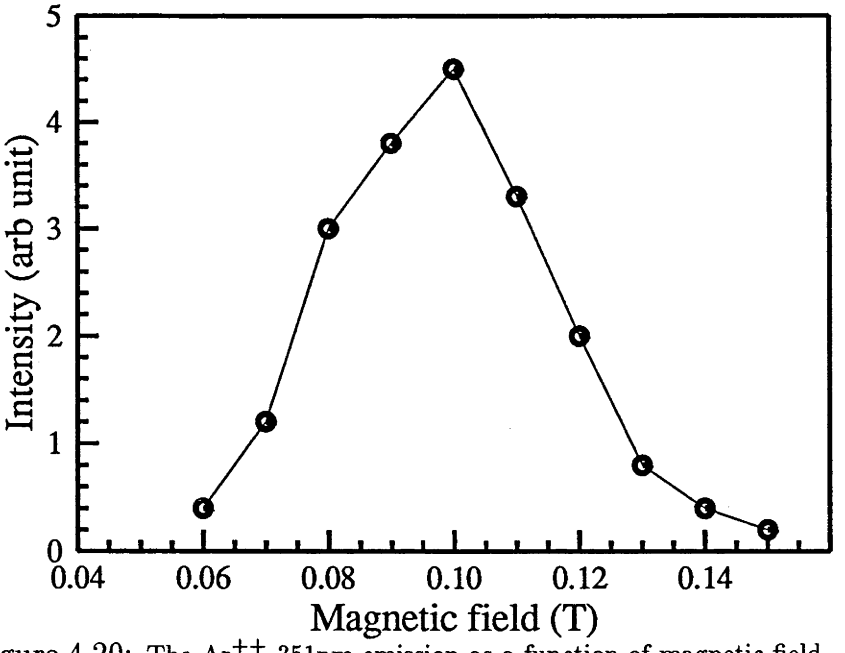

Figure 4.20: The Ar^{++} 351nm emission as a function of magnetic field.

tional to the excitation frequency. When this resonant magnetic field is applied, the rf input power seems to be coupled into the plasma mainly near the axis so forming a highly peaked emission profile, and both the emission and the gain of the 488nm line reach their maximum suggesting a higher coupling efficiency. Thus the plasma should be operated within this resonant magnetic field range in order to get the best performance in a laser application.

The main effect of the filling pressure is on the time evolution: one can increase the effective running time t_2 by increasing the filling pressure. However, for filling pressure higher than 1Pa, the gain slowly decreases with pressure and then drops significantly above 1.4Pa for the range of rf power available. Thus, the filling pressure should be within the range of 0.3-1.3Pa for the best performance of the plasma as a laser source, and the optimal filling pressure will depend mainly on the required laser output pulse duration within the range. To get the highest possible efficiency, the shorter the pulse duration is required, the lower the filling pressure should be used. The shortest plasma duration is limited by the shortest t_1, which is $\sim$0.2ms, when a pressure $\sim$ 0.3Pa is used (Fig 4.8) and one expect a pulse duration of 1ms to obtain the best performance. The optimal filling pressure for getting high efficiency can be expected to be within the range of 0.5 - 1Pa, since in this pressure range the peak gain reaches its maximum.

A threshold power P_{th} $\sim$1.5kW is required to obtain the gain. This power is equivalent to a mean current density of 8A/cm^2 in a similar size (R=5mm, L=1m) dc-excited Ar^+ laser which has a nearly constant voltage drop $\sim$200V for a large current range[32]. Compared to the threshold current density $j_{th} \sim 400/L^{1/2}$=40-50Acm^{-2}[32][33] for a dc-excited Ar^+ laser, this is a lower starting current point. On the other hand, when the rf input power exceeds 3.5kW,

the trace of gain saturation is obvious, meanwhile an increase in Ar^{++} emission is observed. This suggests a saturation in the laser output since as mentioned above the maximum possible output intensity $I_{max} \sim G\, I_{sat}$. And $I_{sat} = G\frac{h\omega}{\sigma\tau_{eff}}$ is normally independent of the input power which changes the pumping rate[29]. The results from the dc-excited Ar^+ laser showed[34] that the laser output does not saturate until a very high current density $\sim$300A/cm^2 is reached. For a dc-excited Ar^+ laser with similar active medium size, 3.5kW corresponds to a current density of only $\sim$22A/cm^2. Notice that this is one order lower than that for dc-excited Ar^+ laser and is only half the value of the threshold current density for a dc Ar^+ laser. This extremely low power for the gain saturation (P_{sat}) is unexpected. This behaviour could suggest that the excitation mechanism responsible for the population inversion is different from that in a dc-excited Ar^+ laser. The fact of a rather early gain saturation above 3.5kW suggests the laser should be operated at a power level not much higher than 3.5kW for the 488nm transition. This also probably means a much lower threshold power for making an ultraviolet Ar^{++} laser, since there is evidence that the saturation in the 488nm gain and emission is the result of the increased double ionization rate.

It is concluded that a new Ar^+ laser can be made based on this plasma and that the laser beam will have a diameter $\sim$1.2cm. Internal laser mirrors can be used to minimize the loss of the system since there are no electrodes and the plasma-wall interaction is weak enough to avoid the associated impurities, which is the main cause of mirror damage. The laser can be operated under the experimental condition range of:

B_0: 0.065-0.1T at 7MHz;

B_0: 0.011-0.16T at 14MHz;

P: 0.4-1.2Pa for repetitive running mode with pulse duration 1-10ms;

RF power: 3.5 and up;

Tube diameter: 30-100mm.

Chapter 5

A new Ar^+ laser based on Basil-II plasma

This chapter describes a novel Ar^+ laser based on the Basil-II plasma. Some comparisons with the conventional Ar^+ laser will also be included in this chapter.

There are at least two points which make this laser different from all of the previous argon ion lasers. First, this is the only laser so far which has a discharge tube diameter of 45mm, much bigger than that of the previous largest argon ion laser system ($\leq$16mm), while the laser output beam diameter is only a quarter of the tube size. The fact that the laser active medium is isolated from the tube wall by a relatively lower density plasma means less plasma-wall interaction, hence less problems with tube wall cooling and less impurities from the wall to pollute the laser system. Second, this system is based on a very efficient plasma generated by the helicon waves, which is excited by a short (80mm) external double loop rf antenna, hence all the technical problems associated with the electrodes can be completely avoided. Both these points are obvious advantages over other types

of argon ion lasers.

Section 1 of this chapter describes briefly the construction of the laser. The output behaviour for various operating conditions will be presented in section 2. Section 3 is a summary.

5.1 Construction of the laser

The laser is developed from the Basil-II apparatus, the main difference being the addition of a pair of internally mounted laser mirrors to form the optical cavity. The main point of the design is to minimize possible mirror damage.

As mentioned above, one of the main advantages of a rf plasma as a laser source is that it avoids all the problems associated with electrodes. It has also been found that the effect of the plasma-wall interaction in this plasma is much less important than that in a dc-excited Ar^+ laser[35] so that the production of impurities from the tube wall, which might be deposited on the mirror surface to degrade the mirror quality, is minimized. Therefore, the ion bombardment on the mirror surface could be a main source for the possible mirror pollution. The net electrical current along the axis should be zero since there are no electrodes to form a current circuit in this plasma. The diffusion of ions is then the main process for them to reach the mirror surface. A pair of stainless steel baffles is used to reduce the flux of ions to the mirrors. These baffles have a 15mm diameter hole in the centre which enables the light in the active medium to travel freely along the axis. There are also two stainless steel tubes on the mirror mount which absorb the ions which escape through the holes of the baffles. It is possible to bias these

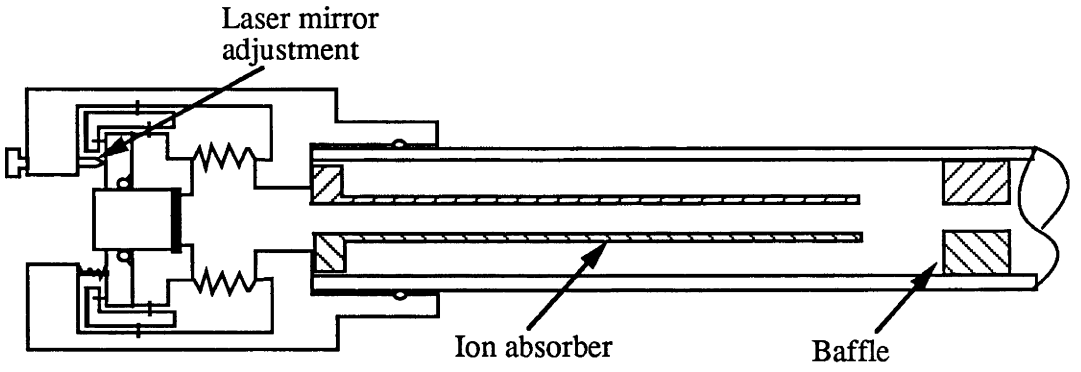

Figure 5.1: Construction of the laser cavity.

ion absorbers to obtain better ion collection performance. The mirrors are then directly fitted on the end of the plasma without the need of introducing Brewster angle windows to separate the mirrors from the plasma. The construction of one end of the laser cavity is shown in Fig 5.1. Two sets of mirrors are investigated in this study, referred to as mirror set 1 and mirror set 2. Mirror set 1 consists of one 100% (R>99.8%) reflecting mirror and one 2% transparency output coupler to study the laser output behaviour of the 488nm transition. Mirror set 2 consists of two 100% (R>99.8%) reflecting laser mirrors to observe the laser action of other transitions. These two sets mirrors were used because they were of available. The mirrors are so adjusted as to get the maximum power output regardless of the mode structure. Table 5-1 lists the specifications of these mirrors.

		ϕ (mm)	T (%)	R (mm)	wavelength range
Set 1	mirror a	15	<0.2	400	457-514nm
Set 1	mirror b	15	2	600	488-514nm
Set 2	mirror a	15	<0.2	400	457-514nm
Set 1	mirror b	15	<0.2	∞	457-514nm

Table 5-1. The specifications of the mirror set 1 and mirror set 2.

Data supplied by Spectra-Physics PTY. LTD.

5.2 Output properties of the laser

The laser is operated in multi- longitudinal modes with the output at 8 transitions in the blue to green region. The output of one of the main laser operation transitions, the 488nm line, has been measured for various experimental conditions to find the optimal operating conditions for this laser. The experiments are carried out under the operation conditions within the range:

$0.050 \leq B_0 \leq 0.14$T;

$0.4 \leq$ P≤ 1.5Pa;

$1 \leq P_{rf} \leq 5$kW;

$f = 7$MHz;

Tube diameter = 45mm;

Pulse : duration 1-10ms, duty cycle 5-50%.

The output of the other lines is measured only as a function of the rf input power at fixed filling pressure of 0.9Pa and fixed magnetic field of 0.075T.

The laser output beam has a waist width ~10mm with a divergent angle $\sim 5 \times 10^{-3}$radians. The diameter of the laser output beam is ~1cm, only about a quarter of the tube size. The output has high order transverse modes so that the cross section of the output has quite complicated patterns.

The experimental results of the laser output of the 488nm transition and the other transitions will be discussed in the following subsections.

5.2.1 The laser output of the 488nm transition

Mirror set 1 is used to study the laser output behaviour of the 488nm transition. Since there are no windows between the laser medium and the laser mirrors, the total loss of the system is approximately equal to that of the mirrors. This is ~2% for mirror set 1. Hence in this case the small signal gain of any transition must exceed 2% per pass to satisfy the laser oscillation condition. It turns out that the 488.0nm transition meets the requirement but the 514.5nm transition does not. Hence the majority of the laser output in the system using mirror set 1 belongs to the 488nm transition.

The laser output of the 488.0nm transition as a function of the magnetic field (Fig 5.2), for rf power of 3.5kW and P=0.9Pa, is similar to the curve for

optical gain (Fig 4.12) as would be expected. There are also, however, some differences. The peak of the laser output is shifted slightly to higher fields and the laser output curve is broader than the gain curve. This may be due to the fact that the gain measured is only at the centre frequency of the 488nm line, while the laser operates with complex high order transverse modes. The threshold magnetic

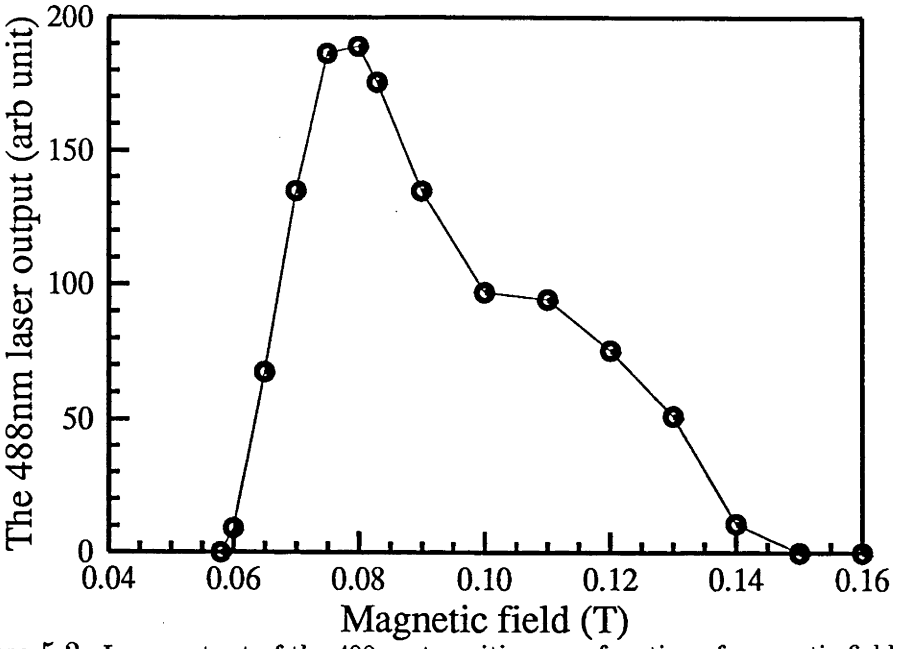

Figure 5.2: Laser output of the 488nm transition as a function of magnetic field.

field is slightly higher than that for the gain since a gain exceeding 2% is required to obtain any laser output in this system. Fig 5.3 shows the optimal magnetic field as function of input rf power (f_{rf}=7MHz) for various filling pressure. The optimal magnetic field is not sensitive to either input power or filling pressure, and has a value of 0.075T for rf power exceeding 2.5kW. A slightly larger B_0=0.095T is required for rf power input lower than 2 kW. This suggests that there is a resonant mechanism responsible for the population inversion in this system.

As a function of the argon filling pressure, the output changes very little from its peak over quite a wide range (Fig 5.4), hence providing a reasonable pressure range for practical operation. However, in a repetitive running mode, for a given pulse duration, there is a requirement of a minimum separation time to obtain good output performance. If the separation time is shorter than this minimum time, the mode in which the plasma operates changes unpredictably from the high mode to low mode, and the laser output will disappear in some

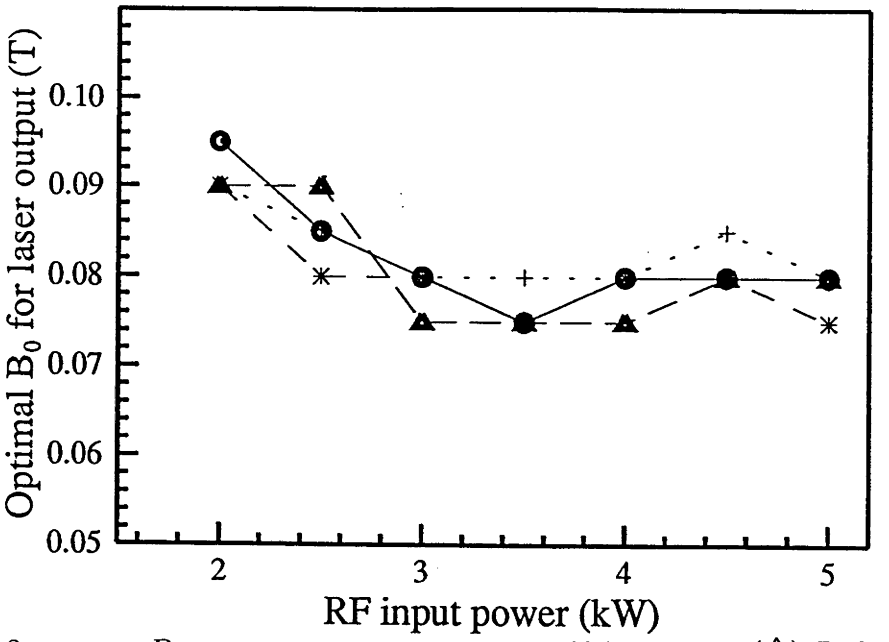

Figure 5.3: Optimal B_0 field as a function of magnetic field for P=0.5Pa (△), P=0.7Pa (+), P=0.9Pa (o), and P=1.1Pa (∗).

of the pulses. Fig 5.5 shows the required minimum pulse separation time (t_{sep}) as a function of filling pressure for pulse duration of 5ms, B_0=0.8T and rf power of 3kW at 7MHz. It can be concluded from Fig 5.5 that the higher the filling

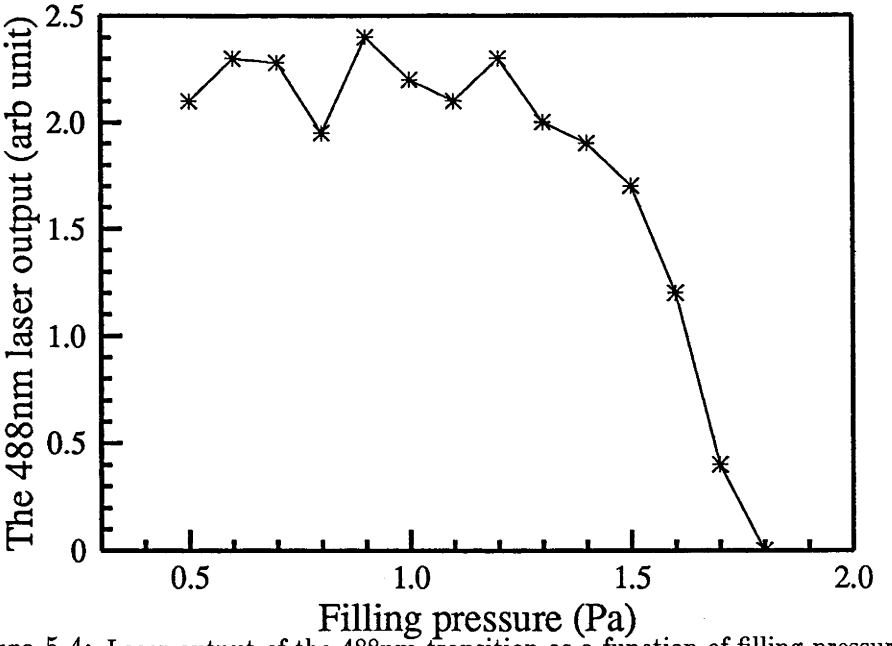

Figure 5.4: Laser output of the 488nm transition as a function of filling pressure.

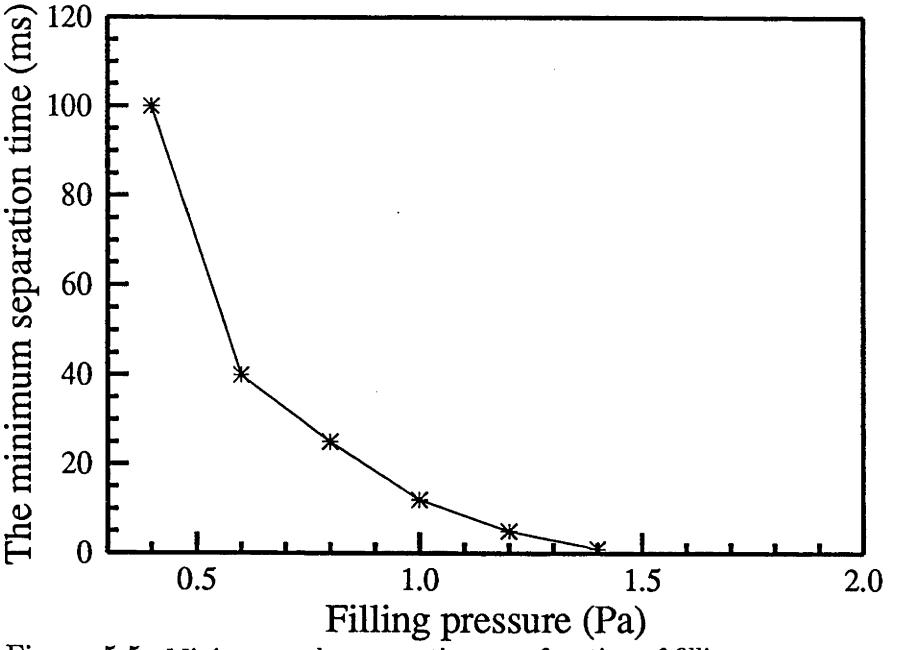

Figure 5.5: Minimum pulse separation as a function of filling pressure.

pressure, the larger the duty cycle could be. This implies that cw (duty cycle of 100%) operation could be reached when the filling pressure is high enough. When rf power increases, the output increases rapidly up to 3.5kW but has the trace of saturation afterwards (Fig 5.6). The highest efficiency, however, is at the highest rf input power in the range (Fig 5.7), when the highest laser output (0.5W) for the 488nm transition is reached with a pulse duration of 5ms with 10% duty cycle.

It can thus be concluded that the optimal operating conditions for the best performance of this laser at a repetitive long pulse operation mode are B_0: 0.065-0.100T, P: 0.5-1.2Pa, and the input rf power should exceed 5kW.

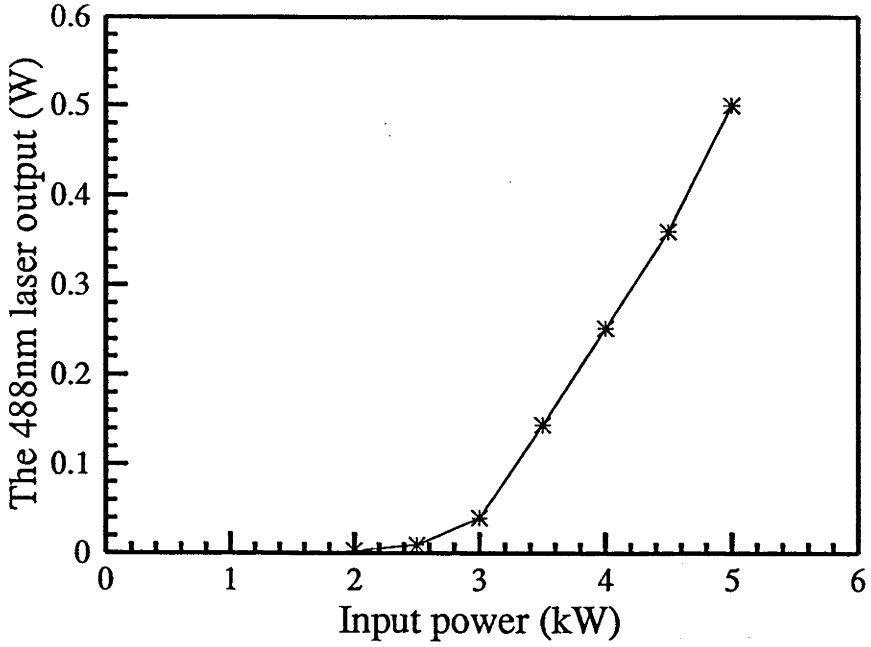

Figure 5.6: Laser output of the 488nm transition as a function of rf input power.

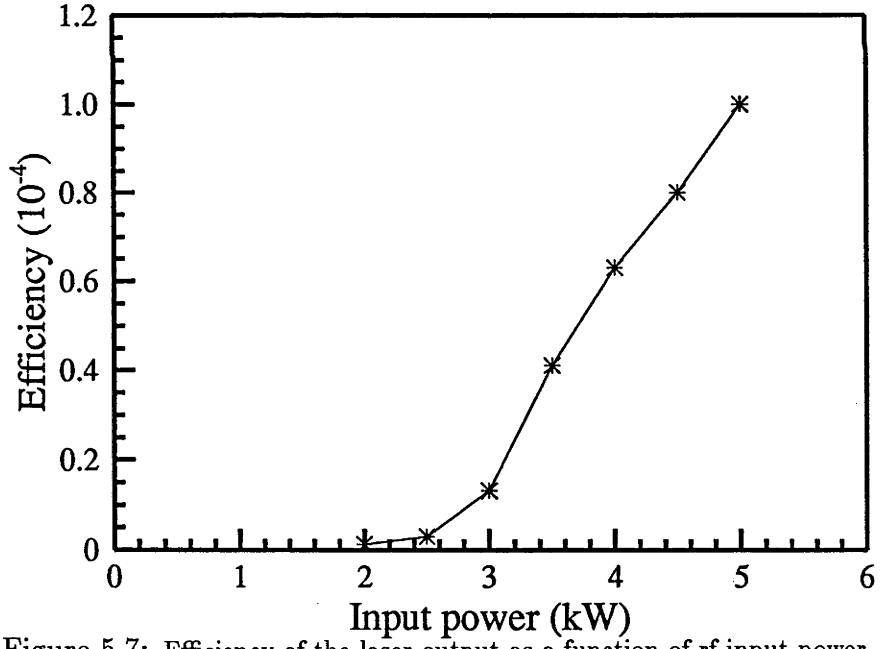

Figure 5.7: Efficiency of the laser output as a function of rf input power.

5.2.2 Laser output with mirror set 2

The mirror set 2 is used to study the laser output of all the transitions within the green-blue range since the total mirror loss of this set is less than 0.4% and a very low gain threshold of only 0.4% is required to observe any laser oscillation.

Laser action at 8 transitions has been found, among them the 514.53nm being the strongest although the 488nm transition has the lowest threshold (Fig 5.8). The experiments are carried out at B_0=0.075T, filling pressure 0.9Pa, and various rf input power at 7MHz. Seven transitions from the eight belong to the 4P-4S transitions while the other (514.18nm) belongs to the $(1D)4p'^2F_{7/2} - (3p)3d^2D_{5/2}$ transition. All these 8 transitions are among the typical laser operation transitions for the conventional argon ion laser. Table.5-2 lists the upper and lower levels of these 8 transitions together with their excitation energy in eV.

Continuous laser operation has also been obtained by using this mirror set but the rf input power used is restricted to below ~1.5kW to avoid the risk of overheating the system. All plasma properties, such as the radial profile, emission intensity, appear to remain roughly the same as those observed in the long pulse operation mode during its quasistationary period. However, a higher filling pressure is needed in dc operation mode to keep the plasma steady. Only the 488nm transition is found since the other transitions need higher threshold power. The behaviour of the continuous running laser is very similar to the pulsed one except that a higher pressure of 1.4-1.6Pa is required for continuous operation at ~1kW level.

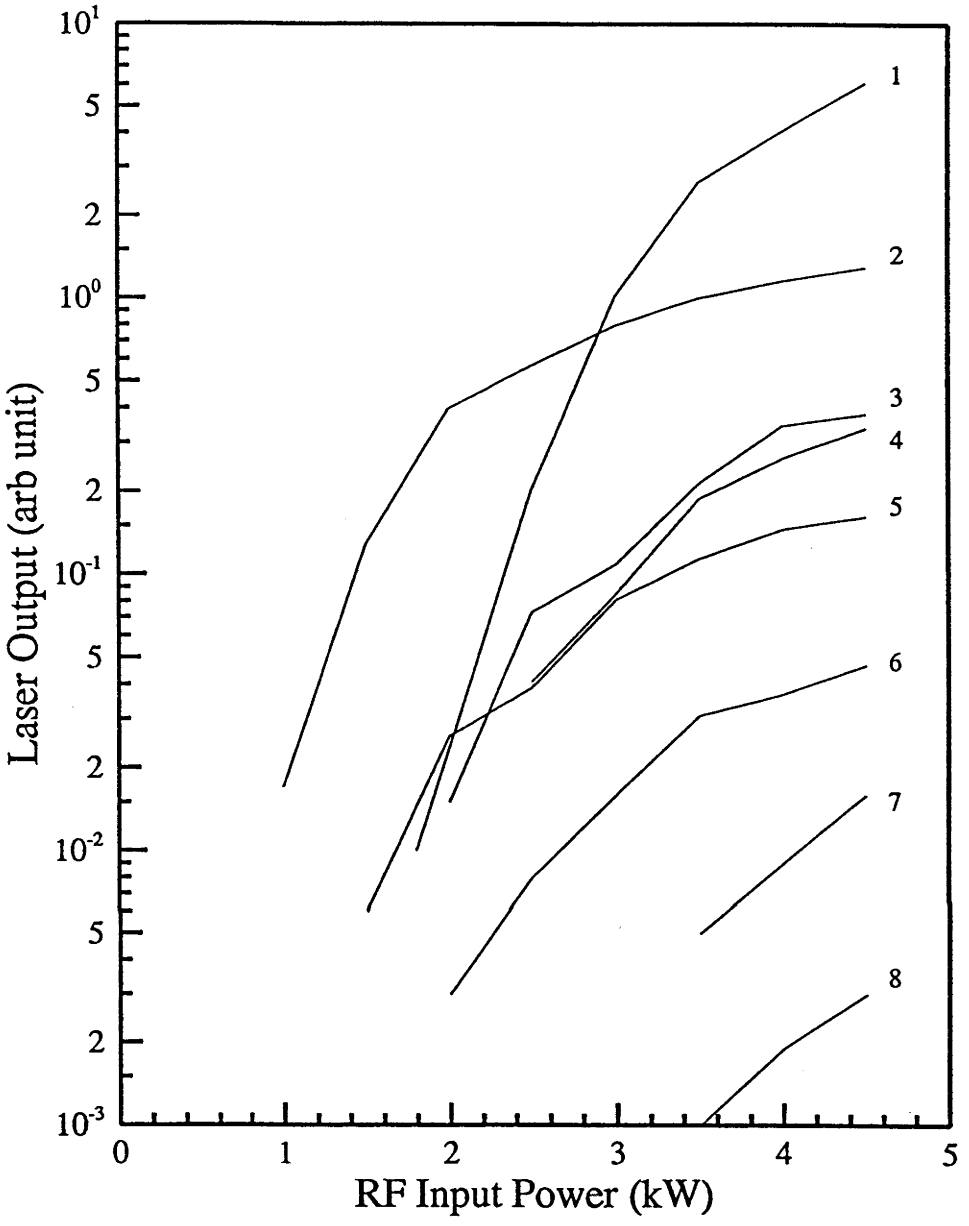

Figure 5.8: Laser output of (1) the 514.2nm transition, (2) the 465.8nm transition, (3) the 457.92nm transition, (4) the 476.5nm transition, (5) the 501.7nm transition, (6) the 496.5nm transition, (7) the 488.0nm transition, (8) the 514.5nm transition, as a function of rf input power.

Wavelength of the transtion	Lower level	Upper level	Excitation energy
457.9nm	$4s^2P_{1/2}$	$4p^2S_{1/2}$	19.97eV
465.8nm	$4p^2P_{1/2}$	$4p^2S_{3/2}$	19.80eV
476.5nm	$4p^2P_{3/2}$	$4p^2S_{1/2}$	19.87eV
488.0nm	$4p^2D_{5/2}$	$4p^2S_{3/2}$	19.68eV
496.5nm	$4p^2D_{3/2}$	$4p^2S_{1/2}$	19.76eV
501.7nm	$4p^4D_{3/2}$	$4p^2S_{3/2}$	19.80eV
514.2nm	$4p'^2F_{7/2}$	$3d^2D_{5/2}$	21.14eV
514.5nm	$4p^4D_{5/2}$	$4p^2S_{3/2}$	19.54eV

Table 5-2 Upper and lower levels and excitation energy of the 8 lasing transitions observed in Basil laser

5.3 Summary and discussion

A new argon ion laser based on an electrodeless plasma has been developed. The laser output is sensitive to the axial magnetic field and the optimal field is ~0.075-0.100T. The laser can be operated in the pressure range of 0.5-2Pa, but the optimal range for pulsed operation is 0.5-1.2Pa. The threshold rf power is about 1kW for the system using a set of high reflection mirrors (mirror set 2) and 2.5kW for the system using a 2% laser coupler. Eight wavelengths within the green-blue range have been observed. The strongest two transitions among the eight are at 514.53nm and 487.98nm, and the intensity of the former is about 4 times of that of the latter in a system using mirror set 2 for input rf power of 5kW,

B_0 of 0.75T, and filling pressure of 0.9Pa. The highest laser output at 488nm this system has reached is 500mW with an efficiency $\sim 10^{-4}$ when mirror set 1 is used. Further increase of both output power and the efficiency is possible if the input power is increased. Continuous operation of this laser has been shown to be possible but the optimal condition, especially the filling pressure, could differ from that found in this study.

This laser has some unique characteristics which have not been observed in any other existing argon ion lasers. Table 5-3 compares some of the features of the dc Ar^+ lasers and this laser.

	Discharge type	Active medium diameter	Threshold current density	Saturation current density	W_{in}/l (kW/cm)	Efficiency (10^{-4})
dc laser	small tube(1-10mm) high current density discharge	1-10mm	~50A/cm^2	>350A/cm^2	0.8 for best performance	1-10
Basil-II laser	large (30-60mm) tube discharge generated by an m=1 helicon wave	~10mm	~6A/cm^2	~30A/cm^2	0.05	1

Table 5-3 Comparison of Basil-II laser with dc excited Ar^+ laser

From Table 5-3, one can see this new laser required much lower threshold 'current density' (effective current density) compared to a dc-excited Ar^+ laser. The fact that the power input per unit plasma length of this laser is more than one order lower than that for best performance of a dc Ar^+ laser suggests the highest input rf power used in this study, which is limited by the rf supply, is far from the power required for the best performance. On the other hand, the efficiency of this laser is about the same as that for a commercial Ar^+ laser. Since the efficency of a Ar^+ laser normally increases rapidly with input power, it is predicted that much

higher efficiency can be reached for an Ar^+ laser based on this plasma by simply increasing the input power.

Chapter 6

Plasma parameters

The preceding two chapters imply that the mechanism responsible for the laser action in Basil-II could be quite different from that in conventional dc argon ion lasers. It is necessary then to look into the plasma for a possible explanation. This chapter presents the experimental investigation of the plasma parameters such as electron density, electron energy distribution function, and the phase velocity of the m=1 helicon wave.

Section 1 of this chapter describes the experimental results of the electron density. Electron density is estimated by a radially moveable single Langmuir probe and its absolute value is checked by microwave interferometry. Electron energy distribution functions will be discussed in Section 2 of this chapter. An unusual beam-like nonthermal tail which can last for ~1ms has been observed. Although the beam-like electron tail has been experimentally measured in some plasmas with electron beam injection[36]-[39], this is the first time such a northermal tail is observed in a laborotary plasma without beam injection. In Section 3 the results of the helicon wave phase velocity measurements will be presented

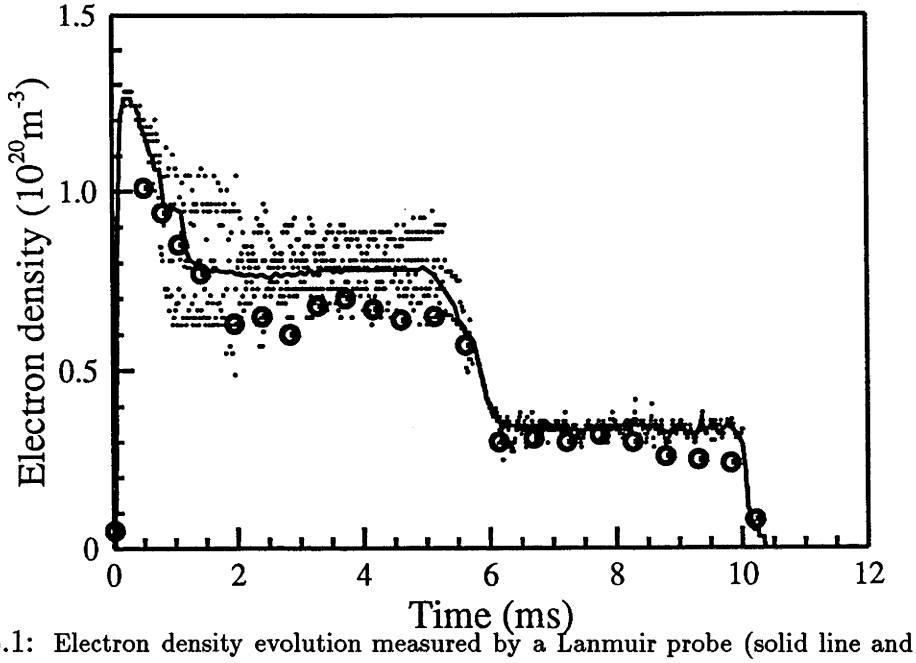

Figure 6.1: Electron density evolution measured by a Lanmuir probe (solid line and small dots) and microwave interfrometer (o).

and the last section of this chapter will contribute to the discussion of the plasma parameters together with some spectroscopic results presented in Chapter 4.

6.1 Electron density

The electron density measurement is carried out over a range similar to that used to study the optical properties of the plasma. The applied magnetic field ranges from 0.04 to 0.15T, and the filling pressure range of 0.3 to 0.8 Pa has been chosen to cover the range in which a reproducible plasma in the mode of interest can be produced. The rf power input ranges from 1 to 5kW. Pulse durations in the experiments are adjusted to allow the final steady state to appear. Fig 6.1 shows the typical time evolution of the central electron density for filling pressure of 0.9Pa, B_0=0.075T and rf input of 3.5kW, measured by a Langmuir

probe. The central density evaluated from the 3 mm microwave interferometer measurement is also included in this figure (o). The good agreement between the results from two independent diagnostics confirms the reliability of the results from Langmuir probe measurement. Henceforth, only the results from Langmuir probe measurements will be presented. The density increases quickly and reaches its peak in less than 0.2ms, and then reaches its first steady level in 1-2ms, depending mainly on the filling pressure and input power. After 1-10 ms, also depending on the filling pressure and input power, the density drops and reaches its second steady value. The peak density can reach a value as high as 3-4 times that of the second plateau.

To understand the character of the curve, it is convenient to divide it into three regions, the head, the first plateau, and the second plateau. Since the density profile is highly peaked at the axis (Fig 6.2), it is reasonable to assume that the rf power is deposited mainly near the axis of the plasma. Initially, ionization in a relatively cold neutral gas environment is the dominant process and the electron density on the axis quickly increases to its peak value. The gas is then heated near the axis and the neutral density in the region of the axis is rapidly reduced to zero due to both ionization and the outward diffusion to the colder part of the tube and then to be pumped out. It is no surprise that the electron density as a function of the time becomes relatively steady, since the ionization rate will eventually be balanced by the charged particles loss rate. From Fig 6.1, one finds the density evolution is quite noisy during this period, which implies a strong interaction between the helicon waves and the charged particles resulting in some kind of instability.

As the background plasma is finally heated up, the density of the neutral

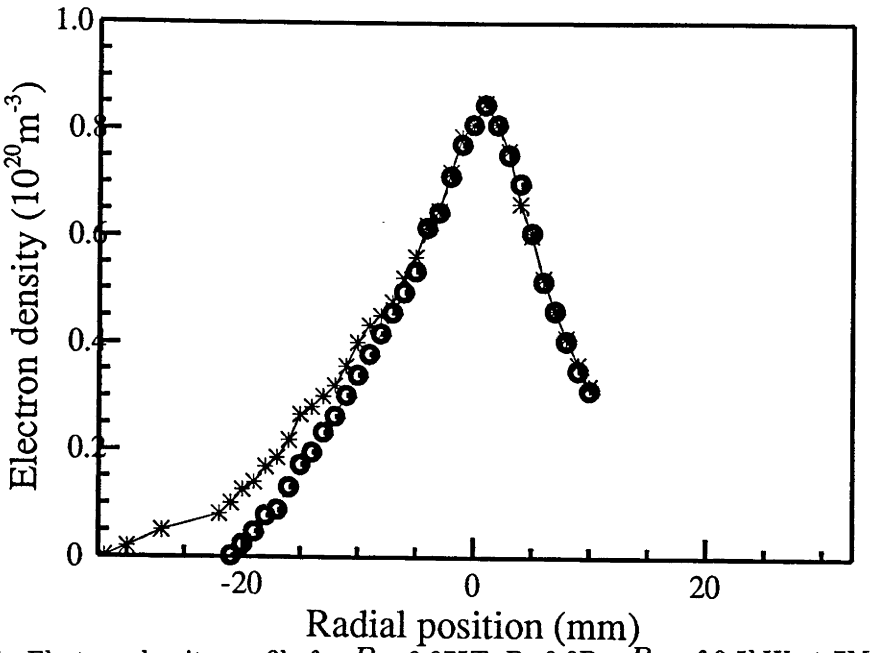

Figure 6.2: Electron density profile for B_0=0.075T, P=0.9Pa, P_{rf} of 3.5kW at 7MHz, and for tube diameter of 45mm (o) and 65mm (*).

atoms near the axis zone is reduced to a critical value so that the supply of the neutral atoms is not enough to support the ionization rate required by a given plasma wave mode. This shortage of neutral atoms on the axis forces the plasma wave mode to change, resulting in lower rf-plasma coupling efficiency and hence the density drops to a much lower but less noisy steady level. The density at the first plateau is of special interest since the peak in optical gain of the 488nm argon ion transition is observed at this time. It has also been found that the electron density for the first plateau is not very sensitive to the tuning of the rf matching circuit providing that the tuning is not far from the optimal position while slight change in tuning will cause serious change in the density at the second plateau. Hence attention is paid only to the density of the first plateau. Later, the density of the first plateau will be referred to for convenience unless otherwise stated.

The radial profile of the electron density for B_0 of 0.075T, P of 0.9Pa, rf input

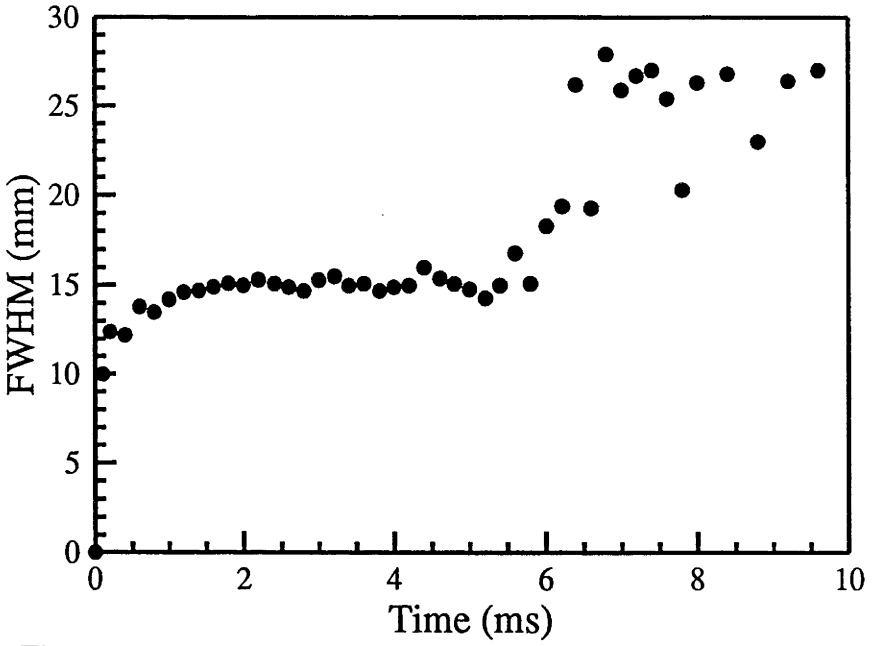

Figure 6.3: Time evolution of the FWHM of the electron density.

power of 3.5kW is shown in Fig 6.2, with Curve 1 (o)for tube diameter of 45mm and Curve 2 (*) for tube diameter of 65mm. From Fig 6.2, it is obvious that the plasma has a dense core ~15mm in diameter which is nearly independent of the tube diameter. This result is consistent with the profile of the spontaneous emission as would be expected. The density profile can be roughly described by

$$n(r) = \begin{cases} n_{e0}(1 - \frac{r}{2r_h}) & r \leq r_h \\ \frac{n_{e0}}{2}(1 - \frac{r - r_h}{R - r_h}) & r > r_h \end{cases} \tag{6.1}$$

where r_h is the half width of half maximum of the profile and R is the tube radius. The volume mean density can then be estimated as

$$\bar{n} = n_{e0}(\frac{r_h^2}{3R^2} + \frac{r_h}{6R} + \frac{1}{6}) \tag{6.2}$$

The FWHM of the profiles of the density for various experimental conditions are plotted in Fig 6.3 to Fig 6.5. The central electron densities and volume averaged density as functions of the filling pressure are shown in Fig 6.6. The applied magnetic field and the RF power input for Fig 6.6 are 0.075T and 3.5kW

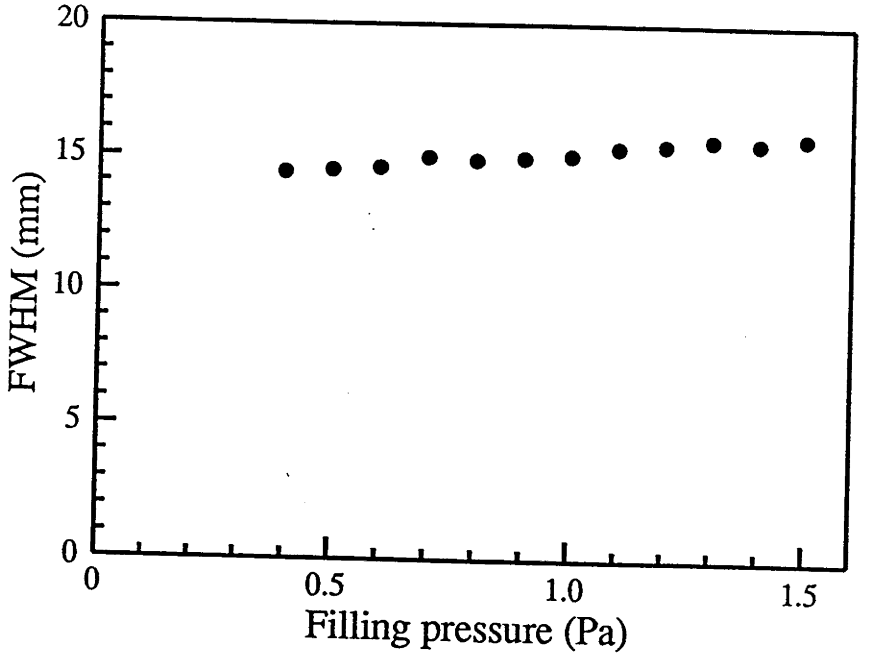

Figure 6.4: FWHM of the electron density density as a function of filling pressure.

respectively. It is found that the central density is nearly independent of the filling gas pressure (Fig 6.7) but the mean density is proportional to the filling pressure, due to the slightly widened profile.

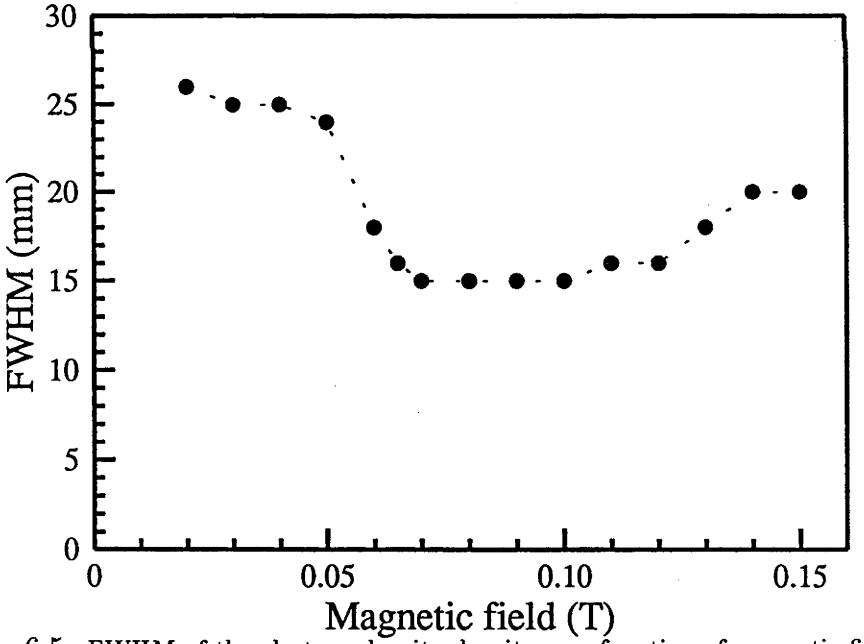

Figure 6.5: FWHM of the electron density density as a function of magnetic field.

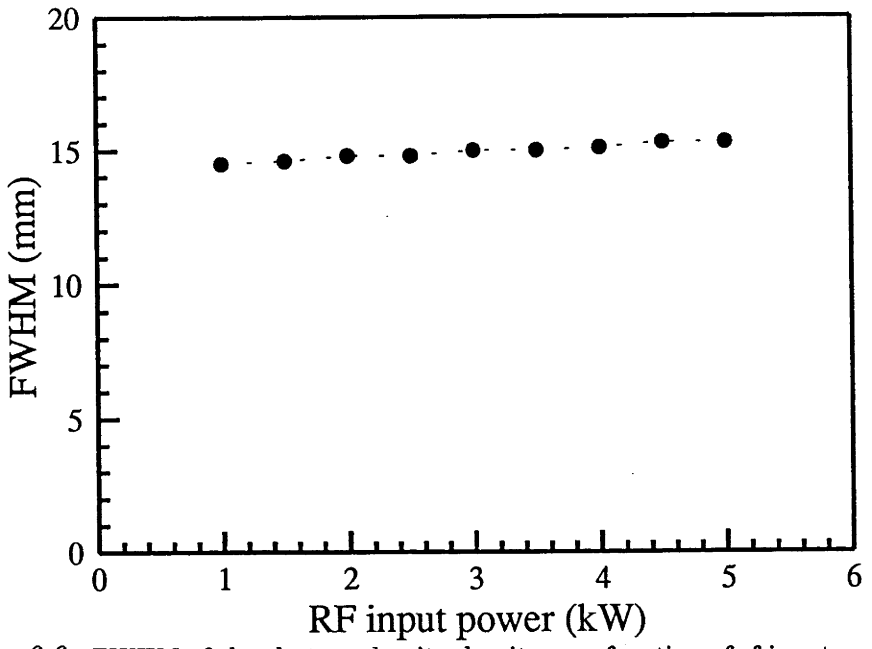

Figure 6.6: FWHM of the electron density density as a function of rf input power.

The central and mean densities as functions of longitudinal magnetic field are shown in Fig 6.8. The central density increases with the magnetic field for $B_0 <$ 0.1 T, and then slightly decreases to a constant value. Notice that when $B_0 >$ 0.12T, the density profile becomes wider (Fig 6.4), i.e. the 'axis zone' increases, so that the mean electron density increases again. The filling pressure and the rf power input are fixed at 0.9 pascal and 3.5 kW for Fig 6.7 and Fig 6.8. The measured central density is plotted as function of rf input power in Fig 6.9. The density increases with the rf input power. There is some indication of saturation in density when rf input power is over 2.5kW. This can be explained by the fact of nearly 100% ionization near the axis. The slight further increase in the density after 3.5kW can be explained by the contribution from doubly ionized ions.

It can be summarized from the above results that the electron density as a function of time has an initial peak and then reaches a relatively steady state after about 2ms. This relatively steady state can last for a few milliseconds, depending

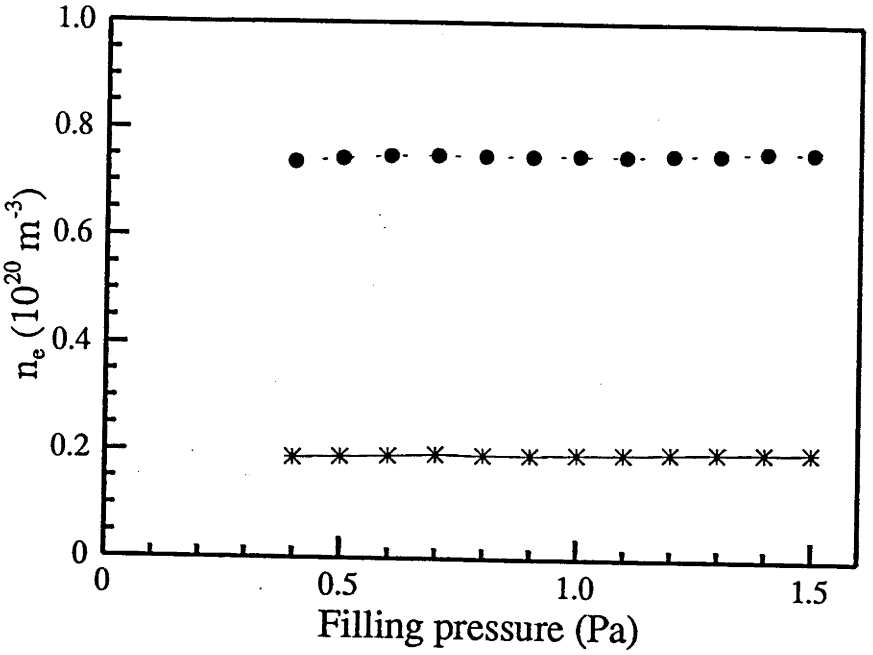

Figure 6.7: The central (•) and mean (∗) electron densities as functions of filling pressure

on the filling pressure and input power, and then suddenly drops to a much lower value which lasts until the plasma is turned off. The density is highly peaked on the axis at the first plateau but widens at the second plateau. The central density at the first plateau is independent of the filling gas pressure within quite

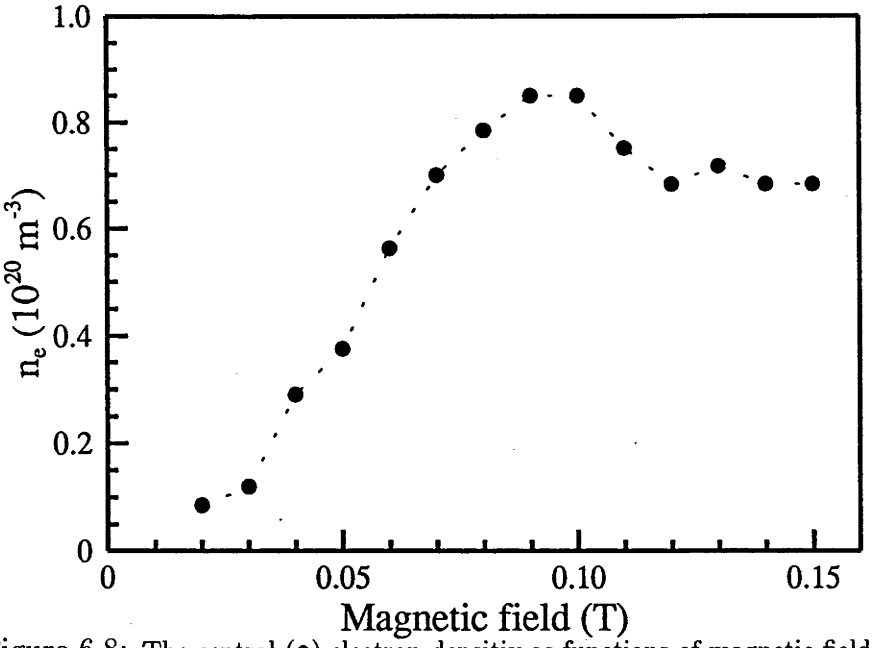

Figure 6.8: The central (•) electron densitiy as functions of magnetic field.

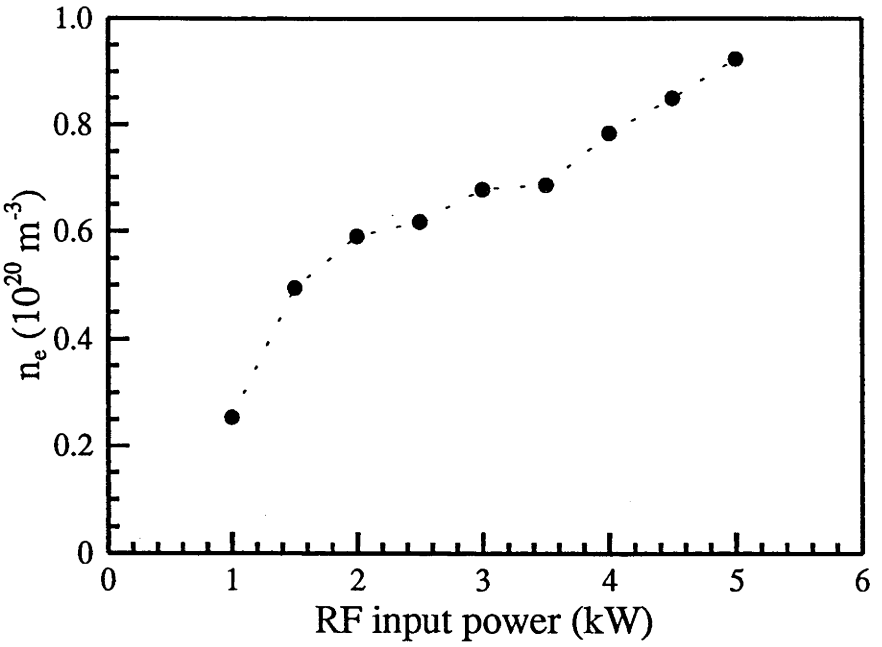

Figure 6.9: The central electron density as a function of rf input power.

a range but is approximately proportional to the rf input power before saturation occurs. One interesting results is that the FWHM of both the optical emission and the electron density are nearly independent of the filling pressure, rf power, rf frequency and even tube diameter. This fact suggests some important physics of this discharge, but further investigation is required to fully understand its origin. Both the value of the central density and the FWHM of its profile are sensitive to the longitudinal magnetic field. The maximum electron density on axis of the plasma in Basil-II is $\sim 10^{20} m^{-3}$.

6.2 Electron energy distribution function

The experiments for measuring the electron energy distribution function are carried out by means of a negatively biased Langmuir probe under the following conditions:

Argon filling pressure : 0.9Pa;

Input rf power : 1.5-5kW, 7MHz;

Axial magnetic field : 0.04-0.14T.

As mentioned in the chapter 3 of the thesis, an iterative tracing method is used in this study to obtain the electron distribution from the measured Langmuir probe data.

It is found that the measured probe characteristics for various experimental conditions can be reasonably fitted by the characteristics calculated from the distribution functions with the general form of:

$$F = \sqrt{eV} \times (f_1 + f_2 + f_3) \tag{6.3}$$

where f_1 is the Maxwellian distribution:

$$f_1 = n_e \sqrt{\frac{m_e}{\pi k T_e}} e^{-\frac{eV}{kT_e}}, \tag{6.4}$$

f_2, the tail 'hole burning' function.

$$f_2 = S_1 \times f_1 \times e^{-S_2 \times \frac{e|V_r - V|}{kT_e}} \tag{6.5}$$

here $0 \geq S_1 \geq -1$, and $S_2 \sim 20$ are parameters which characterise the 'hole burning' depth and width respectively; and f_3, the distribution of an electron beam:

$$f_3 = n_b \sqrt{\frac{m_e}{\pi k T_b}} e^{-\frac{e|V_b - V|}{kT_b}}, \tag{6.6}$$

with $T_b \simeq \Delta E_b \frac{\Delta E_b}{4eV_b}$ and ΔE_b, the beam e^{-1} spread half-width in eV. The parameters which define the distribution function are determined using an iterative tracing method to fit the measured Langmuir probe data for various experimental conditions. The variation of the electron distribution tail as a function of experimental conditions can thus be interpreted from the probe data.

Table.6-1 lists the all the parameters which define the electron distribution for various conditions. The first four columns of the Table give the time from rf switch on, axial magnetic field, input rf power, and the radial position of the probe while the rest gives the parameters.

Fig 6.10 shows the nonthermal electron tails for various times after the initiation of the plasma. A Maxwellian distribution is also plotted for comparison. The distribution is measured on the axis of the plasma for B_0=0.075T, input power of 3.5kW. It can be seen that there is a depletion of the tail, compared to the Maxwellian distribution, in the the range of 22-32eV. This energy range is important for the excitation of the upper levels of the Ar^+ visible transitions, which have excitation energies in the range 18-22eV. This result can explain the unusual big difference between the electron density and the emission evolution, as will be discussed in the last section of this chapter.

In the following discussion, we will concentrate our attention on the high energy electron beam term (f_3), which can be expressed by three parameters, the beam energy E_b=eV_b, beam e^{-1} spread ΔE_b, and the normalized beam density n_b/n_e. Fig 6.11 shows these three parameters as a function of time, and this is a representation of the main results shown in Fig 6.10. From Fig 6.11 one can see more clearly that the beam energy increases while the beam spreads and decays in density with time. However, the flux remains relatively constant. It is curious that the beam lasts for such a long time (~1ms), as contrasted with the knowledge of fast decay of a beam-like distribution due to beam-plasma instability. This means that there must be some mechanism which keeps driving the beam for as long as 1ms. It has been reported that an electron beam will be

t(ms)	B_0(G)	P_{rf}(kW)	r(mm)	S_1	S_2	V_r	V_b	ΔE_b	T_e	n_b/n_e (10^{-4})
0.2	750	3.5	0	0.5	20	22	27	8	5	4.0
0.4	750	3.5	0	0.8	20	25	39	8	5	8.0
0.6	750	3.5	0	0.8	20	25	54	9	5	7.0
0.8	750	3.5	0	0.85	20	30	71.5	12	5	6.8
1.0	750	3.5	0	1	20	30	88	15	5	6.0
1.2	750	3.5	0						5	0
0.6	750	3.5	0	0.8	20	25	60	11	5	7.1
0.6	750	3.5	2	0.7	20	27	50	9	5	5.4
0.6	750	3.5	4	0.4	20	28	45	7	5	3.0
0.6	750	3.5	6	0			40	4	5	1
0.6	750	3.5	7	0			33	4	5	0.4
0.6	750	3.5	9						5	0
0.6	750	3.5	11						5	0
0.6	750	3.5	13.5						5	0
0.6	750	3.5	18.5						4.2	0
0.6	750	1.5	0						5	0
0.6	750	2	0	0.75	20	26	37	9	5	6
0.6	750	2.5	0	0.8	20	26	40	9.5	5	7
0.6	750	3	0	0.8	20	26	47	10	5	8.6
0.6	750	3.5	0	0.80	20	25	54.5	11	5	9.6
0.6	750	4	0	0.85	20	25	56	11.5	5	10.4
0.6	750	4.5	0	0.85	20	25	67	13	5	11.2
0.6	750	5	0	0.85	20	25	79	15	5	12
0.5	500	3.5	0						5	0
0.5	600	3.5	0	0.4	20	24	36.5	5	5	2
0.5	650	3.5	0	0.6	20	24	41.5	6.5	5	4
0.5	700	3.5	0	0.8	20	25	42	7	5	7.5
0.5	750	3.5	0	0.8	20	25	43.5	7	5	9
0.5	800	3.5	0	0.8	20	27	48.5	10	5	8.5
0.5	850	3.5	0	0.8	20	27	48	10	5	8.5
0.5	900	3.5	0	0.8	20	26	50.3	10	5	8.5
0.5	1000	3.5	0	0.8	20	25	47	11	5	7.5
0.5	1100	3.5	0	0.8	20	25	45	11	5	7.5
0.5	1200	3.5	0	0.8	20	25	41.5	10	5	7.0
0.5	1300	3.5	0	0.8	20	25	42	10	5	6.8
0.5	1400	3.5	0	0.7	20	24	40	10	5	6.4

Table.6-1 Parameters of the Electron Energy Distribution Function

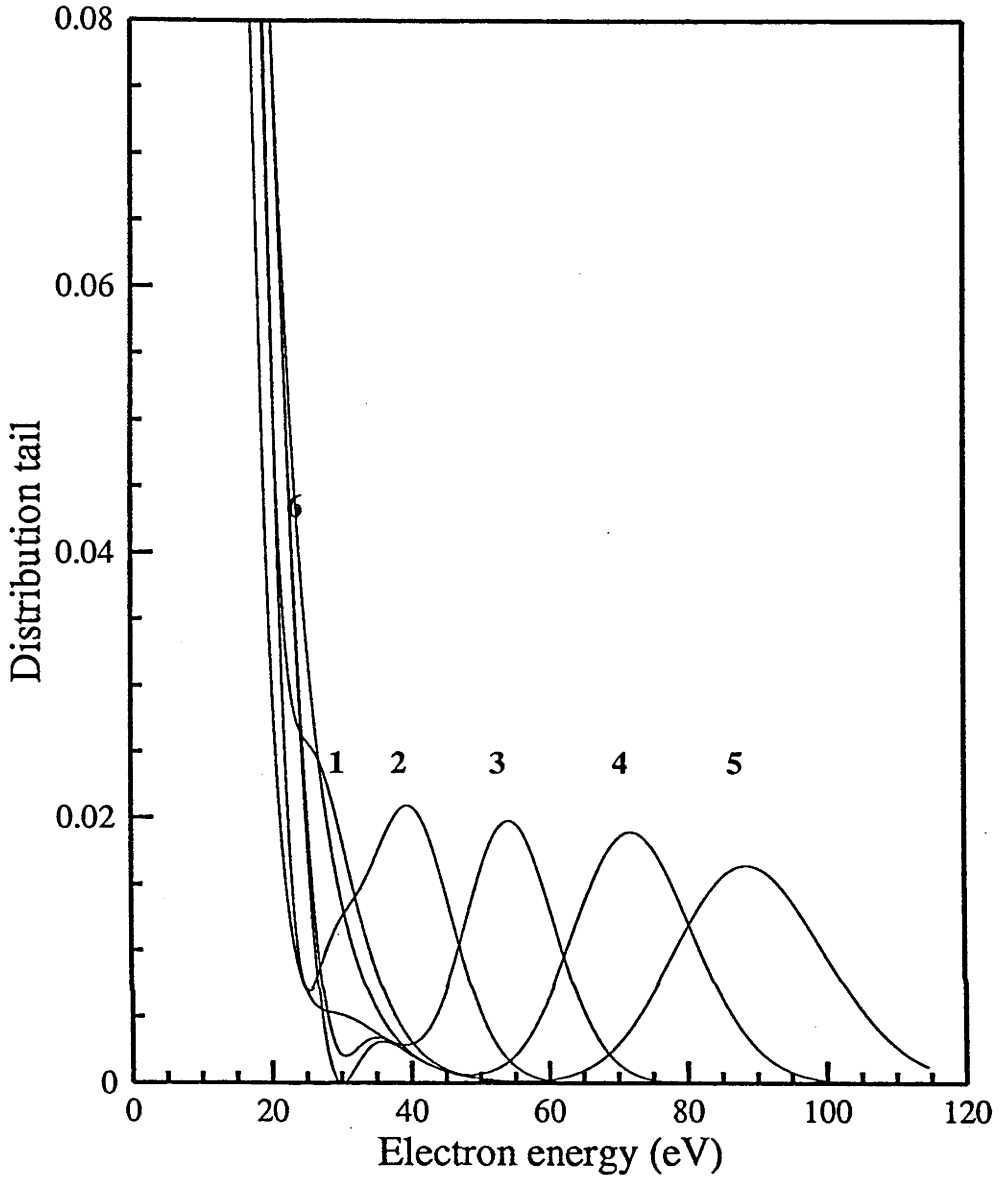

Figure 6.10: The tails of electron distribution for (1) t=0.2ms, (2) t=0.4ms, (3) t=0.6ms, (4) t=0.8ms, (5) t=1ms, and (6) a Maxwillian of 5eV.

absorbed by the plasma to form a flattened nonthermal electron tail within a time $t \sim 50$ nsec, and the equilibrium time for the thermalization of the electron tail is typically 3-5 electron-electron collision times[36]. In this plasma, the electron-electron collision time can be estimated as $t_{ee} = 1/\mu_{ee} = 2 \times 10^{-9}$s. This suggests the mechanism has to be strong enough to overcome not only the fast decay due to the beam-plasma instability but also the thermalization of the tail due to

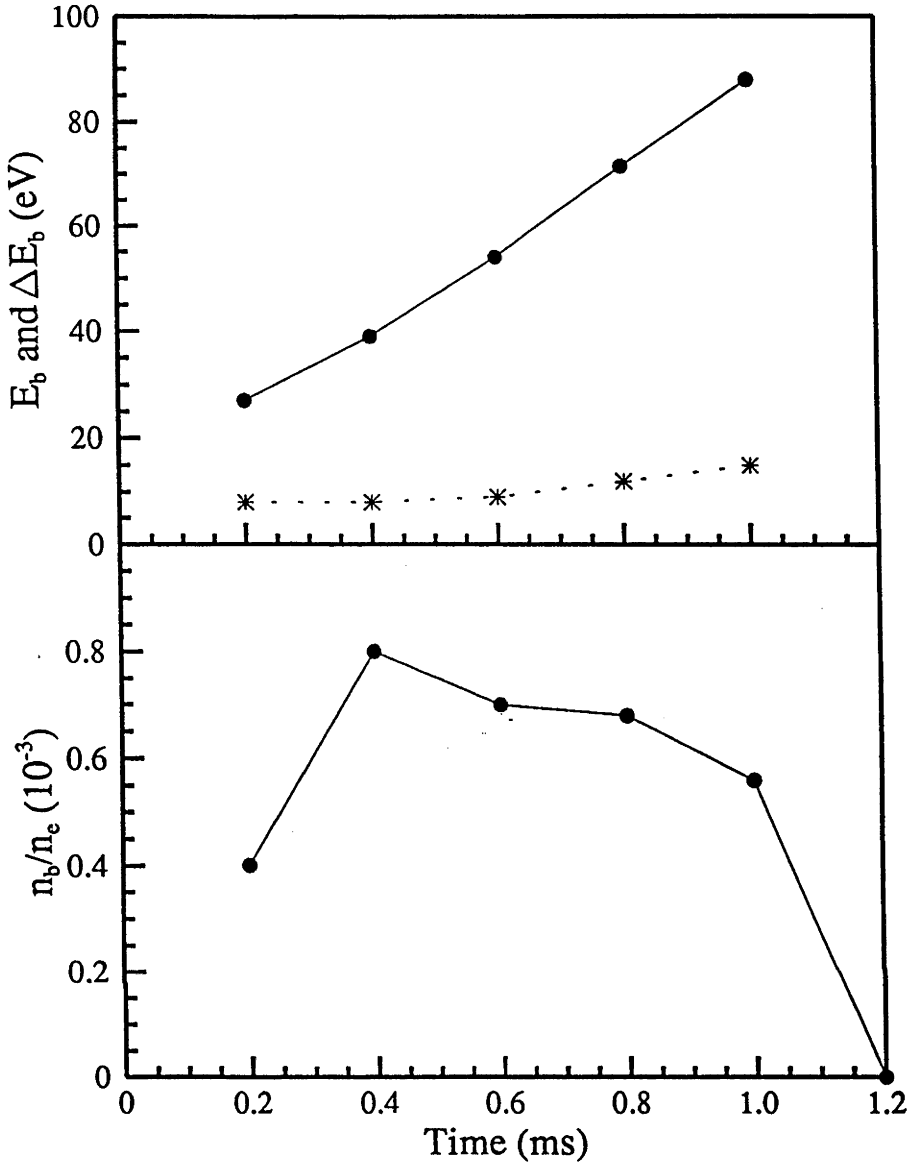

Figure 6.11: E_b (a, •), ΔE_b (a, *), and n_b (b) as functions of time.

electron-electron collision.

The radial profiles of these three parameters are shown in Fig 6.12. The plasma operation condition for Fig 6.11 and Fig 6.12 is the same as that for Fig 6.10. From Fig 6.12 we can see the beam is restricted radially and is the densest with highest energy on axis. For $r > 10$mm, there is no trace of the nonthermal tail and the distribution is Maxwellian with $T_e \sim 5$eV. As a function

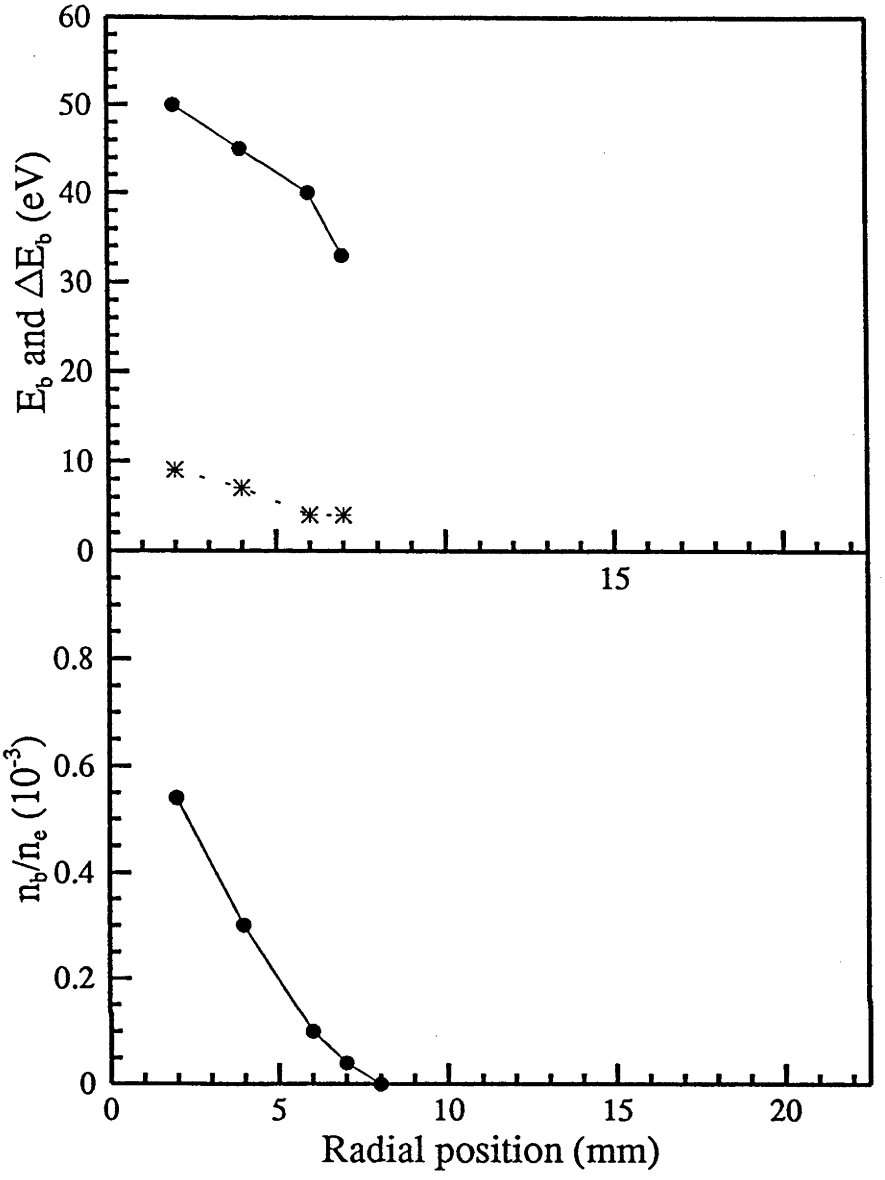

Figure 6.12: E_b (a, •), ΔE_b (a, ∗), and n_b (b) as functions of radial position.

of input rf power (Fig 6.13), all $E_b(\bullet), \Delta E_b(*)$, and n_b increase after a threshold power of 2kW. The distributions for powers lower than this threshold is close to Maxwellian with $T_e \sim$ 3-5eV. The beam parameters also depend on the axial magnetic field (Fig 6.14). There is no trace of the nonthermal tail until B_0=0.06T, when the beam density jumps. This sudden jump could imply some resonant mechanism. There are peaks in both E_b and n_b, but at different field B_0=0.09T (Fig 6.14a) and B_0=0.075T (Fig 6.14b). Note the peak in the beam density

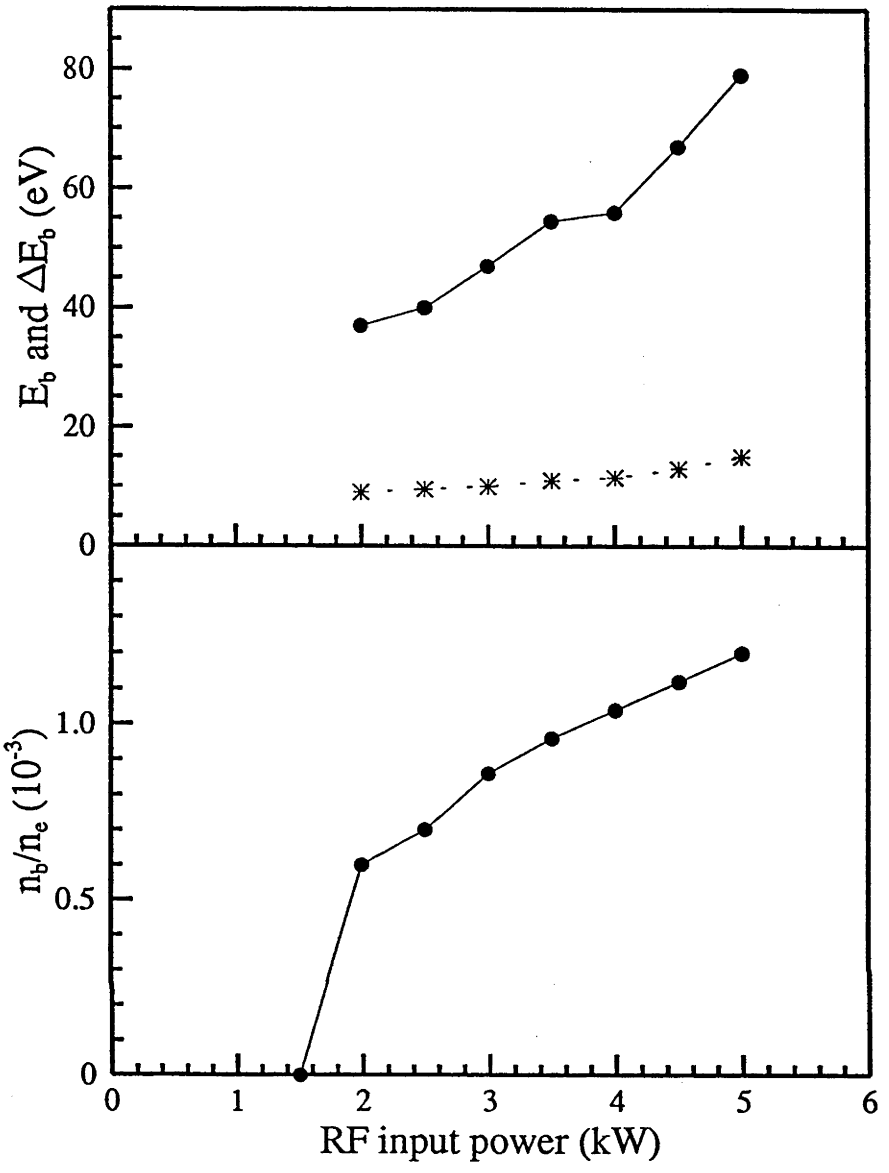

Figure 6.13: E_b (a, •), ΔE_b (a, *), and n_b (b) as functions of rf input power.

appears at a magnetic field (0.075T) close to that (0.068T) required for the lower hybrid resonance condition:

$$f_{rf} = f_l,$$

where f_{rf}=7MHz is the excitation radio frequency and $f_l = \frac{1}{2\pi}\sqrt{\omega_{ci}\omega_{ce}}$ is the lower hybrid frequency. The applied magnetic field for Fig 6.13 is 0.075T and the rf power input for Fig 6.14 is 3.5kW. Experiments carried out by using an

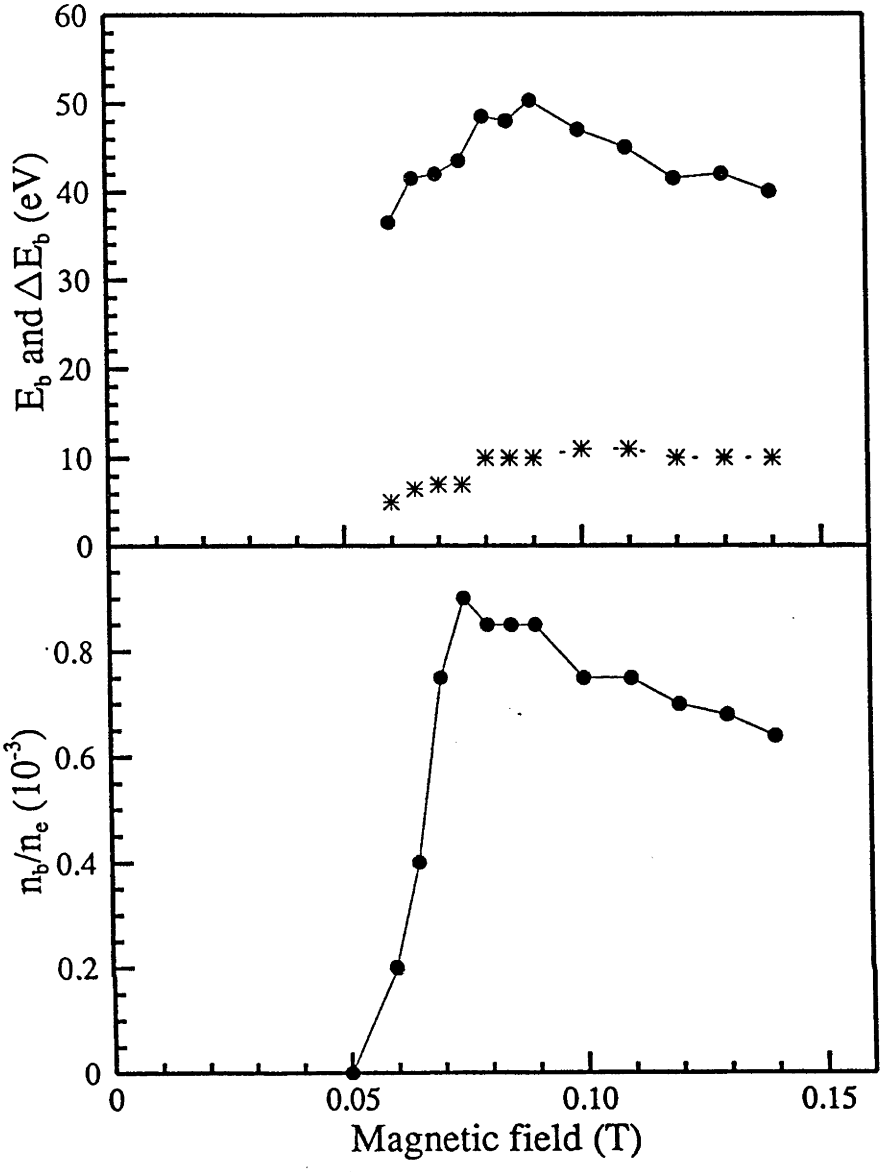

Figure 6.14: E_b (a, •), ΔE_b (a, *), and n_b (b) as functions of magnetic field.

asymmetric probe suggest that the high energy electrons do not have a preferred axial direction. This means this distribution does not form a net electron current.

To summarize the results, nonthermal electron distribution tails have been observed near the axis of an argon plasma, which is excited by rf at 7MHz by an external double loop antenna. The tail of the distribution has a bump at 30-80eV and a dip at 20-30eV. The nonthermal tail appears at the beginning of the

plasma pulse when input rf power exceeds 2kW, axial magnetic field B_0 >0.06T. It can last for a time of 1ms. The energy of the electron beam is approximately proportional to both time and input rf power, while the density of the beam decreases with time but increases with input power. There is a peak in the beam density at B_0=0.075T, which is close to that required by the lower hybrid resonance, and a peak in beam energy at B_0=0.09T. The mechanism responsible for this nonthermal distribution tail is not yet known.

6.3 Phase velocity of the helicon wave

The wavelength of the helicon wave is measured by the magnetic probe described in Chapter 3. Only the B_r component of the wave field is measured to derive λ, the wavelength of the wave. The phase velocity is then calculated from the measured wavelength $v_{ph} = \omega_{rf}/k = f_{rf}\lambda$. It is clear from all the experimental results presented above in this thesis that the plasma behaviour is sensitive to the longitudinal magnetic field, and there is a range of B_0 where some resonance could exist. Therefore, the wavelength of the wave is measured at t=0.2ms after plasma initiation as a function of longitudinal magnetic field for filling argon pressure of 0.9Pa, rf input power of 3.5kW at 7MHz. The phase velocity as a function of magnetic field is shown in Fig 6.15, from which one can see that v_{ph} of the m=1 helicon standing wave is again a magnetic field sensitive parameter like the other parameters, and has its minimum at B_0 ~0.065-0.10, the resonant B_0 range for the 488nm emission.

To look into the interaction between the m=1 helicon wave and the charged

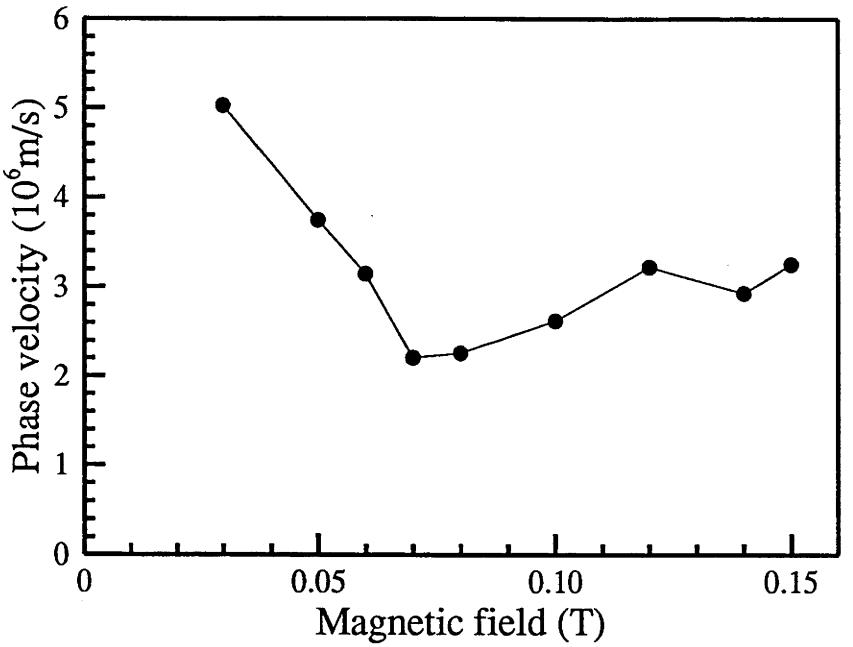

Figure 6.15: Phase velocity of the m=1 helicon wave as a function of magnetic field.

particles, it is convenient to use the phase velocity equivalent energy:

$$E_{ph} = \frac{m_e v_{ph}^2}{2}.$$

One finds that the energy equivalent to the phase velocity of the helicon wave in Basil-II plasma has a minimum value ~15eV (Fig 6.16) in the optimal B_0 range for the best performance of the laser. This energy is close to the excitation energy of the upper level of the 488nm argon ion transition (19.6eV) suggesting a selective excitation mechanism for the population inversion of this plasma. A possible explanation for this result will be discussed in the next chapter.

6.4 Comparison of the results

It is now possible to see the plasma with a background of not only the results from the plasma parameter measurements but also those from the optical property measurements. Fig 6.17 shows the central electron density, the 488nm emission,

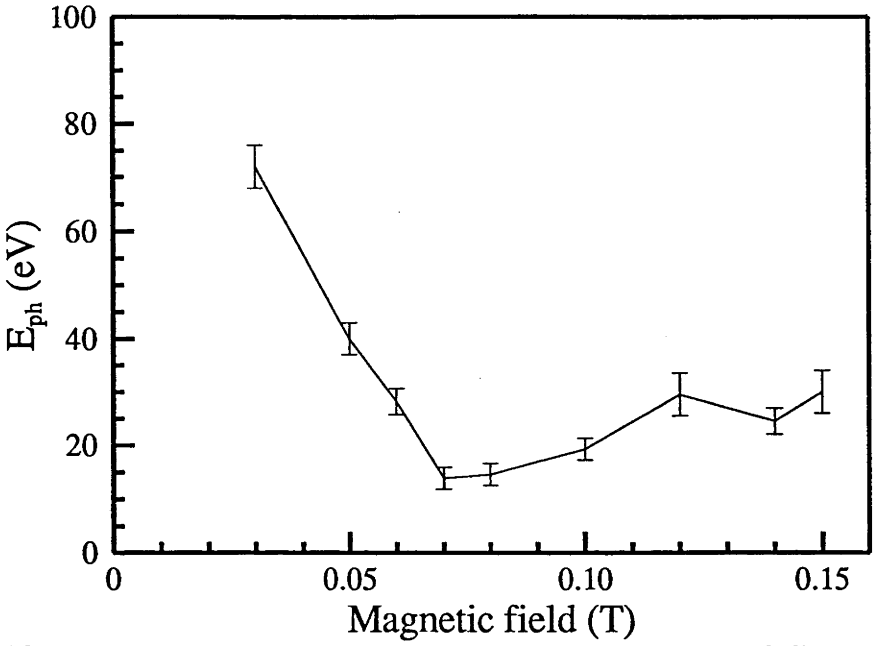

Figure 6.16: The energy equivalent to the phase velocity of the m=1 helicon wave as a function of magnetic field.

laser output of the 488nm transition, FWHM of the emission and density radial profiles, and the phase velocity equivalent energy of the m=1 helicon wave as functions of longitudinal magnetic field. It is clear that all the parameters are sensitive to the B_0 field and most of them have maximum or minimum in the B_0 range of 0.065-0.10T. This strongly suggests that there is a magnetic field sensitive energy transfer process, which is resonant at $B_0 \sim$0.08T. Although the optimal magnetic field for the electron beam is very close to that for the laser action (Fig. 6-14), we believe this abnormal electron energy distribution is not, or at least not directly, responsible for the population inversion in this discharge, since significant optical gain is observed only when the electron beam has nearly disappeared (Fig. 6-18). This is supported by the fact that there is no obvious difference between the laser action for the long pulse operating mode and that for the dc operating mode.

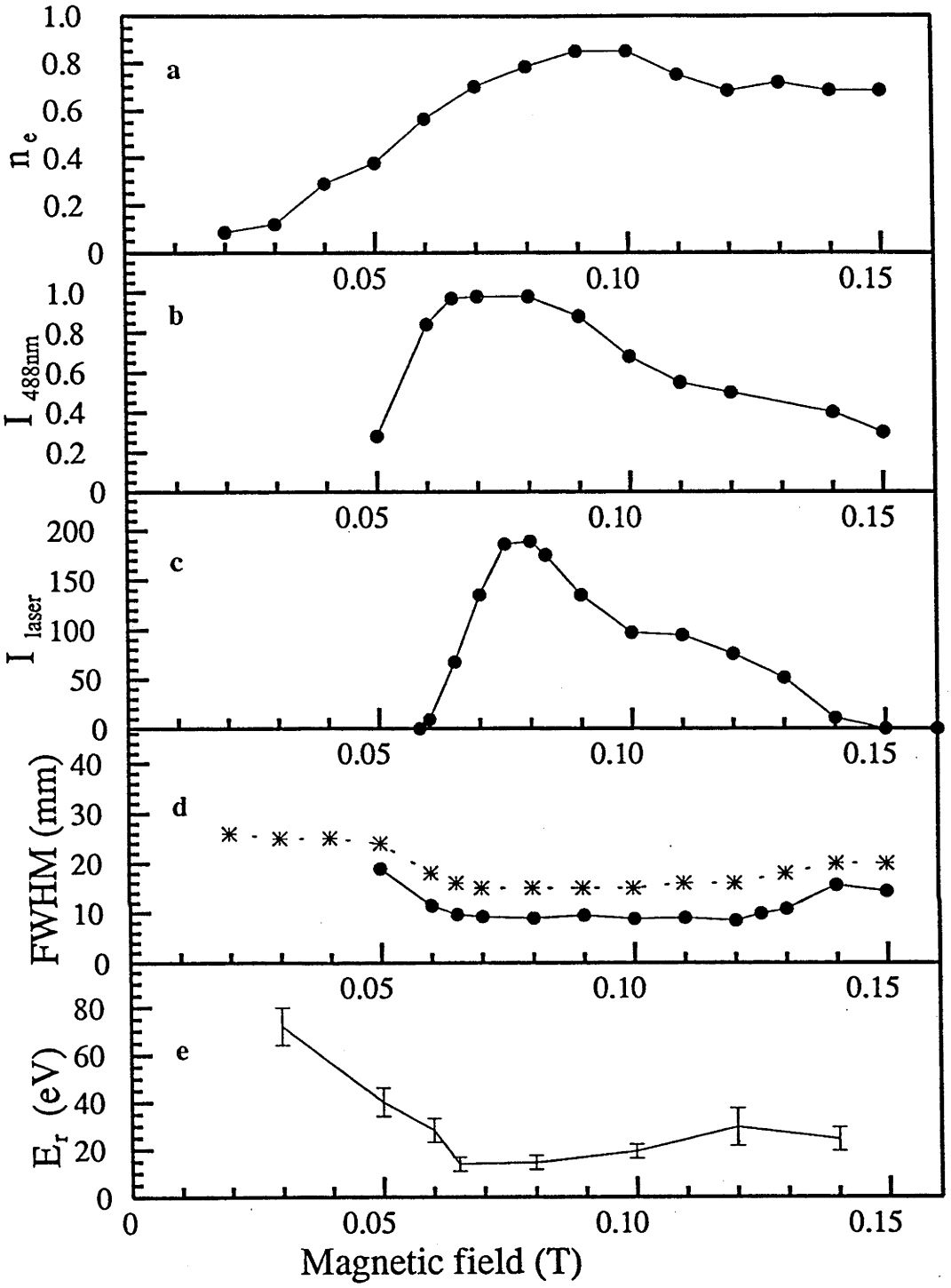

Figure 6.17: Electron density (a, in unit of $10^{20}m^{-3}$), spontaneous emission of the 488nm transition (b, arb unit), laser output of the 488nm transition (c, arb unit), FWHM of density (d, dotted line) and emission (d, solid line) profiles, and the energy equivalent to the phase velocity as functions of magnetic field.

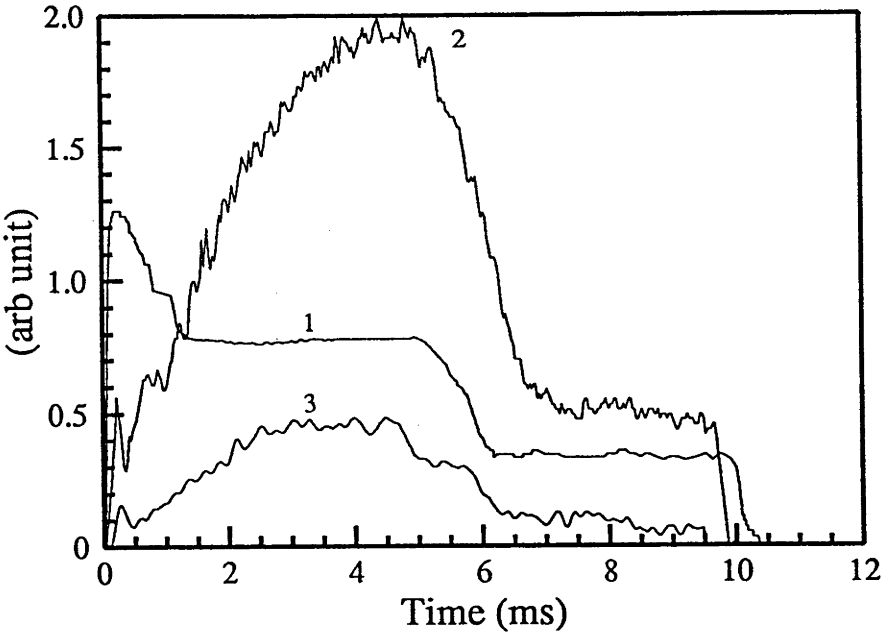

Figure 6.18: Time evolutions of (1) electron density, (2) spontaneous emission, and (3) optical gain

The time evolution of electron density (smoothed), spontaneous emission and stimulated emission of the Ar^+ 488nm transition are plotted together in Fig 6.18.

It is curious to find that the maxima of the emissions do not correspond to the maximum of the density as normally expected. The emission intensity is very low and the electron density has a maximum in the first 1ms of the plasma pulse and the peak(first 1-2ms) of the density FWHM evolution (Fig 6.3) is not consistent with that of the emission FWHM evolution although the rest of the curve does. This can be explained as a result of a low excitation rate due to the lack of electrons in the 22-32eV range and a relatively higher ionization rate due to the bump in the energy range of 30-80eV. The unusually sharp peak in the emission at t$\sim$0.2ms can be explained by the distribution at t=0.2ms, which has relatively more electrons in the range of 22-32eV. The integral of the electron energy distribution function over 22-32eV, which is normalized by an

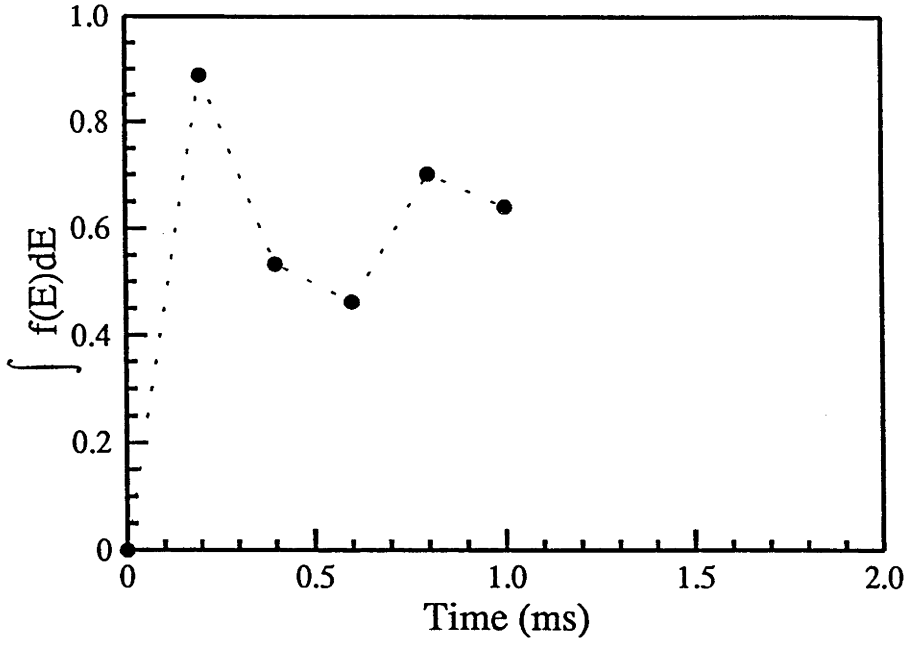

Figure 6.19: The integral of the electron distribution tail over 22-32eV, which has been normalized to that of a Maxwellian of 5eV, as a function of time.

integral of Maxwellian of 5eV, as a function of time is shown in Fig 6.19. The energy distribution can not be measured accurately after t=1.0ms due to the large oscillation in density, which could be a sign of strong energy transfer between the m=1 helicon wave and the charged particles in the discharge. However, the fact that a higher emission intensity occurs at a lower electron density when 2ms $> t >$ 6ms implies that the integral of the electron energy distribution function over the range of interest at that time might well be more than maxwellian. This is also supported by the results from the helicon wave phase velocity measurement, which suggests a selective excitation mechanism. A possible explanation of this feature will be discussed in the next chapter.

Chapter 7

Possible explanation of the population inversion

A possible theoretical explanation of the population inversion mechanism is investigated in this chapter. Section 1 derieves the helicon wave dispersion relation in a uniform cold plasma with cylindrical symmetry. Section 2 presents the theoretical calculation of m=1 helicon wave phase velocity as a function of magnetic field and compares it with the experimental results. The last section discusses the Landau damping of the m=1 helicon wave and shows it as a reasonable explanation for the population inversion mechanism in this plasma.

7.1 Dispersion relation

The dispersion relation is given in this section where the analysis of Chen[40] is followed.

For a cold uniform collisionless plasma, the Helicon waves satisfy the equations:

$$\nabla \times \vec{E} = -\frac{\partial \vec{B}}{\partial t}; \tag{7.1}$$

$$\nabla \times \vec{B} = \mu_0 \vec{j}; \tag{7.2}$$

$$\vec{E} = \vec{j} \times \vec{B}/en_e. \tag{7.3}$$

If the perturbations have the form of $e^{i(m\theta+kz-\omega t)}$, one has:

$$\nabla^2 \vec{B} + \alpha^2 \vec{B} = 0, \tag{7.4}$$

where

$$\alpha \equiv (\frac{\omega}{k})(\frac{e\mu_0 n_e}{B_0}). \tag{7.5}$$

The components of Eq.7.4 in cylindrical geometry are:

$$\nabla^2 B_r - \frac{2}{r^2}\frac{\partial B_\theta}{\partial \theta} - \frac{B_r}{r^2} + \alpha^2 B_r = 0; \tag{7.6}$$

$$\nabla^2 B_\theta - \frac{2}{r^2}\frac{\partial B_r}{\partial \theta} - \frac{B_\theta}{r^2} + \alpha^2 B_\theta = 0; \tag{7.7}$$

$$\nabla^2 B_z + \alpha^2 B_z = 0, \tag{7.8}$$

where

$$\nabla^2 = \frac{1}{r}\frac{\partial}{\partial r}(r\frac{\partial}{\partial r}) + \frac{1}{r^2}\frac{\partial^2}{\partial \theta^2} + \frac{\partial^2}{\partial z^2}$$

Fourier analysing in θ and z, one obtains

$$B_r'' + \frac{1}{r}B_r' + (\alpha^2 - k^2 - \frac{m^2+1}{r^2})B_r) - i\frac{2m}{r^2}B_\theta = 0; \tag{7.9}$$

$$B_\theta'' + \frac{1}{r}B_\theta' + (\alpha^2 - k^2 - \frac{m^2+1}{r^2})B_\theta) - i\frac{2m}{r^2}B_r = 0; \tag{7.10}$$

$$B_z'' + \frac{1}{r}B_z' + (\alpha^2 - k^2 - \frac{m^2}{r^2})B_z) = 0. \tag{7.11}$$

Define a new variable ρ such that

$$\rho^2 = (\alpha^2 - k^2)r^2$$

Eqs.7.9-7.11 can then be written as

$$L_{m^2+1}(B_r) - i\frac{2m}{\rho^2}B_\theta = 0; \tag{7.12}$$

$$L_{m^2+1}(B_\theta) - i\frac{2m}{\rho^2}B_r = 0; \tag{7.13}$$

$$L_{m^2}(B_z) = 0; \tag{7.14}$$

where $L_{m^2} = \frac{\partial^2}{\partial\rho^2} + \frac{1}{\rho}\frac{\partial}{\partial\rho} + (1 - \frac{m^2}{\rho^2})$ is the Bessel operator. Introducing left-handed and right-handed circularly polarized components

$$B^L = \frac{B_r + iB_\theta}{\sqrt{2}}$$

$$B^R = \frac{B_r - iB_\theta}{\sqrt{2}}$$

one has

$$L_{(m-1)^2}B^R = 0; \tag{7.15}$$

$$L_{(m+1)^2}B^L = 0; \tag{7.16}$$

$$L_{m^2}B_z = 0. \tag{7.17}$$

The solution for Eqs.7.15-7.17 can be written in terms of left-handed and right-handed circularly polarized components B^R, E^R, B^L, and E^L:

$$B^R = A(\alpha + k)J_{m-1}(Tr) = -i(\frac{k}{\omega})E^R \tag{7.18}$$

$$B^L = A(\alpha - k)J_{m+1}(Tr) = i(\frac{k}{\omega})E^L \tag{7.19}$$

$$B_z = -i\sqrt{2}ATJ_m(Tr), \quad E_z = 0. \tag{7.20}$$

Here J_m is a Bessel function of the first kind and T is the transverse wave number defined by:

$$T^2 = \alpha^2 - k^2. \tag{7.21}$$

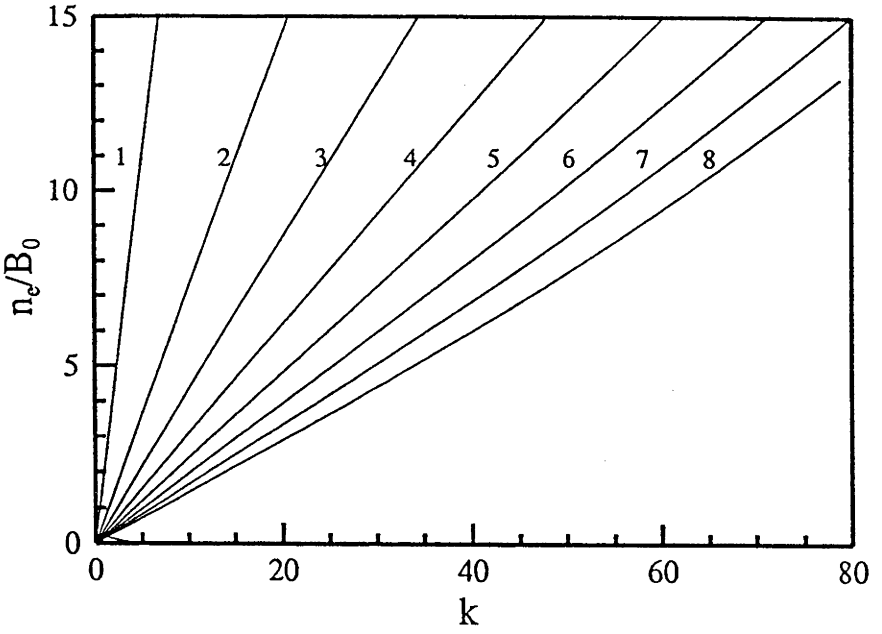

Figure 7.1: Dispersion of the m=1 helicon wave for plasma radius of (curve 1) 1mm, (curve 2) 3mm, (curve 3) 5mm, (curve 4) 7mm, (curve 5) 9mm, (curve 6) 11mm, (curve 7) 13mm, and (curve 8) 15mm.

Both insulating and conducting boundary conditions at $r = R$(R is plasma radius) lead to the following[41]:

$$m\alpha J_m(TR) + kTRJ'_m(TR) = 0, \tag{7.22}$$

where ($'$) is the derivative of J_m with respect to its argument. The dispersion relation is determined by Eqs.7.5, 7.21 and 7.22. The above equations are valid when $\omega_{ci} \ll \omega \ll \omega_{ce}$[42]. Eq.7.22 can be solved by iteration for the m=1 wave. Fig 7.1 shows the dispersion for m=1 helicon wave for various plasma radii and the longitudinal wave number k is plotted as a function of the ratio of n_e/B_0 with n_e in unit of $10^{20}\mathrm{m}^{-3}$ and B_0 in unit of Tesla. Notice that the product of the plasma radius and the transverse wave number TR is a weak function of n_e/B_0 and has a value ~ 3.82 for $R < 15$mm (Fig 7.2). One finds that the condition of $k \ll T$ can be satisfied in the case of Basil-II plasma which has a typical ratio of

$n_e/B_0 \sim 10$ with density profile FWHM $\sim$ 7mm. This condition will be used in the later section to derive the damping length.

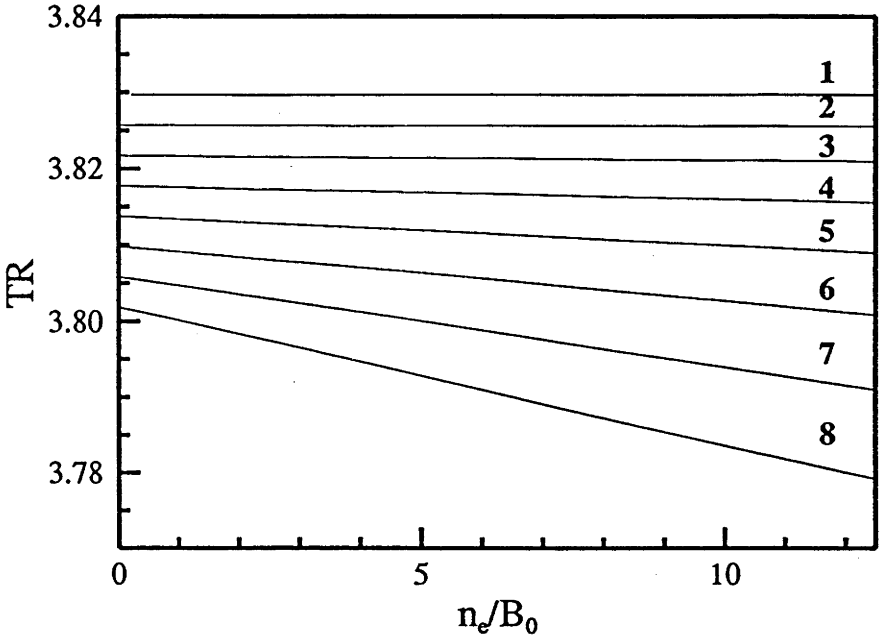

Figure 7.2: TR as a function of n_e/B_0 for plasma radius of (curve 1) 1mm, (curve 2) 3mm, (curve 3) 5mm, (curve 4) 7mm, (curve 5) 9mm, (curve 6) 11mm, (curve 7) 13mm, and (curve 8) 15mm.

7.2 The m=1 helicon wave phase velocity

As can be seen from the previous chapter the radial profiles of both the electron density and the stimulated emission of Ar^+ depend little on the tube diameter (Fig 4.5 and Fig 6.2), hence the plasma is not much affected by the tube wall within the tube diameter range of 30-65mm. Since the most important part of this plasma for laser application is the dense plasma core which can be considered as being a uniform cold plasma, it is possible to apply Eqs.7.5, 7.21, and 7.22 to

calculate the m=1 helicon wave phase velocity.

The calculation is carried out under the assumption that an m=1 Helicon wave propagates in a column of a diameter equal to the measured FWHM of electron density, with a uniform density equal to the measured volume averaged density within the column. The calculated results are listed in Table.7-1 together with the experimentally measured data used in the calculation. The second column of the table lists the measured volume averaged density within a column diameter defined by the measured FWHM of the radial density profile (the third column), for filling pressure of 0.9Pa, rf input power of 4.0kW at 7MHz. The fourth and the fifth columns are the measured and calculated phase velocity v_{ph}^{*} and v_{ph} respectively. The phase velocity is calculated using the data listed in the column 1, 2 and 3 of the table.

B_0 (T)	$\bar{n}$ (10^{19}m^{-3})	FWHM (mm)	v_{ph}^{*} (10^6m/S)	v_{ph} (10^6m/S)
0.02	0.683	27		4.12
0.03	0.956	26	5.03	4.58
0.04	2.322	25		2.63
0.05	3.005	24	3.75	2.64
0.06	4.226	18	3.15	3.00
0.07	5.600	15	2.21	3.17
0.08	6.280	15	2.26	3.23
0.09	6.800	15		3.35
0.10	6.800	16	2.62	3.49
0.11	4.808	16.4		5.26
0.12	5.400	17	3.22	4.93
0.13	5.736	18.4		4.68
0.14	5.400	20	2.93	4.89
0.15	5.400	20.1	3.25	4.98

Table 7-1. Phase velocity of the m=1 helicon wave in Basil-II

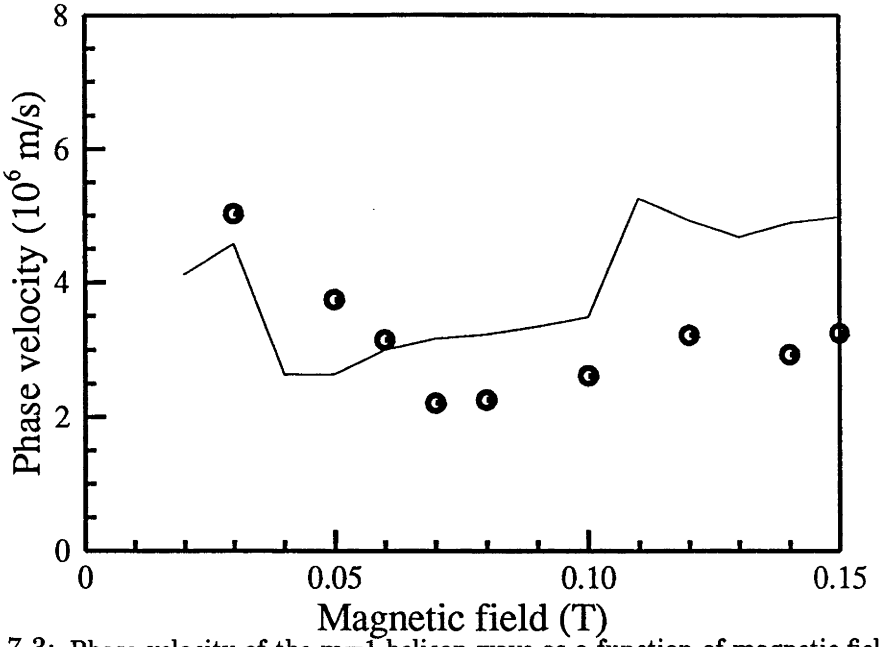

Figure 7.3: Phase velocity of the m=1 helicon wave as a function of magnetic field.

The calculated phase velocity is plotted in Fig 7.3 (solid line) together with that from the experimental measurements (o). Given the simplicity of the model, the results agree quite well with the experimental data in both the form and magnitude and hence confirm the reliability of the experimental measurements. It can be seen that the energy equivalent to the phase velocity has a minimum of $\sim$ 15 eV when the 488 nm laser output power (Fig 5.2) has its maximum. This energy is close to the upper-level energy of the 488 nm line transition (19.7 eV), implying that electrons are resonantly accelerated by the wave to the wave velocity and so cause the selected excitation of the upper-level 488 nm transition.

7.3 Collisional damping and Landau damping of the m=1 Helicon wave

A possible explanation of the population inversion mechanism is Landau damping of the m=1 Helicon wave.

The collisional and Landau damping in a plasma with cylindrical symmetry has been studied by Chen[43], whose analysis is followed below.

The dispersion relation (Eqs.7.21, 7.5, and 7.22) is derived under the assumption of a perfect conductive (zero resistivity) plasma. However, there always is a finite resistivity in a real plasma, hence there can be a non-zero electric field component parallel to B_0 which can interact directly with the electrons and distort the distribution function. Let η be the finite resistivity, Eq.7.3 then should be rewritten as

$$\vec{E} = \eta\vec{j} + \frac{\vec{j} \times \vec{B}}{en_e}. \tag{7.23}$$

One can then obtain:

$$\vec{B} = \frac{1}{\alpha}\nabla \times \vec{B} + i\frac{\eta}{\omega\mu_0}\nabla^2\vec{B}. \tag{7.24}$$

To represent a spatially damped wave, ω should be real, so that the wave vector k hence α has to be complex to satisfy Eq.7.24. In a low pressure plasma like Basil-II, the resistivity η is small (nearly collisionless), so that the last term $\nabla^2\vec{B}$ can be approximated by the η=0 value, $-\alpha_0\vec{B}$ with α_0 defined by

$$\alpha_0 \equiv (\frac{\omega}{\mathrm{Re}(k)})(\frac{e\mu_0 n_e}{B_0}). \tag{7.25}$$

Eq.7.24 then becomes

$$(1 + i\frac{\eta\alpha_0^2}{\omega\mu_0})\alpha\vec{B} = \nabla \times \vec{B}. \tag{7.26}$$

Taking curl of Eq.7.26, one obtain

$$\nabla^2\vec{B} + \alpha^2(1 + i\frac{\eta\alpha_0^2}{\omega\mu_0})^2\vec{B} = 0. \tag{7.27}$$

Comparing with Eq.7.22, one can write the dispersion relation directly by simply replacing α with $\alpha(1 + i\frac{\eta\alpha_0^2}{\omega\mu_0})$:

$$m\alpha(1 + i\frac{\eta\alpha_0^2}{\omega\mu_0})J_m(TR) + kTRJ_m'(TR) = 0, \tag{7.28}$$

Notice that the transverse wave number is now defined by

$$T^2 = \alpha^2(1 + i\frac{\eta\alpha_0^2}{\omega\mu_0})^2 - k^2 \tag{7.29}$$

Let T be real to represent only longitudinal damping, k can be expressed as [44]

$$k = \frac{\omega e n_e \mu_0}{TB_0}(1 + i\frac{\eta\alpha_0^2}{\omega\mu_0}). \tag{7.30}$$

As mentioned in the previous section, for the case of Basil-II plasma the condition of $k \ll T$ is satisfied so that one can write $T \sim \alpha_0$, and k can then be written as:

$$k \simeq \frac{\omega}{\alpha_0}(\frac{e\mu_0 n_e}{B_0})(1 + i\frac{\eta\alpha_0^2}{\omega\mu_0}). \tag{7.31}$$

The collision length can thus be estimated as

$$L_c = \frac{1}{\mathrm{Im}(k)} \simeq \frac{\omega_{ce}}{\alpha_0\nu_{ei}}, \tag{7.32}$$

where ν_{ei} is the electron-ion collision frequency given by $\nu_{ei} = \frac{n_e e^2}{m_e}\eta$. The collision excitation mean free path can then be roughly estimated by

$$\lambda_c \sim \exp(-\frac{eV^*}{T_e})L_c, \tag{7.33}$$

where eV^* is the excitation energy and T_e is in unit of eV.

It has been shown that the collisionless damping (Laudau damping) effect can be expressed by an effective resistivity [43]

$$\eta_{eff} = \frac{\omega}{\varepsilon_0\omega_p^2}\zeta^2 Z'(\zeta) \tag{7.34}$$

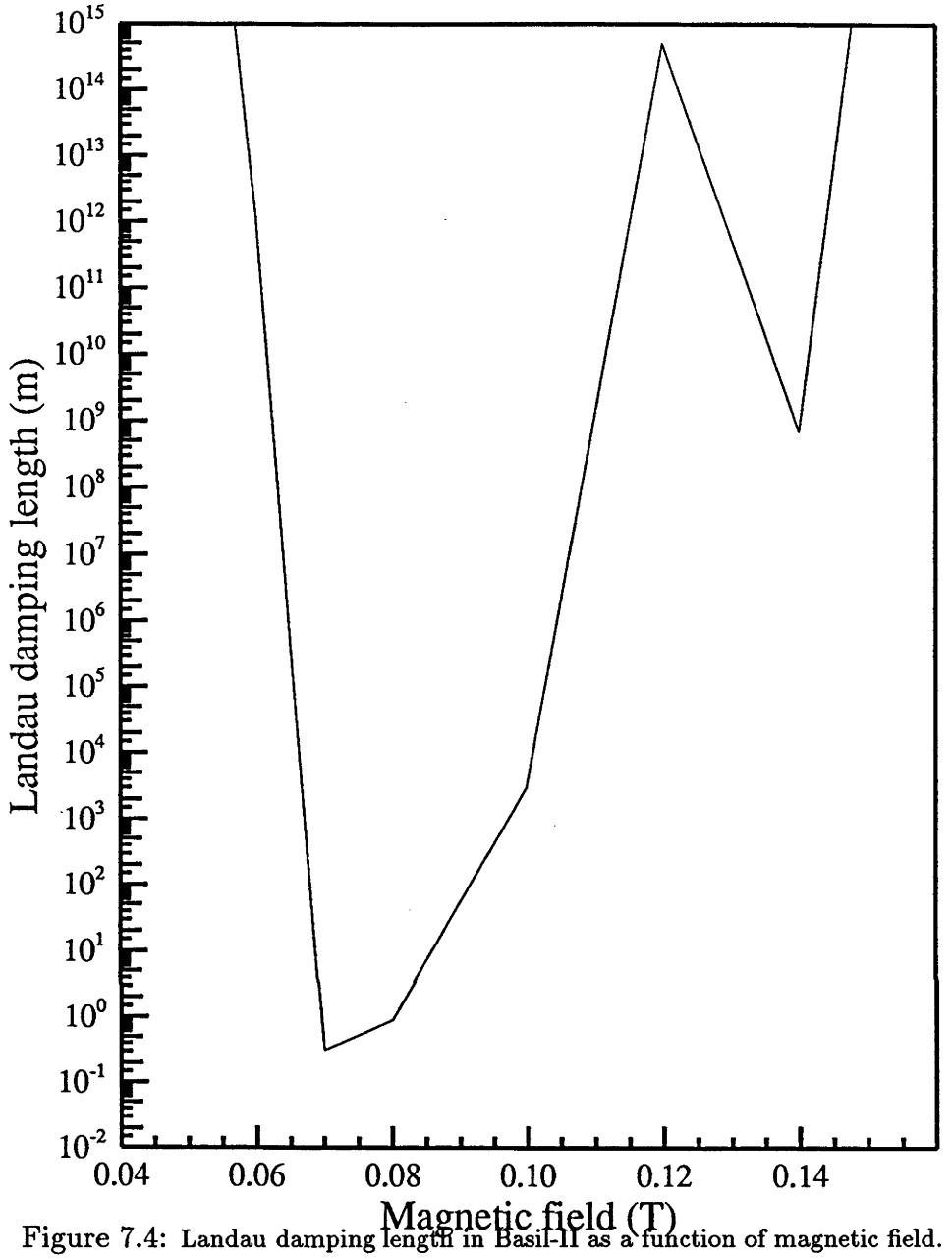

Figure 7.4: Landau damping length in Basil-II as a function of magnetic field.

where $\zeta = \frac{\omega}{kv_{th}}$ and Z' is the derivative of the plasma dispersion function. The Landau damping length (L_{LD}) can then be estimated by replacing η with η_{eff} in Eq.7.32. This will lead to

$$L_{LD} = \frac{\omega_{ce}}{\omega\alpha_0^2}\frac{e^{\zeta^2}}{2\sqrt{\pi}\zeta^3}. \tag{7.35}$$

Eqs.7.33 and 7.35 can be used to estimate the effect of Landau damping in

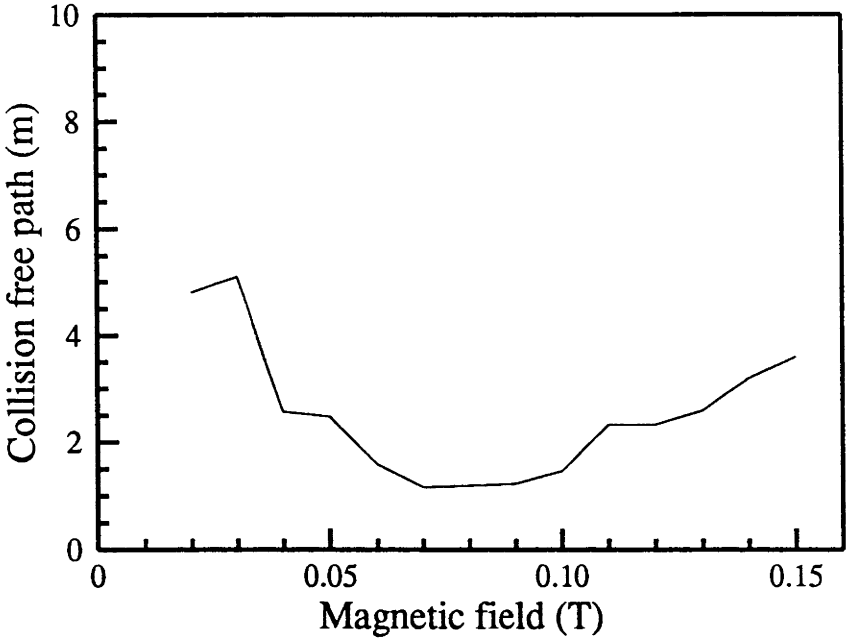

Figure 7.5: Collision excitation mean free path in Basil-II as a function of magnetic field.

Basil-II plasma. Using the experimentally measured data listed in Table.7-1 and T_e ~4.3eV, one finds that the Landau damping length (L_{LD}) is sensitive to the longitudinal magnetic field (Fig 7.4) and has a minimum ~0.3m when B_0 is in the range of 0.07-0.08T, the optimal B_0 for the laser operation. On the other hand, the collision length is not that strongly linked with the B_0 field and an estimate of mean free path for collision excitation yields several meters (Fig 7.5). This means, under some conditions, Landau damping could play an important role in energy transferring and provide an efficient means for transfer energy to the electrons with energies close to that required for upper state excitation of the laser transition, which subsequently suffers inelastic collisions in the column, hence it suggests Landau damping could be the main mechanism for the population inversion in this plasma.

To obtain population inversion in a gas-ion laser system, high energy gaps of the ionization of the working gas and the excitation of the upper state of

the laser transition must be overcome. This ,in turn, results in the very high threshold electron current density (hence threshold power) requirement in a dc-excited system to obtain sufficient excitation of the upper states of the laser transitions. The selective excitation method based on Landau damping of m=1 helicon wave is then especially important for these lasers, since it offers a direct path to transfer energy to those electrons which are responsible for the ionization or the excitation of the upper level of the laser transition. The total energy required by the system using such an excitation mechanism can be expected to be significantly reduced so that the efficiency of the system would increase. This is somewhat confirmed by the already-observed much lower power threshold for the Basil-II laser.

This new population inversion mechanism can be applied to the argon ion laser system and possibly also to the other ion lasers.

Chapter 8

Summary and conclusion

This chapter gives a summary and some conclusions of the thesis.

The optical properties of the plasma are experimentally measured and it is found that enough optical gain (> 3% single pass) of the Ar^+ 488nm line for the plasma operating as a laser source can be obtained under the experimental condition of:

0.4Pa < P < 1.4Pa;

0.06T < B_0 < 0.12T for RF at 7MHz;

0.12T < B_0 < 0.16T for RF at 14MHz;

RF Power > 1.5kW.

The features of the new Ar^+ laser based on the Basil-II plasma are investigated and nine of the ten popular laser transitions within green to blue range, which have been found in the dc-excited Ar^+ laser, have been observed in the new developed Basil laser. The efficiency of this new system is similar, at this stage, to that of the dc-excited Ar^+ laser, which has been fully developed after more than 25 years research. The low threshold power requirement for this new system,

however, suggests that a higher efficiency could be expected by running the system at a higher power level.

The plasma parameters in the Basil-II plasma are measured in this study. The electron density of this plasma is $\sim 10^{20}m^{-3}$. The electron energy distribution is found to be non-Maxwellian during the first 1ms after the plasma initiation. A beam-like electron tail is observed in the energy range of 30-80eV. The duration (1ms) of this distribution suggests a driving mechanism which is sufficiently strong to overcome the scattering of the beam due to the expected beam-plasma instability.

The possible population inversion machenism is studied and it is found that Landau damping of m=1 helicon wave can offer a direct energy transfer path which in turn derives the selective excitation of the laser transition upper level.

It can be concluded from this study that enough population inversion for laser operation can be obtained in an electrodeless argon plasma generated by rf excited m=1 helicon wave, and the Landau damping of the m=1 helicon wave can play an important role in the formation of the population inversion. The laser system based on such a mechanism can remove problems associated with the electrodes and has lower power threshold than that of any common dc-excited Ar^+ laser, which implies a possible higher efficiency of the system. This new mechanism offers a new path for the further development of gas-ion lasers.

Bibliography

[1] I. E. Sakharov, V. V. Ermolin, and S. V. Shatalin **Sov. Phys. Tech. Phys.**, Vol.19 (1974) 1081-1084

[2] G. Herziger, and W. Seelig, **Z. fur Physik**, Vol219, (1969), 5

[3] W. B. Bridges, **Appl. Phys. Lett.**, Vol.4 (1964), 128-130

[4] V. F. Kitaeva, A. I. Odintsov, and N. N. Sobelev, **Usp. Fiz. Nauk**, Vol.99, (1969), 362-416

[5] W. B. Bridges, A. N. Chester, and A. S. Halsted, **Proc. IEEE**, Vol.59, (1971), 724-737

[6] S. C. Lin and C. C. Chen, **Am. Aeronaut & Astronautics J.**, Vol.9, (1971), 4-11

[7] Yu. I. Ovsepyan, **Proceedings of the P.N. Lebedev Physics Institute, Academy of Sciences of the USSR**, Vol.145, Part 1, (1984); English Translation: **J. Sov. Laser Research** Vol.7, (1986), 416-488

[8] V. I. Donin, D. A. Shapiro, D. V. Yakovin, and A. S. Yatsenko, **Phys. Lett. A**, Vol.126, (1988), 273-276

[9] S. A. Babin, V. I. Donin, and A. E. Kuklin, **7th International Symposium of Gas Flow & Chemical Lasers**, (Vienna, 22-26 August 1988), 99

[10] V. F. Kitaeva, Yu. I. Osipov, and V. V. Pikalov, **Zh. Tekh. Fiz.**, Vol.48, (1978), 1663-1671

[11] R. W. Boswell,R. Porteous,A. prytz,A. Bouchoule and P. Ransonne, **Physics Letters**, Vol.91A, No.4, (1982), 163-166

[12] R. W. Boswell, **A Study of Waves in Gaseous Plasmas**, Thesis for the Degree of the Doctor of Philosophy, The Flinders University of South Australia, July 1970

[13] R. W. Boswell, **Plasma Physics and Controlled Fusion**, Vol.26, (1984), 1147

[14] R. W. Boswell, **Phys. Lett.**, Vol.33A, (1970), 457-458

[15] C. Christopoulos, R. W. Boswell and P. J. Christiansen, **Phys. Lett.**, Vol.47A, (1974), 239-240

[16] R. W. Boswell, A. J. Perry and M. Emami, **J. Vac. Sci. Technol.**, Vol.A7, (1989), 3345-3350

[17] A. J. Perry and R. W. Boswell, **Appl. Phys. Lett.**, Vol.55, (1989), 148-150

[18] Peiyuan Zhu and R. W. Boswell, **Phys. Fluids B,** Vol._, (1991),

[19] F. F. Chen, **Laser and Particle Beams**, Vol7, (1989), 551

[20] R. Brown and J. Lang, **Astrophysical & Laboratory Spectroscopy**, (Proceedings of the thirty-third Scottish Universities Summer School in Physics, 1988)

[21] N. Hershkpwitz, **Chapter 3, Plasma Diagnostics** Academic Press, Inc. San Diego (1989), Vol.1, 113-181

[22] J. D. Swift and M. J. R. Schwar, **Electrical Probes for Plasma Diagnostics** London Iliffe Books Ltd. (1970)

[23] F. F. Chen, **Plasma Diagnostic Techniques** Academic Press (1965), Chapter 4, p.164

[24] M. A. Heald and C. B. Wharton, **Plasma Diagnostics with Microwaves**, John Wiley & Sons Inc., (1965)

[25] H. Meuth and E. Sevillano, **Chapter 5, Plasma Diagnostics**, Academic Press, Inc. San Diego (1989), Vol.1, 239-307

[26] Z. Xiang and C. Yu, **High Temperature Plasma Diagnostic Technology** Shanghai Science and Technology Press, (1982)

[27] Peiyuan Zhu, R. Boswell, **Phys. Rev. Lett.**, Vol63, No.26, (1989), 2805-2808

[28] C. S. Willett, **Introduction to gas lasers: population inversion mechanisms**, Pergamon Press Ltd., (1974)

[29] A. E. Siegman, **Lasers**, University Science Books, Mill Valley, California (1979)

[30] Hans R. Griem, **Plasma spectroscopy**, McGraw-Hill Company, Inc., (1964), p176-177

[31] W. Magnus and F. Oberhettinger, **Functions of Mathematical Physics**, Chelsea Publishing Company, New York, (1954), 141

[32] Yu. I. Ovsepyan **Trudy Ordena Lenina Fizicheskogo Instituta im. P. N. Lebedeva AN SSSR**, Vol145, (1984), 3-78

[33] G. Herziger, and W. Seelig, **Z. fur Physik**, Vol219, (1969), 5

[34] H. Boersh, J. Boscher, D. Hoder and G.Schafer, **Physic Letters**, Vol31A, N0.4, (1970), 188-189

[35] Peiyuan Zhu and R. W. Boswell, **J. Appl. Phys.**, Vol.68, (1990), 1981

[36] D. A. Whelan and R. L. Stenzel, **Phys. Rev. Lett.**, Vol.50, (1983), 1133

[37] S. Kainer, J. Dawson and R. Shanny, **Phys. Fluids**, Vol.15, (1972), 493

[38] D. Boyd, W. Carr, R. Jones and M. Seidl, **phys. Lett.**, Vol.45A, (1973), 421

[39] P. Y. Cheung and A. Y. Wong, **Phys. Fluids**, Vol.28, (1985), 1538

[40] F. F. Chen, **Introduction to Plasma Physics and Controlled Fusion** Vol.1: Plasma Physics, Plenum Press, (1984)

[41] F. F. Chen, **Proceedings of 1987 International Conference on Plasma Physics (Kiev, USSR Apr. 1987)**, Vol.4, 321-324

[42] F. F. Chen, **Report ANU-PRL IR 85/12**, Australian National University, (1985)

[43] F. F. Chen, To be submitted to **Plasma physics and Controlled Fusion**,

[44] F. F. Chen, **U.S.-Japan Seminar on Generation and Application of Hot, Dense Laser Plasmas**, (Honolulu, Hawaii, August 8-12, 1988)